

## HYPERVELOCITY IMPACT EFFECTS ON LIQUID HYDROGEN TANKS

by  
C.W. FERGUSON

N66-22267

FACILITY FC-101-102

145 (PAGES)	1 (CODE)
CR-54852 (NASA OR CONTRACT NUMBER)	32 (CATEGORY)

GPO PRICE \$ \_\_\_\_\_

CFSTI PRICE(S) \$ \_\_\_\_\_

Hard copy (HC) 3.00

Microfiche (MF) 1.50

# 653 July 65

prepared for  
NATIONAL AERONAUTICS AND SPACE ADMINISTRATION  
CONTRACT NAS 3-4193

**DOUGLAS MISSILE & SPACE SYSTEMS DIVISION**

#### NOTICE

This report was prepared as an account of Government sponsored work. Neither the United States, nor the National Aeronautics and Space Administration (NASA), nor any person acting on behalf of NASA:

- A.) Makes any warranty or representation, expressed or implied, with respect to the accuracy, completeness, or usefulness of the information contained in this report or that the use of any information, apparatus, method, or process disclosed in this report may not infringe privately owned rights; or
- B.) Assumes any liabilities with respect to use of, or for damages resulting from the use of any information, apparatus, method or process disclosed in this report.

As used above, "person acting on behalf of NASA" includes any employee or contractor of NASA, or employee of such contractor, to the extent that such employee or contractor of NASA, or employee of such contractor prepares, disseminates, or provides access to, any information pursuant to his employment or contract with NASA, or his employment with such contractor.

Requests for copies of this report should be referred to

National Aeronautics and Space Administration Office of  
Scientific and Technical Information  
Attention: AFSS-A  
Washington, D.C. 20546

## FINAL REPORT

# HYPERVELOCITY IMPACT EFFECTS ON LIQUID HYDROGEN TANKS

by  
C.W. FERGUSON

prepared for  
NATIONAL AERONAUTICS AND SPACE ADMINISTRATION  
March 31, 1966

CONTRACT NAS 3-4193

Technical Management  
NASA Lewis Research Center  
Cleveland, Ohio  
Chemical Rocket Systems Division  
Gordon T. Smith

Douglas Aircraft Company, Inc.  
Missile and Space Systems Division  
Santa Monica, California

## PREFACE

This report was prepared by Douglas Aircraft Company, Inc., Missile and Space Systems Division, under NASA Contract NAS 3-4193. This investigation was initiated by Lewis Research Center of NASA to determine the structural behavior of liquid hydrogen propellant tanks when subjected to meteoroid impact. The work was administered under the direction of the Chemical Rocket System Division, G. T. Smith, Project Manager.

The report covers the work period 1 July 1964 through 30 November 1965. It is submitted to fulfill this contract and is cataloged by Douglas as Report No. SM-52027.

At Douglas, R. W. Hallet, Jr., Director of Research and Development, and Dr. H. H. Dixon, Chief Engineer of the Advance Structures and Mechanical Department, provided technical direction, and C. W. Ferguson acted as Program Manager. W. C. Jenkins, Research and Development, directed the fracture mechanics experimental and analytical work. R. N. Teng, Douglas Aerophysics Laboratory, directed the hypervelocity impact experiments. G. E. Sutila, Douglas Aerophysics Laboratory, directed the design and installation of the  $\text{LH}_2$  facility at the Ballistic Range.



## CONTENTS

		Page
	LIST OF FIGURES . . . . .	vii
	LIST OF TABLES . . . . .	xi
	SYMBOLS . . . . .	xiii
Section		
1	SUMMARY . . . . .	1
2	INTRODUCTION. . . . .	3
3	PROGRAM PLAN. . . . .	7
4	EXPERIMENTAL TESTING APPARATUS. . . . .	13
	4.1 Uniaxial Static Fracture Test Procedure . . . . .	13
	4.2 Biaxial Static Fracture Test Procedure . . . . .	18
	4.3 Hypervelocity Impact Test Procedure . . . . .	23
5	STATIC FRACTURE TESTS OF PREFLAWED PANELS . . .	47
	5.1 Uniaxial Panel Fracture Tests . . . . .	47
	5.2 Biaxial Panel Fracture Tests . . . . .	54
6	HYPERVELOCITY IMPACT POINT-LOAD TESTS . . . . .	61
	6.1 Liquid Nitrogen Checkout Tests . . . . .	62
	6.2 Tests of Quasi-Composite Panels at LH <sub>2</sub> Temperature . . . . .	64
	6.3 Tests of Unprotected Panels at LH <sub>2</sub> Temperatures. . .	67
7	HYPERVELOCITY IMPACT DISTRIBUTED-LOAD TESTS. .	99
	7.1 Meteoroid Shield Test Program . . . . .	99
	7.2 Basic Test Results . . . . .	101
	7.3 Correlation of Test Results with Impact Energy and Shield Spacing . . . . .	104
8	CONCLUSIONS . . . . .	111
Appendix		
A	PROCESSING HISTORY AND CHEMICAL COMPOSITION OF TEST PANEL RAW MATERIALS . . . . .	113
B	MECHANICAL PROPERTIES OF TEST PANEL MATERIALS . . . . .	115
C	STATIC FRACTURE TESTS OF PREFLAWED PANELS TABULATED DATA . . . . .	123
D	HYPERVELOCITY IMPACT TEST RESULTS TABULATED DATA . . . . .	129

5-3	Uniaxial Fracture Tests of Impact-Flawed Panels (5A1-2.5 Sn (ELI) Titanium Test Temperature--423°F) . .	52
5-4	Uniaxial Fracture Tests of Center Preflawed Panels (2219-T87 Aluminum Test Temperature--423°F) . . . . .	53
5-5	Uniaxial Fracture Tests of Center Fatigue-Cracked Panels (5AL-2.5 Sn (ELI) Titanium Test Temperature-- 423°F) . . . . .	55
5-6	Uniaxial Fracture Tests of Center Impact-Flawed Panels (5AL-2.5 Sn (ELI) Titanium Test Temperature--423°F) . .	55
5-7	Uniaxial Fracture Tests of Center Preflawed Panels (2219-T87 Aluminum Test Temperature--423°F) . . . . .	56
5-8	Burst Tests of Preflawed Biaxial Panels (2219-T87 Aluminum Test Temperature--423°F) . . . . .	58
5-9	Burst Tests of Fatigue-Cracked Biaxial Panels (5A1-2.5 Sn (ELI) Titanium Test Temperature--423°F) . . . . .	58
5-10	Burst Tests of Impact Preflawed Biaxial Panels (5A1-2.5 Sn (ELI) Titanium Test Temperature--423°F) . .	59
5-11	Burst Tests of Preflawed Biaxial Panels (2219-T87 Aluminum Test Temperature--423°F) . . . . .	59
5-12	Burst Tests of Fatigue-Cracked Biaxial Panels (5A1-2.5 Sn Titanium (ELI) Test Temperature--423°F) . .	60
5-13	Burst Tests of Impact Preflawed Biaxial Panels (5A1-2.5 Sn (ELI) Titanium Test Temperature--423°F). . .	60
6-1	Hypervelocity Impact Tests of Stressed Biaxial Panels-- Aluminum (Behavior of 0.032-In. -Thick 2219-T87 Aluminum at LN <sub>2</sub> Temperature) . . . . .	63
6-2	Hypervelocity Impact Tests of Stressed Biaxial Panels-- Titanium (Behavior of 0.036-In. -Thick 5A1-2.5 Sn (ELI) Titanium at LN <sub>2</sub> Temperature) . . . . .	63
6-3	Correlation of LN <sub>2</sub> Checkout Tests with Impact Energy (Behavior of 0.032-In. -Thick 2219-T87 Aluminum) . . . . .	65
6-4	Correlation of LN <sub>2</sub> Checkout Tests with Impact Energy (Behavior of 0.036-In. -Thick 5A1-2.5 Sn (ELI) Titanium) .	65
6-5	Results of Hypervelocity Impact Tests of Quasi-Composite Panels . . . . .	66
6-6	Correlation of Quasi-Composite Panel Test Results with Impact Energy (Behavior of 0.032-In. -Thick 2219-T87 Aluminum at LH <sub>2</sub> Temperature) . . . . .	68
6-7	Correlation of Quasi-Composite Panel Test Results with Impact Energy (Behavior of 0.015-In. -Thick 5A1-2.5 Sn (ELI) Titanium at LH <sub>2</sub> Temperature) . . . . .	68

## FIGURES

4-1	Uniaxial Testing Apparatus . . . . .	14
4-2	Setup for Growing Fatigue Cracks in Uniaxial Panels . . . .	16
4-3	Typical Primary and Secondary Type Hypervelocity Prelaws in Uniaxial Panels . . . . .	17
4-4	16mm Camera Photorecording--Burst Test No. 7 . . . . .	23
4-5	Post Test Condition of Test Panel--Burst Test No. 7 . . . .	24
4-6	Schematic of Douglas Aerophysics Laboratory Ballistic Range . . . . .	25
4-7	Ballistic Range Light Gas Gun . . . . .	25
4-8	Observed Distribution of Impact Velocity . . . . .	28
4-9	Ballistic Range LH <sub>2</sub> System Schematic . . . . .	30
4-10	LH <sub>2</sub> System Installation in the Ballistic Range . . . . .	31
4-11	LN <sub>2</sub> and LH <sub>2</sub> Supply System at the Ballistic Range . . . . .	31
4-12	Biaxial Cryogenic Test Fixture . . . . .	32
4-13	Dynamic Pressure Transducer Installation . . . . .	34
4-14	Data Readout System and Ballistic Range Control Console .	35
4-15	Setup for Hydrostatic Bulging of Biaxial Panels . . . . .	36
4-16	Relation of Spherometer Reading to Spherical Radius . . . .	37
4-17	Forming of Bulged Biaxial Panels (0.032-Gage Aluminum Panel No. B02) . . . . .	38
4-18	Calculated Membrane Stresses in a Biaxial Bulged Panel (0.032-Gage Aluminum Panel No. B02) . . . . .	38
4-19	Measured Shape of Biaxial Bulged Panel (0.032-Gage Aluminum Panel No. B02) . . . . .	39
4-20	Biaxial Panel Remote Readout Sphereometer . . . . .	41
4-21	Biaxial Panel Strain-Gage Instrumentation . . . . .	42
4-22	Strain-Gage Calibration of Aluminum Biaxial Panels . . . .	43
4-23	Strain-Gage Calibration of Titanium Biaxial Panels . . . .	44
5-1	Typical Results of Uniaxial Static Fracture Tests . . . . .	48
5-2	Uniaxial Fracture Tests of Center Fatigue-Cracked Panels (5A1-2.5 Sn (ELI) Titanium Test Temperature-- 423°F) . . . . .	52

6-8	Typical Results of Point-Load Tests of Quasi-Composite Panels (Behavior of 0.032-In. - Thick 2219-T87 Aluminum at LH <sub>2</sub> Temperature) . . . . .	69
6-9	Fracture Strength of Impact Damaged Quasi-Composite Biaxial Panels (Behavior of 0.032-In. - Thick Aluminum Alloy at LH <sub>2</sub> Temperature) . . . . .	70
6-10	Results of Biaxial Panel Point-Load Tests (Behavior of 0.032-In. - Thick 2219-T87 Aluminum at LH <sub>2</sub> Temperature) .	72
6-11	Results of Biaxial Panel Point-Load Tests (Behavior of 0.125-In. - Thick 2219-T87 Aluminum at LH <sub>2</sub> Temperature) .	72
6-12	Results of Biaxial Panel Point-Load Tests (Behavior of 0.015-In. - Thick 5Al-2.5 Sn (ELI) Titanium at LH <sub>2</sub> Temperature). . . . .	73
6-13	Results of Biaxial Panel Point-Load Tests (Behavior of 0.036-In. - Thick 5Al-2.5 Sn (ELI) Titanium at LH <sub>2</sub> Temperature). . . . .	73
6-14	Results of Point-Load Tests of 2219-T87 Aluminum Panels .	75
6-15	Results of Point-Load Tests of 5Al-2.5 Sn (ELI) Titanium Panels . . . . .	75
6-16	Comparison of Biaxial Panel Point-Load Impact Tests with Static Burst Tests of Preflawned Panels (Behavior of 0.032-In. - Thick 2219-T87 Aluminum at LH <sub>2</sub> Temperature) .	76
6-17	Comparison of Biaxial Panel Point-Load Impact Tests with Static Burst Tests of Preflawned Panels (Behavior of 0.125-In. - Thick 2219-T87 Aluminum at LH <sub>2</sub> Temperature) .	76
6-18	Comparison of Biaxial Panel Point-Load Impact Tests with Static Burst Tests of Preflawned Panels (Behavior of 0.015-In. - Thick 5Al-2.5 Sn (ELI) Titanium at LH <sub>2</sub> Temperature) . . . . .	77
6-19	Comparison of Biaxial Panel Point-Load Impact Tests with Static Tests of Preflawned Panels (Behavior of 0.036-In. - Thick 5Al-2.5 Sn (ELI) Titanium at LH <sub>2</sub> Temperature) . . .	77
6-20	Layout to Determine Shock Path Geometry (Shot No. B-8.2-49, Panel No. 032A No. B20) . . . . .	81
6-21	Correlation LH <sub>2</sub> Shock Measurements with Chou's Equation .	82
6-22	Correlation of LH <sub>2</sub> Shock Data with Chou's Equation . . . . .	84
6-23	Effect of Including Energy Partitioning During Correlation of LH <sub>2</sub> Shock Data using Chou's Equation . . . . .	85
6-24	Fit of Chou's Equation to High- and Low-Energy Shots . . . .	87
6-25	Correlation of Point-Load Test Results with Impact Energy (Behavior of 0.032-In. - Thick 2219-T87 Aluminum at LH <sub>2</sub> Temperature). . . . .	91

6-26	Correlation of Point-Load Test Results with Impact Energy (Behavior of 0.125-In. - Thick 2219-T87 Aluminum at LH <sub>2</sub> Temperature) . . . . .	91
6-27	Correlation of Point-Load Test Results with Impact Energy (Behavior of 0.015-In. - Thick 5Al-2.5 Sn (ELI) Titanium at LH <sub>2</sub> Temperature) . . . . .	92
6-28	Correlation of Point-Load Test Results with Impact Energy (Behavior of 0.036-In. - Thick 5Al-2.5 Sn (ELI) Titanium at LH <sub>2</sub> Temperature) . . . . .	92
6-29	Master Curve--Results of Biaxial Panel Point Load Tests (Behavior of 2219-T87 Aluminum and 5Al-2.5 Sn (ELI) Titanium at LH <sub>2</sub> and LN <sub>2</sub> Temperatures). . . . .	96
7-1	Fixture Setup for Distributed-Load Tests . . . . .	101
7-2	Results of Biaxial Panel Distributed-Load Tests (Behavior of 0.032-In. - Thick 2219-T87 Aluminum at LH <sub>2</sub> Temperature). . . . .	102
7-3	Results of Biaxial Panel Distributed-Load Tests (Behavior of 0.015-In. - Thick 5Al-2.5 Sn (ELI) Titanium at LH <sub>2</sub> Temperature). . . . .	103
7-4	Typical Distributed-Load Test Results . . . . .	104
7-5	Correlation of Distributed-Load (Meteoroid Shield) Test Results with Impact Energy and Shield Spacing (Behavior of 0.032-In. - Thick 2219-T87 Aluminum at LH <sub>2</sub> Temperature). . . . .	105
7-6	Correlation of Distributed-Load (Meteoroid Shield) Test Results with Impact Energy and Shield Spacing (Behavior of 0.125-In. - Thick 2219-T87 Aluminum at LH <sub>2</sub> Temperature) . . . . .	106
7-7	Correlation of Distributed-Load (Meteoroid Shield) Test Results with Impact Energy and Shield Spacing (Behavior of 0.015-In. - Thick 5Al-2.5 Sn (ELI) Titanium at LH <sub>2</sub> Temperature). . . . .	108
7-8	Correlation of Distributed-Load (Meteoroid Shield) Test Results with Impact Energy and Shield Spacing (Behavior of 0.036-In. - Thick 5Al-2.5 Sn (ELI) Titanium at LH <sub>2</sub> Temperature). . . . .	109
B-1	Mechanical Properties of 2219-T87 Aluminum . . . . .	121
B-2	Mechanical Properties of 5Al-2.5 Sn (ELI) Titanium . . . . .	121

## TABLES

4-I	Characteristics of Aluminum Spherical Projectiles . .	27
5-I	Fracture Toughness at -423°F. . . . .	53
A-I	Processing History and Chemical Composition of Test Panel Raw Materials. . . . .	113
B-I	Room Temperature Mechanical Properties of Test Panel Sheet Materials (Vendor Data) . . . . .	116
B-II	Room Temperature (70°F) Mechanical Properties of Test Panel Sheet Materials (Douglas Tests) . . . . .	117
B-III	LH <sub>2</sub> Temperature (-423°F) Mechanical Properties of Test Panel Sheet Materials (Douglas Tests) . . . . .	119
C-I	Fatigue Preflawn Uniaxial Panels Test Plan . . . . .	124
C-II	Hypervelocity Impact Preflawn Uniaxial Panels Test Plan. . . . .	124
C-III	Fatigue Preflawn Biaxial Panels Test Plan . . . . .	125
C-IV	Hypervelocity Impact Preflawn Biaxial Panels Test Plan . . . . .	125
C-V	Uniaxial Tests of 2219-T87 Aluminum Panels at -423°F . . . . .	126
C-VI	Uniaxial Tests of 5Al-2.5Sn(ELI) Titanium Panels at -423°F . . . . .	127
C-VII	Biaxial Burst Tests of Preflawn Panels at -423°F . . .	128
D-I	LN <sub>2</sub> Checkout Shots . . . . .	130
D-II	Point Load Tests of Quasi-Composite Panels . . . . .	131
D-III	Point Load Tests of Unprotected Panels . . . . .	133
D-IV	Test Plan for Distributed-Load Tests . . . . .	135
D-V	Distributed-Load Test Results . . . . .	136

## SYMBOLS

$2a$	critical crack length
$2a_o$	initial crack length
$A$	a constant
$B$	a constant
$C$	bulge coefficient Equation 5-3
$c_o$	sonic velocity
$d$	projectile diameter
$D$	hole diameter Equation 6-1
$D_b$	adiabatic compressibility Equation 6-7
$E$	Young's Modulus
$E_b$	bulk modulus Equation 6-8
$ELI$	extra low interstitial
$f$	indicates a function of
$K$	stress intensity factor
$K_c$	fracture toughness, critical stress intensity factor Equations 5-1 and 5-3
$K_{cn}$	nominal fracture toughness
$K_1, K_2, K_3$	dynamic pressure instrumentation stations
$K.E.$	kinetic energy
$KSI$	thousands of pounds per square inch
$k$	proportionality constant
$l_o$	initial flaw or crack length
$l_c$	critical flaw or crack length Equations 5-2 and 5-4
$l_f$	maximum length of arrested tear or fracture
$m$	nondimensional exponent
$P$	pressure
$P_\infty$	semi-infinite target crater
$R$	radius of curvature or shock wave radius
$R_I$	impact load and material strength parameter Equations 6-10, 6-11 and 6-16

$R_o$	characteristic length of the projectile
$R_p$	notch resistance factor Equation 5-2
$R_\sigma$	hoop stress ratio Equations 6-9
$S_s$	shield spacing
$s_o$	standard deviation
$t_o$	a constant Equation 6-12
$t$	time
$t_s$	panel thickness (sheet)
$U$	shock velocity Equation 6-3
UTS	ultimate tensile strength
$V$	projectile velocity
$v$	fluid volume
$v_o$	initial fluid volume
$v_{t_s}$	wall puncture volume
$v_\infty$	semi-infinite crater volume
$w$	panel width
YS	yield strength
$\alpha, \beta,$	
$\gamma, \theta, \xi$	dimensionless exponents
$\epsilon_H$	panel strain due to hoop loading
$\epsilon_B$	panel strain due to plate bending
$\rho$	density
$\rho_o$	initial density
$\sigma$	tensile stress (usually gross area)
$\sigma_H$	hoop tension stress Equation 5-3
$\sigma_{H_c}$	critical membrane hoop stress
$\sigma_R$	fracture strength
$\sigma_{uB}$	biaxial ultimate strength
$\sigma_u$	ultimate tensile strength
$\sigma_y$	uniaxial yield strength
$\sigma_{yB}$	biaxial yield strength
$\nu$	Poisson's ratio



## Section 1

### SUMMARY

An experimental and analytical investigation was conducted to determine the structural behavior of cryogenic tank wall materials under simulated meteoroid environments and to develop practical engineering methods defining tank working stresses under the impact of hypervelocity projectiles.

The boundary limits between safe fracture and catastrophic fracture were established for two metals used in cryogenic propellant tanks. The materials investigated were 2219-T87 aluminum and 5 Al-2.5 Sn (ELI) titanium alloy. Safe fracture boundary limits were established for a wide range of meteoroid masses and velocities. A semiempirical equation was developed from the experiments' results which can be used to safely design unprotected, pressurized tanks. Charts were constructed that correlated the fracture behavior of shielded tank walls with meteoroid impact characteristics and the protective shield geometries.

Hypervelocity projectiles of known weight were launched by a light-gas gun to simulate meteoroid impact. Preliminary impact tests were conducted with the tank walls at  $-320^{\circ}\text{F}$  and numerous tests were conducted at  $-423^{\circ}\text{F}$ . Measurements of shock-wave characteristics of the contained cryogenic propellants were taken and, then, used as an aid in formulating tank design equations.

The tank membrane stresses at fracture were related to the material fracture toughness. Fracture toughnesses were determined from hypervelocity preflawed and fatigue cracked panels at  $-423^{\circ}\text{F}$ . Good correlations were obtained between the experimental and calculated biaxial toughness which were predicted from uniaxial data.

## Section 2

### INTRODUCTION

In several current space propulsion systems, large size liquid hydrogen ( $\text{LH}_2$ ) fuel tanks constitute the major volumetric portion, as in the S-IV, the S-IVB, and the S-II Stages of Saturn Vehicle System. The Atlas-Centaur also contains an  $\text{LH}_2$ -fueled upper stage. These tanks are constructed of high-strength aluminum and stainless steel alloys. Studies indicate that titanium may also be used extensively for tank structures. Missions for these spacecraft in the near future will only expose the large  $\text{LH}_2$  tanks to the space environment for a relatively short time where probability of impact by large meteoroids is small. As missions become longer and as  $\text{LH}_2$  tankage becomes larger, the probability of impact of a dangerous-size meteoroid against the tank shell increases proportionately. Spacecraft on flights to and beyond the vicinity of Mars may be subjected to an increasing meteoroid impact flux rate; this conjecture is generally verified by the recent Mariner 4 measurements where micrometeoroid impact flux rates as a function of astronomical unit (AU) distance were obtained (Reference 1). Data on larger sizes of meteoroids are still very meager.

It has been reasonable to undertake current space missions with an incomplete knowledge of how cryogenic tankage (particularly  $\text{LH}_2$  tank structures) will respond to impact with significantly large meteoroids. However, for future missions it is essential that the behavior of pressure-stressed cryogenic tankage under meteoroid impact be completely defined, so that structures can be adequately designed. The research reported here was undertaken to produce reliable design data on the load-carrying capability of impact-damaged liquid hydrogen tank shells. The further purpose of this research is to assess the response of this type of structure to the point loads and distributed loads that are produced by hypervelocity impact. This research is essentially an extension of the preliminary investigations reported by Stepka and Morse (Reference 2). The immediate objectives have been accomplished and design

data have been produced on the behavior of the specific aluminum and titanium alloy shell structures which were tested. These data are presented in this document.

The program had two major objectives. The first objective was to develop very detailed design data on the behavior of specific materials under hypervelocity impact conditions, and the second objective was to develop methods for predicting the general behavior of cryogenic tank shells under hypervelocity impact conditions.

In the investigation for detailed design data, aluminum alloy 2219-T87 and titanium alloy 5Al-2.5Sn (ELI) were used as the basic materials for sheet raw stock and simulated tank shells.

In the investigation for methods of predicting the general behavior of pressure-stressed and fluid-filled cryogenic tank shells under hypervelocity impact conditions, the analyses gave consideration to such factors as (1) damage to the shell by direct interaction of the meteoroid particle with structural components and (2) the shock wave overpressures in the contained fluid.

Data on the  $\text{LH}_2$  shock time-histories were obtained for numerous impact conditions, and the nature of the  $\text{LH}_2$  shock was characterized by the method of Chou (Reference 3). Combination of the projectile impact characteristics with the  $\text{LH}_2$  shock wave characteristics governs the behavior of a simple shell structure when subjected to direct impact by a hypervelocity projectile.

Master design curves of the point-load test results were developed which adequately describe the particular shell configurations tested. The curves indicate trends of behavior which may be applicable to panels made from other alloys. Additional testing will enhance the confidence in the charts for design of panels that are of different geometry, or that contain different fluids, than those that were used for these initial tests. Point-load tests are representative of direct meteoroid impingement on a bare or unprotected  $\text{LH}_2$  tank shell.

The point-load tests showed that catastrophic fracture of a  $\text{LH}_2$  tank wall can result from the combination of a meteoroid-induced flaw and local over-pressure in the propellant. Such fractures would abort most space missions, and in severe cases would cause loss of the entire spacecraft and its payload.

To reduce the probability of this type of failure, many space vehicles have meteoroid bumper shields to protect the pressure-stressed propellant tank walls. These outer shields will vaporize and disperse the impacting meteoroid particles, and although such protection will greatly reduce the probability of puncture of propellant tanks, the secondary impact of debris resulting from a meteoroid strike against a bumper still poses a significant hazard.

A sizeable portion of the hypervelocity impact experiment effort was directed to the investigation of various meteoroid-shield-protected  $\text{LH}_2$  tank shells. These distributed-load impact test configurations consisted of simple sheet metal bumpers spaced at various distances in front of the biaxial panels.

Work on the fundamental nature of the impulse loading resulting from the interaction of a meteoroid with a thin shield is currently under intensive investigation by Dr. G. V. Bull and his associates at the Space Research Institute of McGill University. Some of the Douglas meteoroid-shield experiments were designed to complement Bull's work and to provide basic data for future studies on the more complex shielded structures.

Charts correlating the observed fracture behavior of shielded tank walls with the kinetic energy of the hypervelocity projectiles and the shield stand-off spacing have been developed and are presented in this report for all of the configurations tested.

The behavior of shielded tank shells under the conditions of hypervelocity impact is complex: the region of catastrophic fracture of a main shell is dependent upon (1) projectile-bumper configuration, (2) shield stand-off distance, (3) shield material and thickness, (4) stress-level in the tank shell, and (5) projectile impact velocity.

Hypervelocity projectiles were launched by the Douglas light-gas gun to simulate the meteoroid impacts. The projectile impact velocities were kept essentially constant throughout the test program, and impact velocities averaged 21,700 fps.

To provide baseline fracture mechanics data on the materials used to fabricate the impact test panels, a series of static fracture tests on both uniaxial and biaxial test specimens was conducted. All of the tests were conducted at  $\text{LH}_2$  temperature. Detailed results of all static tests are documented in this report, and the fracture data are used as an aid in correlating the results of the hypervelocity impact tests with the various fracture mechanics theories.

### Section 3

#### PROGRAM PLAN

The objective of this research program was to generate design data on and develop analysis methods for the behavior of meteoroid impact damaged liquid hydrogen tank shells. Two materials (2219-T87 aluminum alloy and 5Al-2.5Sn extra low interstitial (ELI) titanium alloy) were selected to be evaluated for use as the structural shell of a 13-foot-diameter, spherical liquid hydrogen ( $\text{LH}_2$ ) tank. The materials have characteristics that indicate that they may be well suited for use in cryogenic propellant tanks. The 2219-T87 aluminum alloy is currently being used for large spacecraft structures, and the use of the titanium alloy appears attractive for ultra-low-weight cryogenic propellant tanks (Reference 4). A relatively thick and thin gage thickness of each material was selected to cover actual thickness ranges that are representative of future system requirements.

#### Scope of the Investigation

To develop reliable design data it is necessary to test simulated flight articles (tanks which contain actual cryogenic propellants) under accurately simulated flight stresses. It is also necessary to accurately define the mass, velocity, and integrity of the impacting projectiles. To accomplish the research objectives, the following tasks were performed:

- (1) Task I consisted of design and fabrication of the biaxial test fixture, the procurement of material for all test specimens, the design of uniaxial and biaxial test panels, and the design and installation of the  $\text{LH}_2$  system in the Douglas Ballistic Range.
- (2) Task II consisted of fabrication and testing of preflawed uniaxial and biaxial panels. Fatigue flaws were produced in the panels at room temperature. Hypervelocity flaws were also produced in the uniaxial panels at room temperature. However, impact pre-flawed biaxial burst test specimens were selected from panels used during Task III testing that contained simple punctures. The panels were fractured statically at  $\text{LH}_2$  temperature as outlined below:

(A) Uniaxial panel tests.

1. Impact preflawed panels--12 tests.
2. Fatigue preflawed panels--8 tests.

(B) Biaxial panel tests.

1. Impact preflawed panels--7 tests.
2. Fatigue preflawed panels--8 tests.

The data obtained during these tests were compared to existing fracture mechanics theories. Static fracture characteristics were then considered in the analysis to correlate the Task III results with impact loading parameters.

- (3) Task III consisted of a series of hypervelocity impact tests to determine the effect of point and distributed impulse loads on biaxially stressed panels. The experimental phase consisted of the following (fixture charged with  $\text{LH}_2$  except as noted):

(A) Hypervelocity impact point-load tests.

1. Liquid nitrogen check-out tests.
2. Test quasi-composite configuration panels (See Section 6.2).
3. Test unprotected panels (See Section 6.3).

(B) Hypervelocity impact distributed load tests.

#### Selection of Materials for Test Panels

Two of the more promising candidate materials for large cryogenic propellant tanks for spacecraft structure are 2219-T87 aluminum alloy and 5Al-2.5Sn (ELI) titanium. Each material has attractive mechanical strength characteristics at low temperatures and can readily be fabricated into large tanks with simple weld-joints. In fact, NASA/Lewis Research Center is directing a comprehensive research effort to fully establish all pertinent characteristics of these materials. The hypervelocity impact effects phase reported here is a component part of the overall effort.

The 2219 aluminum was purchased in 0.032- and 0.125-in. thicknesses. Sheet sizes were standard for the particular gages, 48 x 144-in. for the 0.125-in.-thick sheets, and 36 x 144-in. for the 0.032-in.-thick sheets. The material was procured in the T37 condition, then aged to the T87 condition before testing. All aluminum sheets were from the same vendor, were from the same mill run, and were procured especially for this program.

The 5Al-2.5Sn titanium, ELI grade, was purchased in 0.015 and 0.036-in. thicknesses, and all sheet sizes were 36 x 96-in. All titanium sheets were made from the same heat, and were also procured especially for the program.

Preceding materials investigations have shown that the low temperature fracture behavior of titanium alloys is quite dependent upon the percentage of interstitial elements (C, O<sub>2</sub>, H<sub>2</sub>, and N<sub>2</sub>) present, Reference (4) and (5). In the ELI (extra low interstitial) grade of titanium, the quantity of interstitial elements is held at very low levels. Therefore, knowledge of the processing history and precise chemical compositions of the particular heat of titanium is pertinent to the research effort. The chemical analysis of the heat of titanium from which the test specimens were made is given in Appendix A.

The aluminum alloys are not greatly sensitive to small variations in chemical composition. The material is normally procured to specifications which list allowable percentage ranges of the alloying elements; and the producer certifies that he meets the required specification values. The results of chemical analysis checks made by Douglas on several sheets of aluminum from the mill run were compared with specification values and found to be within specification. The comparative values are shown in Appendix A.

#### Test Panel Mechanical Properties

Detail tabulations of mechanical properties of the test panel materials are set forth in Appendix B of this report. Included are vendor data on room temperature properties and the results of Douglas tests of 48 ASTM type tensile specimens. Twenty-four of the tensile specimens were tested at room temperature and 24 were tested at LH<sub>2</sub> temperature (-423°F).

Average values of the results of the Douglas tests are used throughout this report for data analysis and impact test result correlation studies. Tensile test results indicate that the mechanical properties of each material do not vary significantly from the mean with either rolling direction or sheet thickness. Average mechanical properties for data correlation are as follows:



1. 2219-T87 Aluminum (-423°F).
  - A. UTS =  $\sigma_u$  = 102 KSI.
  - B. YS =  $\sigma_y$  = 74 KSI.
2. 5Al-2.5Sn (ELI) Titanium (-423°F).
  - A. UTS =  $\sigma_u$  = 220 KSI.
  - B. YS =  $\sigma_y$  = 210 KSI.

Note that the mechanical properties of the materials used for this investigation are truly representative of the alloys. A comparison of the material properties with previously reported values is shown in Appendix B.

Ground rules for selecting panel maximum test membrane stress were established to provide that either 90% of yield strength,  $\sigma_y$ , or the ultimate tensile strength,  $\sigma_u$ , divided by a factor of safety of 1.4 (whichever gave the lower value) would be used. A second nominal test stress level was taken as 2/3 of the maximum value.

The yield criterion governed the aluminum panel maximum test stress selection, and the ultimate criterion governed the titanium. Since the fixture was completely charged with LH<sub>2</sub> during each test, the mechanical properties at -423°F were used as base strength levels. In general, therefore, the biaxial panels were pressurized to nominal hoop stress,  $\sigma_H$ , at levels of

$$\sigma_H = 0.90 \sigma_y = 67 \text{ KSI}$$

and

$$\sigma_H = 0.60 \sigma_y = 44 \text{ KSI}$$

for the aluminum specimens, and

$$\sigma_H = \frac{\sigma_u}{1.4} = 157 \text{ KSI}$$

and

$$\sigma_H = 2/3 (157) = 105 \text{ KSI}$$

for the titanium panels. Actual measured thicknesses, panel contours, and fixture pressure levels were used for data analysis of each test.

There is an additional material strength consideration that must be considered when analyzing data obtained from biaxial tests of titanium panels. Preceding research at Douglas (Reference 6) has disclosed that the biaxial strength of certain titanium alloys is significantly greater than that predicted by techniques which assume the material is isotropic in nature. Based on Von Mises' criterion for isotropic materials, the 1:1 biaxial yield should be equivalent to the uniaxial yield. Reference 6 indicates the biaxial yield strengths (1:1 stress field @ R. T.) for 5Al-2.5Sn titanium range from 17% to over 35% greater than uniaxial yield values. Corresponding burst strength increases (again 1:1 field) were even higher (percentage measurement) when compared with material ultimate tension strength.

When the panels used for this hypervelocity impact investigation were fabricated by the hydrostatic bulging technique, reduction of some of the panel shape as a function of hydrostatic pressure data indicated that the 1:1 biaxial yield of the 5Al-2.5 Sn (ELI) titanium was approximately 15% above the uniaxial yield. Data obtained during similar work with 2219-T87 aluminum alloy indicated that the 1:1 biaxial yield was very close to the uniaxial yield for that alloy at room temperature.

The precise biaxial strength increase factors for the ELI grade of 5Al-2.5Sn titanium at  $\text{LH}_2$  temperature are not known at present; however, it is thought that the increase factors will be similar to those observed during tests conducted at room temperature.

The actual 1:1 biaxial yield and ultimate strengths at  $-423^\circ\text{F}$  are pertinent for reducing test data and correlating material fracture strength theories with observed behavior of structures subjected to impact loading conditions. Engineering logic indicates that biaxial burst strength increase factors at  $\text{LH}_2$  temperature are perhaps less than those determined at room temperature. Analysis of test results indicated that some increase in the 1:1 biaxial burst (and yield) strength should be considered.

Therefore, the 1:1 biaxial yield strength,  $\sigma_{yB}$ , and biaxial ultimate strength,  $\sigma_{uB}$ , were taken arbitrarily as  $1.15 \sigma_y$ , and  $1.15 \sigma_u$ , respectively, for all of the data analysis work.

## Section 4

### EXPERIMENTAL TESTING APPARATUS

Two different sets of experimental apparatus were used for the two major phases of the research effort. Uniaxial static fracture tests were conducted at the Douglas Materials Research Laboratories with apparatus designed for a concurrent NASA-sponsored research effort, "Research on Growth of Plane-Stress Flaws in Thin Walled Cryogenic Material" by D. A. Eitman and co-workers (NASA Contract NAS 3-4192). The apparatus will be briefly described here.

A rather elaborate testing system was designed, fabricated, and installed in the ballistic range of the Douglas Aerophysics Laboratory (DAL) for the hypervelocity impact phase of the program. The static burst tests of biaxial panels were also conducted, with the  $\text{LH}_2$  apparatus at the DAL Range.

#### 4.1 UNIAXIAL STATIC FRACTURE TEST PROCEDURE

Uniaxial static fracture tests were conducted on fatigue and hypervelocity impact preflawed panels at  $-423^\circ\text{F}$ . In general, the tests were performed by immersing the panels in a cryostat that contained  $\text{LH}_2$  and loading them monotonically to failure.

##### 4.1.1 Test Apparatus

The uniaxial test fixture was capable of testing panels with maximum dimensions of 16 x 42 in. to a load of 150,000 lb at temperatures ranging from room to  $-423^\circ\text{F}$ . Both static and fatigue tests could be performed in the fixture, although all tests in this program were static tests and were conducted at  $-423^\circ\text{F}$ . A photograph of the test fixture is shown in Figure 4-1.

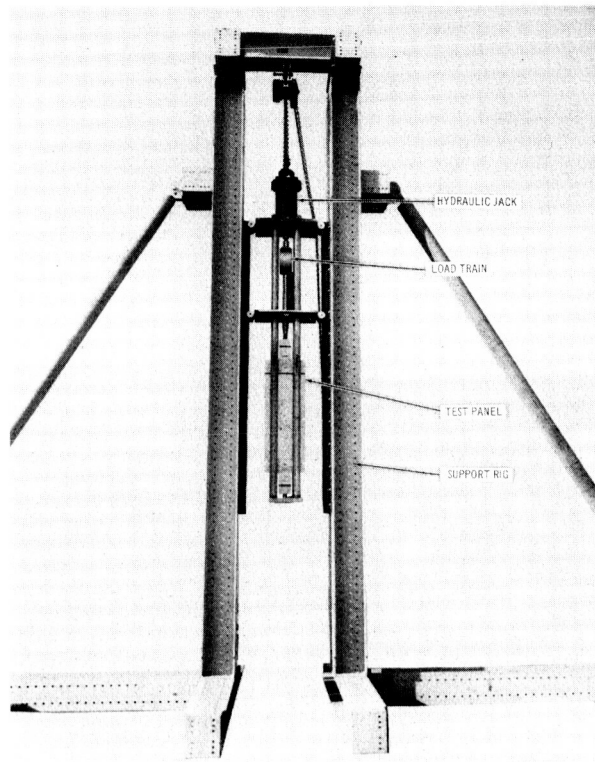


Figure 4-1. Uniaxial Testing Apparatus

---

#### 4.1.2 Specimen Design and Preparation

Uniaxial test panels for the hypervelocity impact effects program were designed for testing in the plane-stress apparatus (NAS 3-4192). Originally, a width of 16 in. was selected for the aluminum panels and a width of 14 in. was selected for the titanium panels. These sizes were chosen so that all attachments in the uniaxial grips would be used. All specimens were loaded so that the direction of stressing was normal to the sheet rolling direction.

The uniaxial test fixture was designed to use a simple bolt and friction clamp joint at the ends of the panels. The sizes of the flaws produced in several of the panels were rather small in comparison to overall panel size. Because similar panels failed in the clamp joint during some preliminary tests, it was decided to modify the panel design slightly to ensure that they would fracture at the region of the flaw. The grip area of several panels was reinforced by application of finger-type doublers and most of the panels were machined to a width of 12 in. in the center section to reduce the cross-sectional

area in the region of the flaw. In selecting panel widths, fracture toughness testing rules-of-thumb indicate that the net fracture stress should be less than 90% of the yield stress if fracture toughness data are to be valid. Fatigue preflawed panel tests met these requirements. Some of the impact preflawed panels fractured at very high stress levels; these stresses, which exceed the usual levels, result from the inherent strength of panels that contain very small impact flaws.

The doublers were fabricated and bonded on two aluminum UH032A#1 and UH032A#3 and all of the titanium impact preflawed panels (see Appendix C for specimen nomenclature). Narmco 7343 epoxy was used to bond the doublers to the panels, and all panels except for two aluminum fatigue preflawed panels that contained long initial preflaws (UF123A#1 and UF032A#1), were machined to the 12-in. width.

#### 4.1.2.1 Fatigue Preflawned Panels

Fatigue starter slots were machined in the center of eight uniaxial panel blanks (two of each gage of each material) by the electrical discharge method (Reference 7 describes the process). The widths of the slots at each end were approximately 0.005-in. wide. The lengths were varied from 0.2 to 1.0 in. in the titanium panels and were varied from 1 in. to slightly over 4 in. in the aluminum panels. These panels were then cycled in a 30,000-lb-capacity uniaxial fatigue machine at ambient temperature (Figure 4-2). Fatigue cracks were grown to lengths from 1/16 to 1/8 in. beyond the end of the machined slots. In general, load levels were selected so that about 30,000 cycles were required to produce the noted flaw sizes. Table C-I (Appendix C) shows the geometry of the fatigue preflaws and the test plan for uniaxial testing of fatigue preflawned panels.

#### 4.1.2.2 Hypervelocity Impact Preflawned Panels

Hypervelocity impact preflaws were produced in the center of 12 uniaxial panel blanks (3 of each gage of each material). The hypervelocity impact shots were made into 2 panels per shot, and impact velocities were in the 22,000-fps range. The titanium panels were impacted by 1/8-in.-diam pyrex glass spheres (40 mg), and the two sheets were spaced 1/4 in. apart. The aluminum panels were impacted by 0.30-in.-diam by 1/4-in.-long Lexan

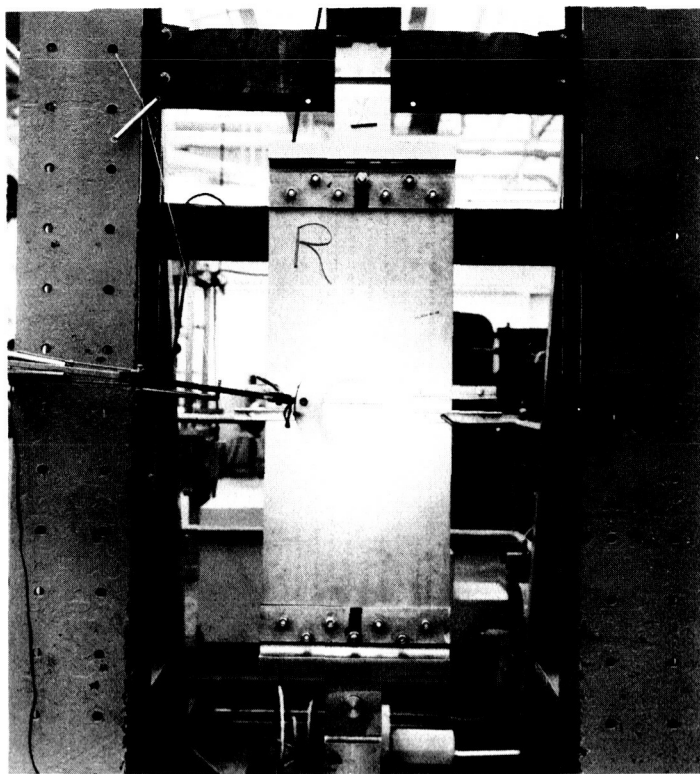
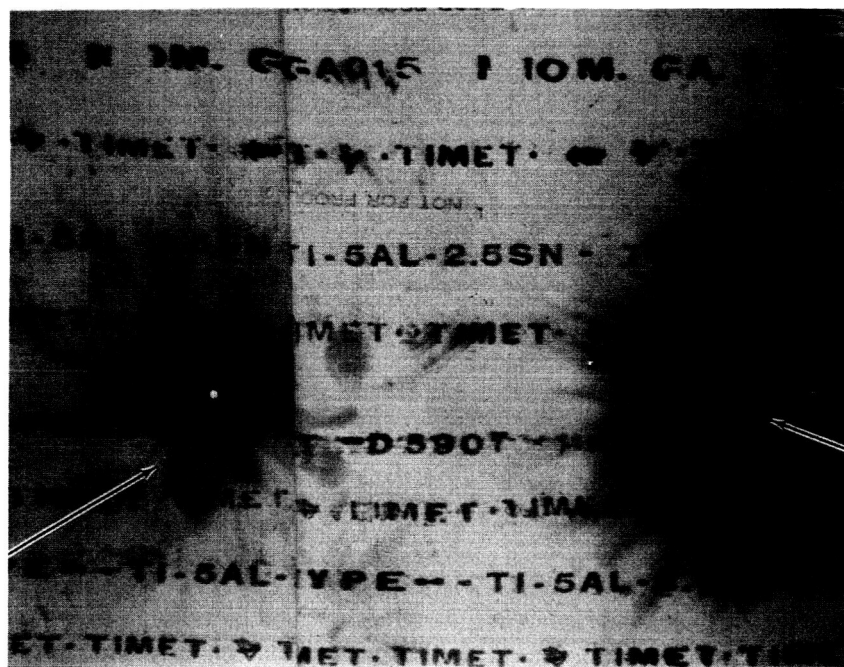


Figure 4-2. Setup for Growing Fatigue Cracks in Uniaxial Panels

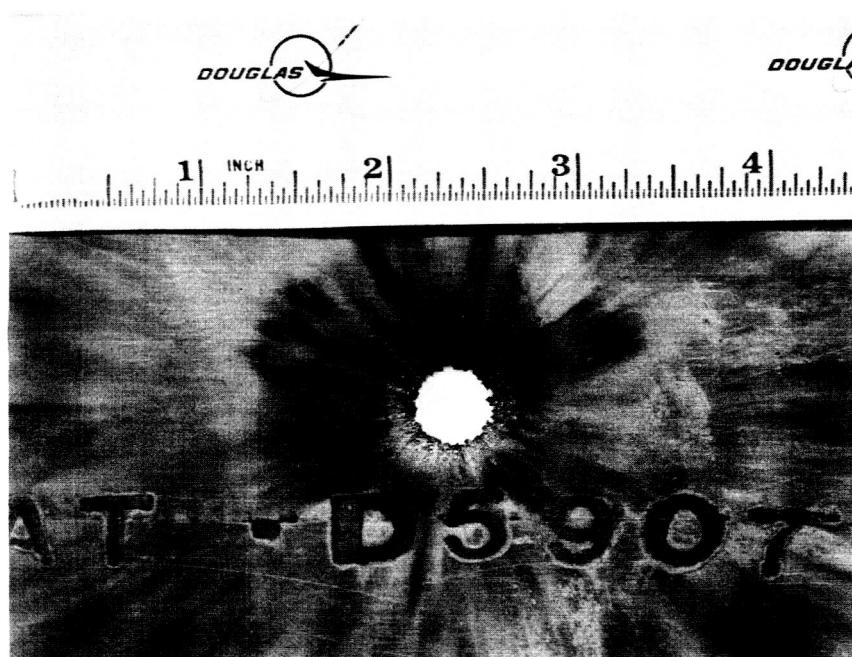
cylinders (400 mg) and the two sheets were spaced 1/2-in. apart during each shot. The impact test configuration selection was based on the results of some preliminary shots that were made on small sheet panels of the aluminum and titanium. It was found that a typical hypervelocity flaw could be produced in each sheet when they were spaced a small distance apart if the projectile had enough energy to completely perforate both sheets. Figure 4-3 is a photograph of the results of a shot into two 0.015-in.-thick titanium panels. The type flaws shown are typical of hypervelocity preflaws produced. Table C-II (Appendix C) shows the geometry of hypervelocity impact preflaws.

#### 4.1.3 Instrumentation

The panels were instrumented with continuity gages which measured the flaw size during the tests. Two different size gages were used: one was 3/4-in. wide and measured crack extensions up to 0.20 in. in 0.01-in. increments; the other gage was also 3/4-in. wide, but measured crack extensions up to 2 in. in 0.10-in. increments. Two small gages were installed on all titanium



a. OVERALL VIEW OF 0.015-IN.-THICK TITANIUM PANELS  
SHOT B8-13



b. CLOSE-UP VIEW OF IMPACT PREFLOWED AREA OF REAR SHEET

Figure 4-3. Typical Primary and Secondary Type Hypervelocity Preflows  
in Uniaxial Panels

panels and on each aluminum panel that contained relatively small size preflaws. Large gages were installed on aluminum panels that contained large preflaws. For intermediate-size flaws, combinations of small and large gages were installed. The gage outputs were traced on a multichannel recorder with load cell outputs, as a function of time.

## 4.2 BIAXIAL STATIC FRACTURE TEST PROCEDURE

As noted in the introductory statement on test apparatus, the biaxial static (burst) tests were conducted with the biaxial test fixture and the  $\text{LH}_2$  pressurizing system that was built for the hypervelocity impact experiments. This equipment is described in detail in Sections 4.3.3 and 4.3.4. In general, a biaxial panel burst test was conducted in the same manner as an impact test except that, of course, the light-gas gun was not fired.

### 4.2.1 Specimen Design and Preparation

Standard biaxial panels were used as test specimens for the biaxial burst tests, and both fatigue preflawed and hypervelocity impact preflawed panels were tested. A group of biaxial panels that contained simple punctures were selected from the remains of specimens from the hypervelocity impact tests as impact preflawed test specimens.

#### 4.2.1.1 Fatigue Preflawed Specimens

Six panels were fabricated and formed to the required spherical contour (forming procedure described in Section 4.3.5). Fatigue starter slots were machined in the center of the six panels by the electrical discharge method. The widths of the slots were made approximately 0.005-in. wide, and the lengths were varied from 0.2 to 1.0 in. Long axes of all slots were parallel to the rolling direction of the sheets. The slots were patched with a non-load-carrying rubber seal, and the panels were installed in a jig which pressurized the panel with hydraulic oil. A pressure cycling system was set up, and fatigue cracks were grown in each of the six panels. Table C-III (Appendix C) shows the geometry of the fatigue preflaws in the biaxial panels.



After the fatigue cracks were grown, the rubber patch was removed and the cracks were sealed with thin (0.005-in.-thick) sheets of Mylar with the edges of the Mylar tacked down with Mylar pressure-sensitive tape. A piece of thin stainless steel shim stock was placed (but not rigidly attached to other parts) between the Mylar patch and the panel. This simple patch worked satisfactorily during the fatigue flawed panel burst tests.

#### 4.2.1.2 Hypervelocity Impact Flawed Specimens

Impact preflawed biaxial burst test specimens were selected from panels used during hypervelocity impact point-load testing that contained simple punctures. Two panels of each gage of each material were selected and prepared for burst testing. Panels with punctures that were at the small end and at the large end of the range of each configuration were selected. However, consideration was also given to the overall structural condition of each panel (in post impact test condition) during the selection process. Some of the panels that survived the point load tests with simple punctures but which were prestressed to the higher membrane stress levels and subjected to high energy level impact shots were rejected as unsuitable for fracture testing. The primary reason for this decision was that the conditions described usually produce general yielding in the region of the panel adjacent to the hole; in some cases local deformations were quite severe. As a geometric description, the shape of these particular panels is characterized here as of volcanic form. The skins are raised in conical form, about the center of the hypervelocity impact crater, above the original spherical surface. Upon post-impact hydrostatic pressurization of such a panel, the 1:1 biaxial membrane stress is modified by the change of shape of the panel as well as by the presence of the punched hole.

Table C-IV (Appendix C) lists the panels that were selected and prepared for burst testing and the test plan for burst testing.

Originally it was planned to statically burst each of the eight panels listed in Table C-IV. However, the panels tested burst at very high stress levels, and it was not possible to fracture certain panels which were made of the thicker gage sheets within the pressurization limitations of the  $\text{LH}_2$  system.

Review of the results of Burst Tests 7 through 13 indicated that the tests, as conducted, did not produce the precise fracture mechanics baseline data desired. All panels which survive impact testing with simple punctures evidently have undergone some yielding (to varying degrees) in the region directly adjacent to the hole; hence, a complicating factor is introduced. Testing was conducted to the stage where, within the design capability of the LH<sub>2</sub> pressurization system, additional runs would produce no further pertinent fracture data, and so then testing was discontinued.

The impact preflaws were sealed in the same manner as that described in the preceding section except it became necessary to improve the patching system for the higher pressure tests; the simple patches leaked somewhat at the higher test pressures. To fix the patch leakage problem, a one-half mil Mylar sheet that covered the entire back surface of the panel was placed between the panel and the test fixture. This leak repair proved effective.

#### 4.2.2 Biaxial Panel Instrumentation

Two types of measurements were made during the biaxial panel static fracture test sequence. First, it was required that the panel hoop stress,  $\sigma_H$ , be accurately defined. The measurements made for determination of the basic stress state were of panel shape and fixture hydrostatic pressure. The apparatus described in the section on biaxial panel instrumentation was used; however, some slightly different techniques were used to measure preflawed panel shape. Second, it is essential that any slow growth be recorded if correlation using fracture mechanics analysis techniques were to be made.

The shape of each panel was carefully measured up to and beyond the material yield strength pressure levels (and recorded) during the initial hydrostatic bulge form operation. For the fatigue preflawed panels, measurements of panel contour were again taken at room temperature after the panel was installed in the LH<sub>2</sub> biaxial test fixture. The remote controlled spherometer was adjusted to one side of the panel centerline so that the center leg did not rest exactly on the fatigue-crack slot. Local bulging of the panel at the slot would cause mismeasurement of general panel curvature. The room temperature measurements were compared with those taken during the original forming

operations, and were found to be in reasonable agreement. Measurements were also taken after the fixture was charged with  $\text{LH}_2$ . All measurements on the fatigue flawed panels, both at room and at  $\text{LH}_2$  temperature, were taken only to safe hoop stress levels. If a catastrophic fracture had occurred during the time the spherometer was on the panel, the instrumentation would have been destroyed. The panel shape measurements were extrapolated from the maximum values obtained at  $\text{LH}_2$  temperature to the panel fracture conditions. Extrapolated panel shape measurements as a function of fixture hydrostatic pressure were compared with numerous similar traces taken during the hypervelocity impact phase of the program. These were within the general accuracy of the basic instrumentation readout.

For the hypervelocity impact preflawed panels, panel shapes were calculated from the data taken during each impact shot. However, these data were only taken of pressure levels that produced stresses in the vicinity of material yield strengths. All impact preflawed panels fractured at higher stress levels than expected; panel shapes data were again extrapolated to higher pressure levels. It is not claimed that this procedure is highly accurate. Note again that local deformations of the panels produced significant effects on panel fracture behavior. Future work of this nature should include much more elaborate panel shape measuring instrumentation.

Instrumentation to monitor any growth of the preflaws during the application of hydrostatic pressure loadings was also used during each burst test. Two types of systems were used.

#### 4.2.2.1 Fatigue Preflawed Panel Crack Growth Instrumentation

Foil type continuity gages as described earlier were installed on the six fatigue preflawed panels to record slow crack growth during each burst test. Two gages were installed at each end of the fatigue flaw; small gages were mounted at each end of the flaw on each titanium panel and on the thin gage aluminum panel that contained a relatively small fatigue flaw. Both a small and a large gage were mounted at each end of the flaw on the two aluminum panels that contained relatively large fatigue flaws. The signals from each continuity gage output channel were recorded, along with the fixture

hydrostatic pressure, on a multi-channel Y-t recorder. The tips of the progressing cracks were contained within the instrumented area on each panel up to the instant of catastrophic fracture.

#### 4.2.2.2 Impact Preflawn Panel Crack Growth Instrumentation.

Before actual testing, it was not known whether there would be any slow growth of cracks from the impact flaws (analogous to that observed during tests of fatigue flawed specimens) during the static burst tests. The foil type continuity gages could not be used as there was no reliable method of predicting the point of initiation, around the periphery of the punched hole, and the direction of the final fracture propagation paths.

Cinematography of the front face of the panels was selected as the data instrumentation for this series of burst tests. A jig was built to locate the exact center of the puncture in each panel, and a series of concentric circles were scribed, using a pair of machinist dividers, around the hole on the front face of the panel. The contrast between the panel surface and the fiducial scribe lines was enhanced by first painting the panel with dark blue machinist layout dye. A standard 16mm movie camera was set in the range tank about four feet in front of the biaxial test fixture. A 4-in.-focal-length lens was used to provide a 3 x 4 in. field of view. The camera was protected by a steel armor plate that contained a heavy acrylic plastic viewing port. Standard spot lights were used for illumination, and ASA 400 speed, black and white film was used in the camera.

The resolution of the resulting photorecorded data was good; the scribe lines were bright and clear. It appears, from examination of enlargements of the film strip, that any slow growing cracks in the region of the impact flaw (before the instant of catastrophic fracture) would be discernable. No slow growth crack extension from the impact flaw is shown by the photorecorded data (Figure 4-4).

The figure shows the last two frames taken before the panel fractured and a frame in which there are indications of the actual fast propagating crack. The camera was operated at a framing rate of 48 frames per second during

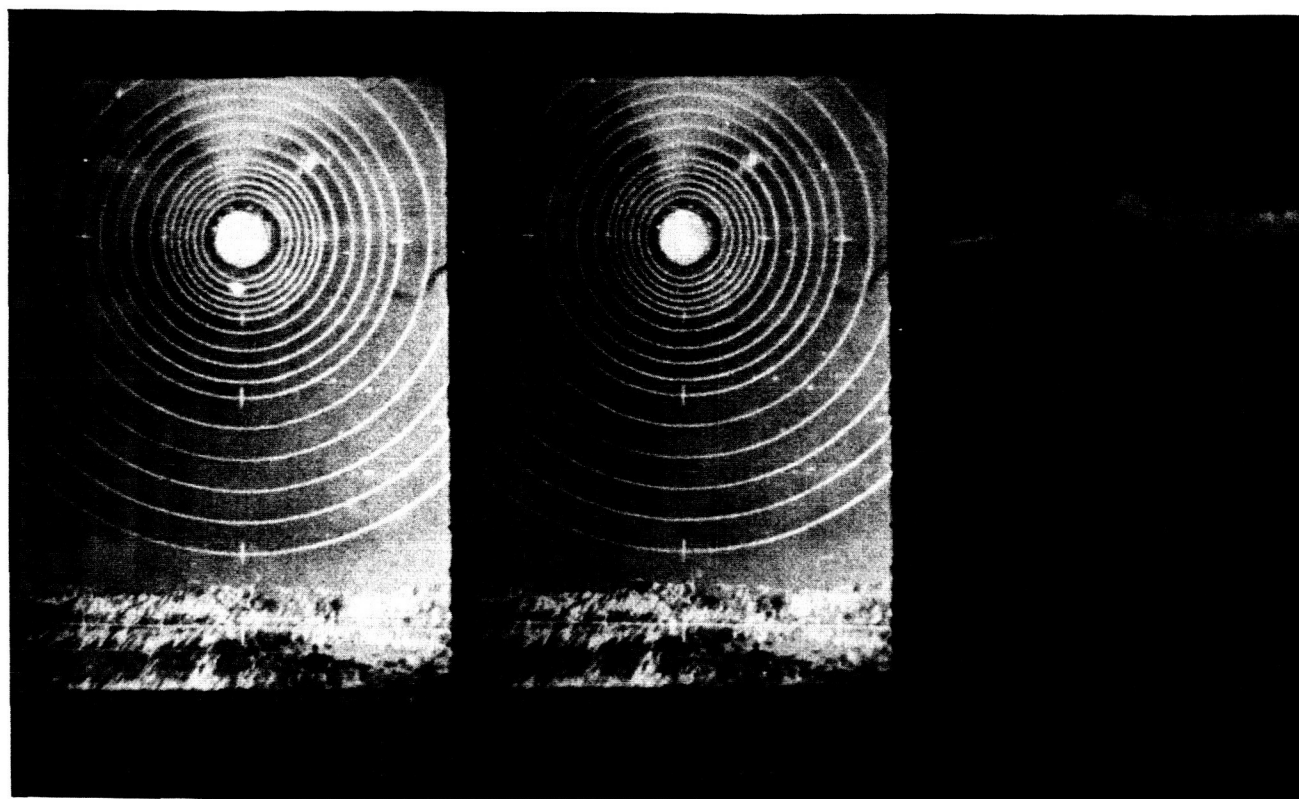
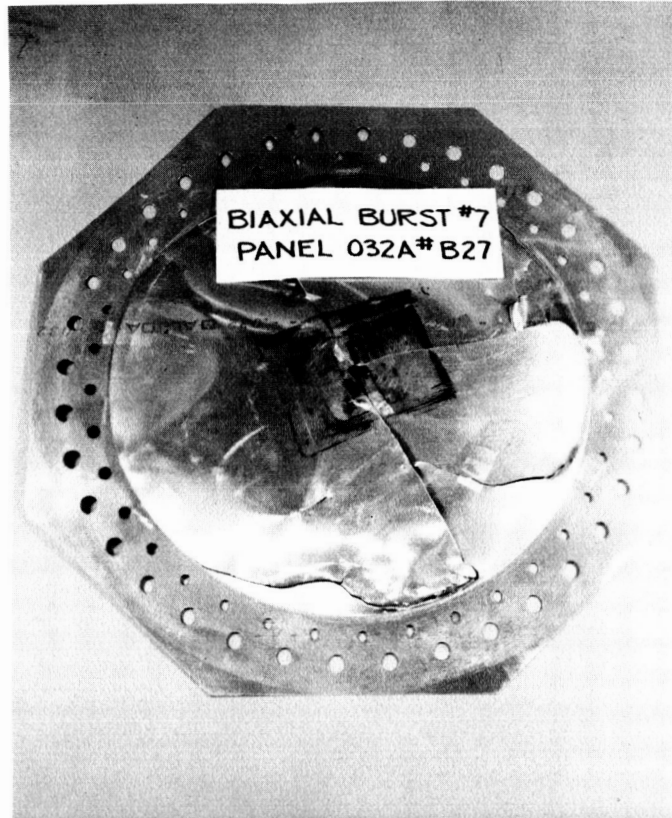


Figure 4-4. 16mm Camera Photorecording – Burst Test No. 7

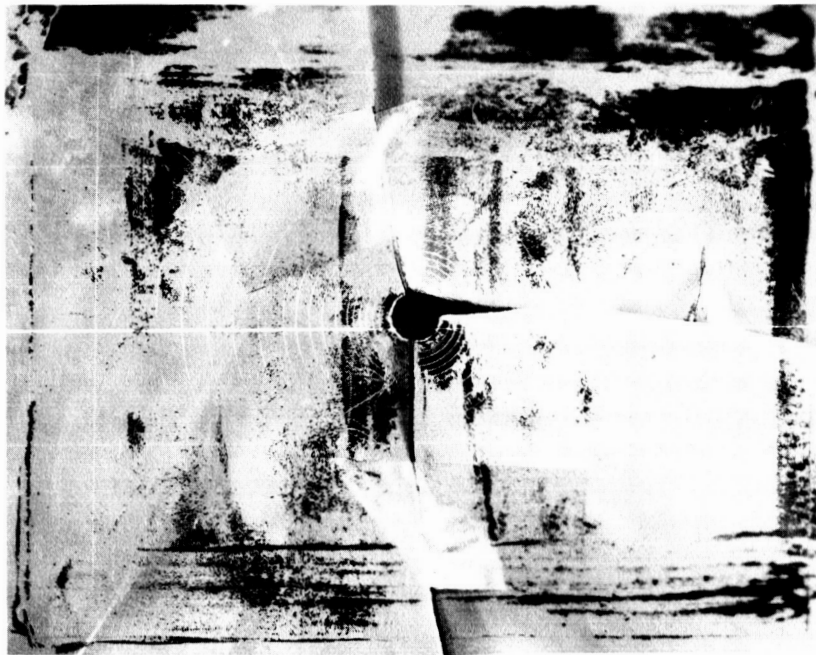
this test sequence. The panel loading hydrostatic pressure was steadily increased from the minimum value (1 atm minimum differential in the ballistic range LH<sub>2</sub> set-up) to that producing panel burst in approximately 1 min. elapsed time. Figure 4-5 shows the post-burst-test condition of the same panel. Note the correspondence of the fracture paths shown by this photograph with the indications shown by the third 16mm frame of Figure 4-4.

#### 4.3 HYPERVELOCITY IMPACT TEST PROCEDURE

The impact experiments were conducted in the ballistic range at the Douglas Aerophysics Laboratory, El Segundo, California. The experiment arrangement of the ballistic range is shown schematically in Figure 4-6. Figure 4-7 is a photograph of a portion of the facility. The range consists of a two-stage light-gas gun, a blast chamber, and a range tank that is 10-ft in diameter by 100 ft long. Apparatus for holding and pressurizing the biaxial test panels was located approximately at mid-station in the range tank. The



a) OVERALL VIEW OF TEST PANEL



b) CLOSE-UP HYPERVELOCITY PREFLAW

Figure 4-5. Post Test Condition of Test Panel – Burst Test No. 7

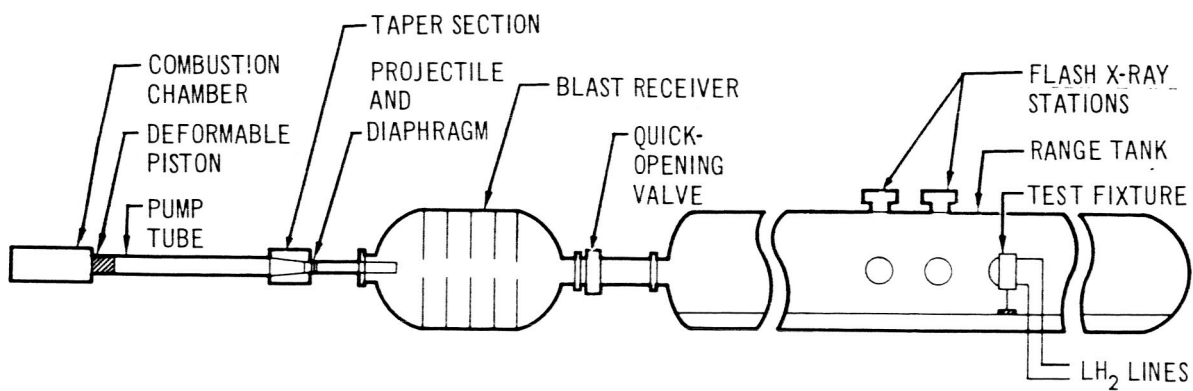


Figure 4-6. Schematic of Douglas Aerophysics Laboratory Ballistic Range

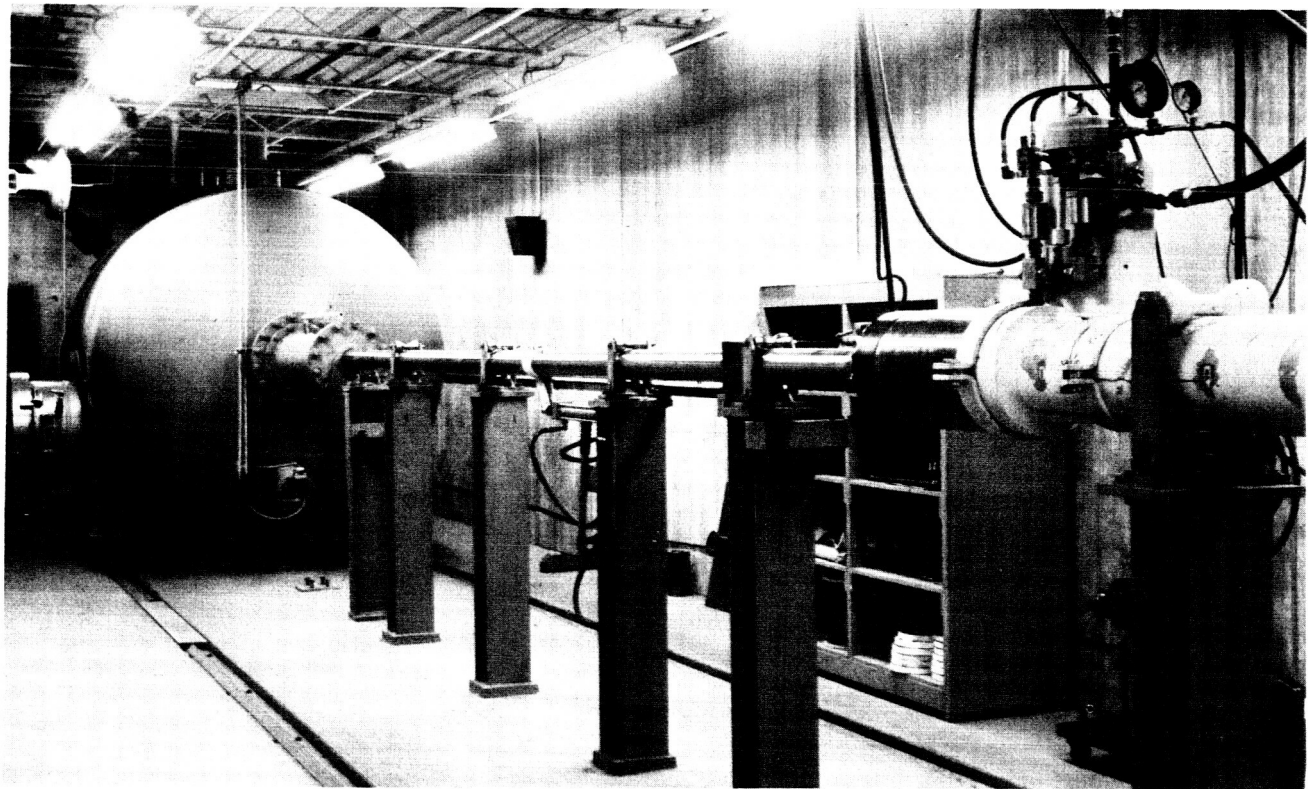


Figure 4-7. Ballistic Range Light Gas Gun

loading fixture and  $\text{LH}_2$  handling apparatus was designed and built especially for the program.

#### 4.3.1 Projectile Launching Equipment

The light-gas gun used for the experiments has a 0.25-in. -diam nominal bore launch tube, and was designed to operate like the gun described in Reference 8. Light-weight (about 0.1 g) Lexan (a polycarbonate) cylindrical projectiles can be launched to velocities in the high 20,000 foot per second (fps) range with this particular system. To launch the required range of projectile sizes required for this program, various size launch tubes were used; bore diameters ranged from 0.280-in. to 0.360-in. diameter. Total launch weights (sabots plus projectiles) ranged from about 0.2 to 0.6 g. Projectile velocities averaged about 22,000 fps (at the instrumentation stations, just uprange from the target fixture) and gun loading parameters were selected to maintain a constant velocity, of this order, during each shot. Because of the expense associated with each  $\text{LH}_2$  test run, this moderate projectile launch velocity range was selected; that is, clean-shooting reliability was given priority over all-out efforts to push launch velocities to the upper (for light-gas gun) limits. There is a natural tendency for the velocity performance of a given basic gun configuration to be degraded slightly as launch mass increases.

#### 4.3.2 Projectile Characteristics

Either aluminum spheres or Lexan cylindrical slugs were used as test projectiles throughout the course of this program. The only exceptions were the first two  $\text{LN}_2$  check-out shots where pyrex glass spheres were used as projectiles. Commercially-manufactured precision aluminum balls, ranging in size from 1/16 to 1/4-in. -diam, were used; the diametrical tolerance on each lot of balls was -0 to +0.0005 in., individual balls of the same size were from the same manufacturing lot, and were of identical weight (to  $\pm 1$  mg measured by a laboratory balance). The values listed in Table 4-I are the average of the weight measurements of 10 aluminum balls of each basic size; the table values were used for reduction of data from impact tests where the aluminum projectiles were used. All aluminum projectiles were launched in a sabot.



Table 4-1  
CHARACTERISTICS OF ALUMINUM SPHERICAL PROJECTILES

Projectile Diameter (in.)                      (mm)		Projectile Weight (mg)
1/16 (0.0625)	1.59	6.0
3/32 (0.0937)	2.38	20.0
1/8 (0.1250)	3.18	47.3
5/32 (0.1562)	3.97	92.0
3/16 (0.1875)	4.76	159
7/32 (0.2194)	5.56	253
1/4 (0.2500)	6.35	378

The Lexan cylindrical projectiles were machined by Douglas as required. Two sizes were used. One set was nominally 0.280-in. -diam by 0.200-in. -long, with an average weight of about 0.22 g. The larger size was nominally 0.350-in. -diam by 0.350-in. -long, with an average weight of about 0.57 gm. The weight of each Lexan projectile was measured, recorded, and used to reduce the impact test data for that particular shot.

#### 4.3.2.1 Projectile Velocity and Integrity Instrumentation

Projectile velocity was measured by a flash X-ray shadowgraph system that was located just up-range from the biaxial test fixture. The system consisted of two stations which were 5 ft apart. The trigger system for the first X-ray station consisted of a light screen and a photomultiplier monitor and readout system. This station recorded a shadowgraph of the projectile in the as-launched condition. The trigger system of the second X-ray station consisted of a thin (1/2 mil) Mylar yaw screen and photocell monitor. The light flash given off as the projectile punctured the screen provided the sequencing signal. Appropriate time delays were provided in the electronic circuits so that the X-ray tube was discharged at a time when the projectile was at, or near, the center of each instrumentation station. The Mylar yaw screen substantiated the cleanness of the shot. The second X-ray shadowgraph substantiated the integrity of the projectile after passage through the

yaw screen. The time duration between the discharges of the two X-ray tubes was measured and recorded by a 10-mc electronic counter. With this system, the projectile impact velocity was calculated to within 1%.

#### 4.3.2.2 Statistical Analysis of Impact Velocity

A distribution of measured values of projectile impact velocity (as measured by the flash X-ray instrumentation system) for 70  $\text{LH}_2$  test runs is shown in Figure 4-8. The most probable value for impact velocity is 21,660 fps with a probable error of the mean equal to 70 fps. The standard deviation,  $s_o$ , is 850 fps and with a value of  $1.64 s_o$  (90% probability all deviations within the chosen limit) the projectile impact velocity may be taken as  $21,660 \pm 1,450$  fps for this study.

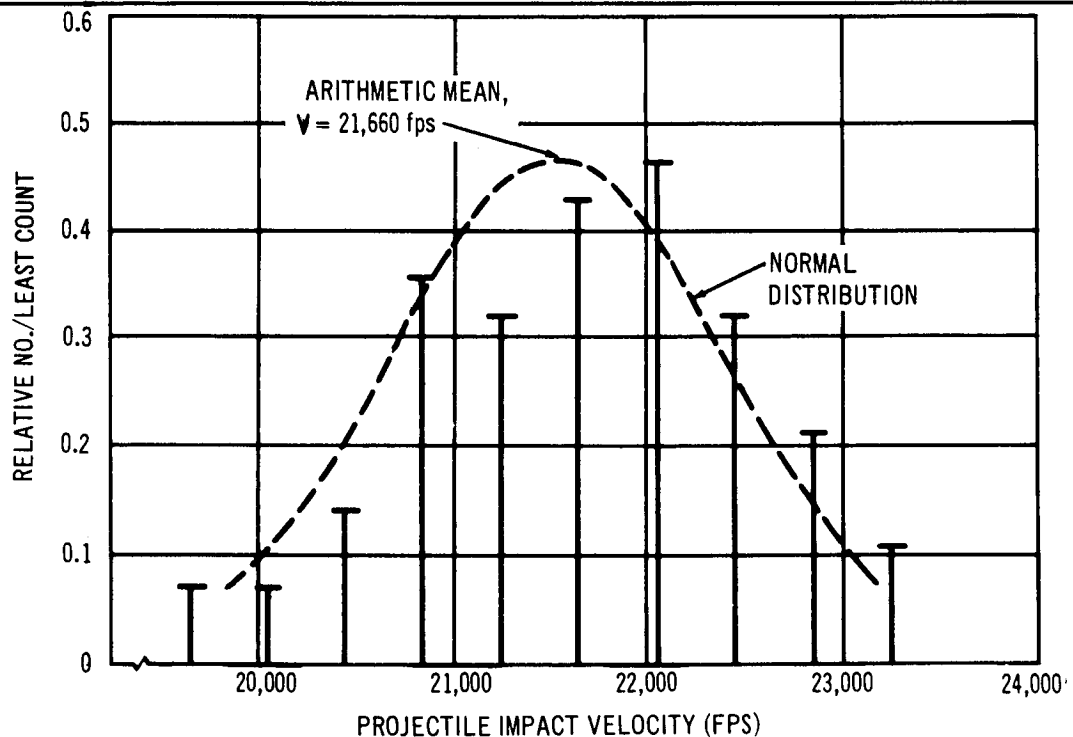


Figure 4-8. Observed Distribution of Impact Velocity

#### 4.3.3 Installation of an LH<sub>2</sub> System at the Douglas Ballistic Range

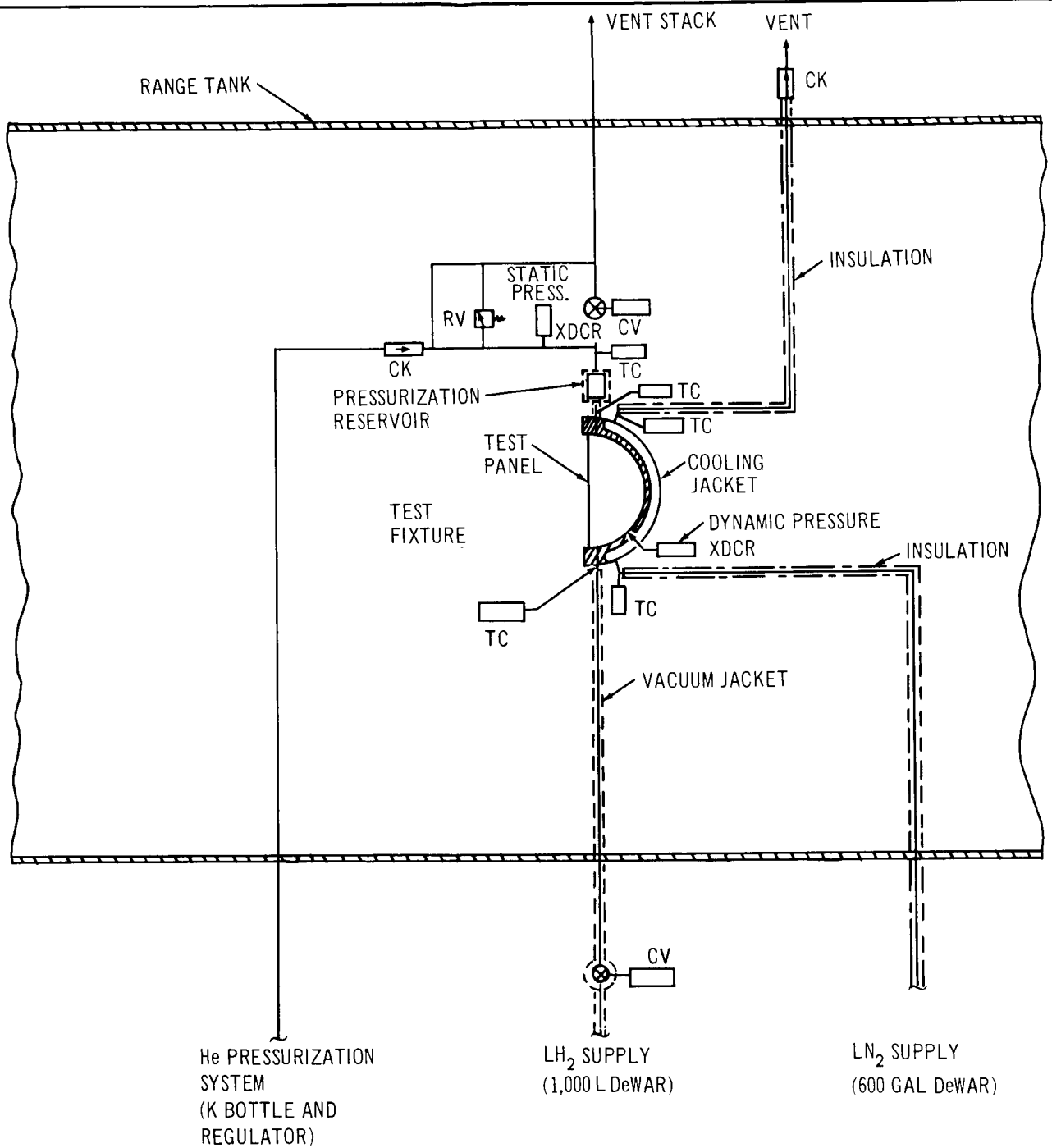
Figure 4-9 is a schematic of the LH<sub>2</sub> system that was built into the ballistic range and Figure 4-10 shows some of the plumbing as installed. During the initial liquid nitrogen shots, the LH<sub>2</sub> Dewar vessel was left unconnected, and the LN<sub>2</sub> Dewar was simply attached to the cryogenic transfer lines that feed the main chamber of the test fixture (Figure 4-11). All control valves for LH<sub>2</sub> operation were remotely operated, and pressure and temperature instrumentation was read remotely in the control room. As a safety measure, a 10-ft-high earth-filled barricade was built around the LH<sub>2</sub> Dewar vessel site at the side of the range tank.

The levels of the cryogenic fluids were monitored by thermocouples at the locations shown on the schematic. During a typical LH<sub>2</sub> test, the fixture was first precooled to -320°F by charging the cooling jacket with liquid nitrogen (LN<sub>2</sub>). The main chamber was then charged with LH<sub>2</sub> until the thermocouple above the pressurization reservoir indicated the liquid level was at, or above, this location. Purpose of the reservoir was to ensure that the main chamber remained full of hydrogen in the liquid phase throughout the critical sequence of test events. Tests were not completed unless the thermocouple just below the reservoir showed that liquid was still above that level.

#### 4.3.4 Biaxial Fixture Design

A test fixture capable of biaxially stressing test panels made from the selected aluminum and titanium alloy sheet material to the design membrane stress levels, with LH<sub>2</sub> as the pressurizing medium, was designed and built. The fixture, as shown by Figure 4-12, is basically a hemispherical container. Test panels were bolted to the front face by means of a bolt circle and a clamp ring. The fixture contained ports for direct attachment of the LH<sub>2</sub> fill and vent lines. A precooling jacket was formed with a secondary shell which was welded on the back of the biaxial test fixture. The secondary shell incorporated connections for cryogenic lines.

The shell of the fixture was made from 6061-T6 aluminum alloy, and fasteners for the hold-down ring attachment were made from A-286 stainless steel. In general, all other metallic items of the assembly were of various aluminum and stainless steel alloys. Encapsulated spring-loaded tubular Teflon O-rings



KEY TO SYMBOLS

CV CONTROL VALVE	RV PRESSURE RELIEF VALVE
CK CHECK VALVE	TC THERMOCOUPLE
XDCR PRESSURE TRANSDUCER	

Figure 4-9. Ballistic Range LH<sub>2</sub> System Schematic

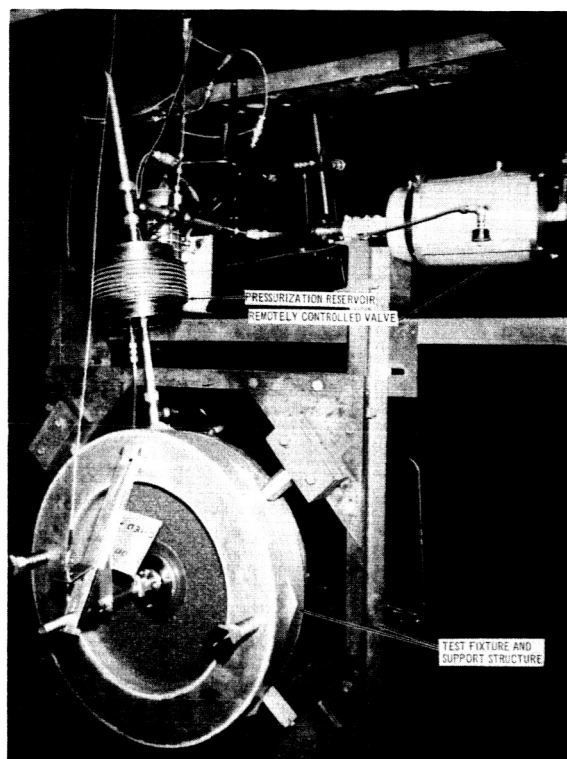


Figure 4-10.  $\text{LH}_2$  System Installation in the Ballistic Range

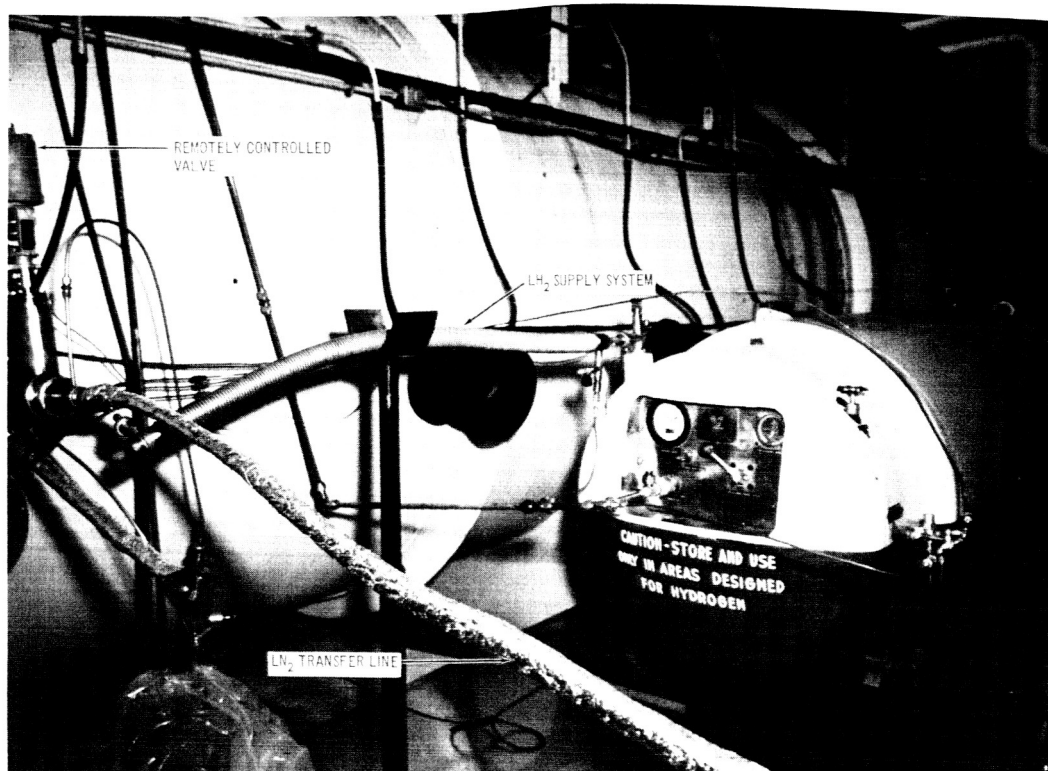


Figure 4-11.  $\text{LN}_2$  and  $\text{LH}_2$  Supply System at the Ballistic Range

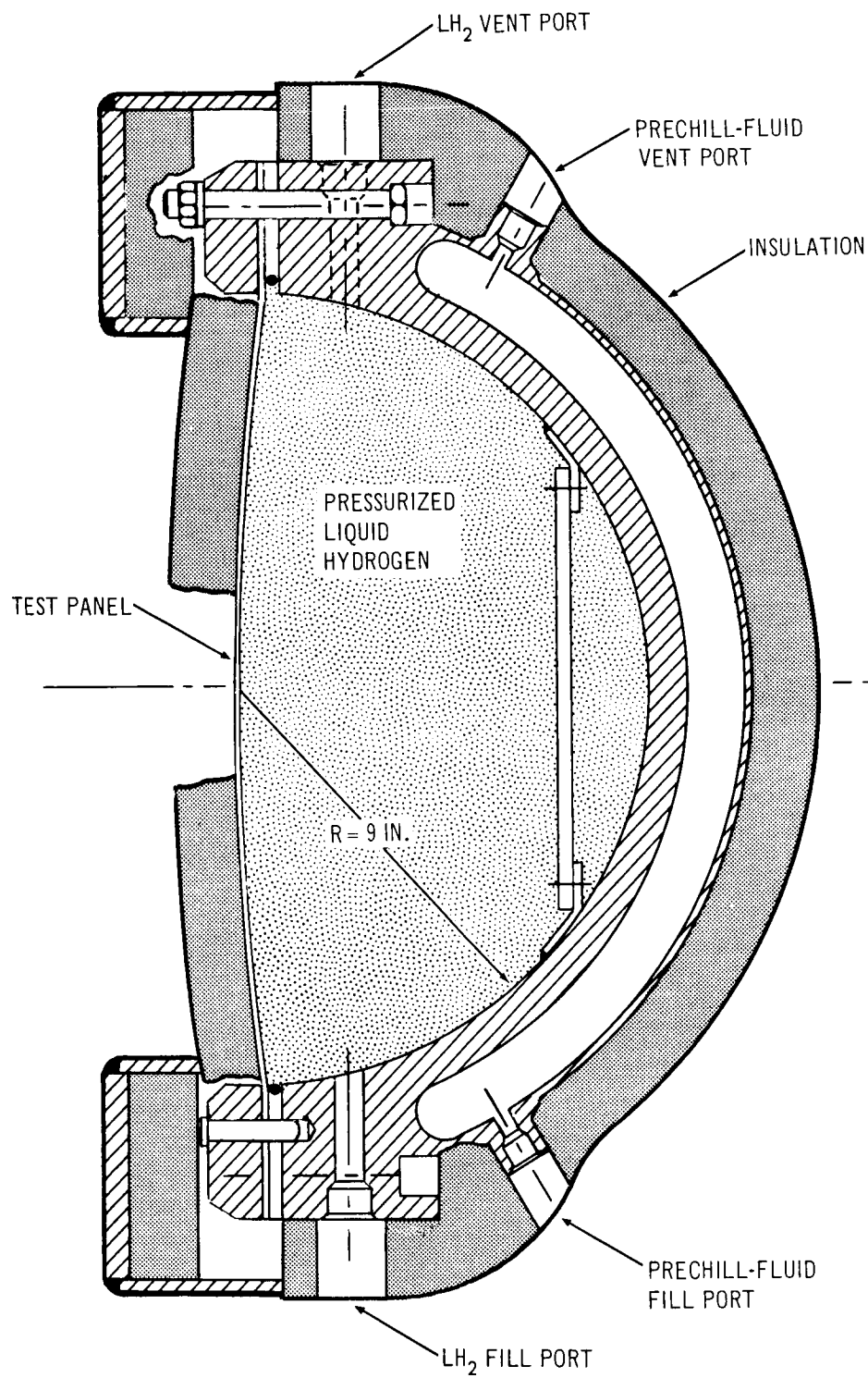


Figure 4-12. Biaxial Cryogenic Test Fixture

were used as the primary seals because they were relatively inexpensive and were reuseable.

A 1/2-in. -thick aluminum plate was mounted just in front of the back spherical surface of the  $\text{LH}_2$  chamber to catch particles of debris that completely traversed the  $\text{LH}_2$  chamber during the hypervelocity impact tests.

The volume of the internal  $\text{LH}_2$  chamber of the biaxial test fixture was approximately  $1 \text{ ft}^2$ .

#### 4.3.4.1 Biaxial Fixture Instrumentation

In addition to the thermocouple and static pressure transducers shown in Figure 4-9 that were installed in the  $\text{LH}_2$  system, a set of dynamic pressure transducers was mounted directly in the  $\text{LH}_2$  chamber of the biaxial test fixture. This instrumentation measured the characteristics of the  $\text{LH}_2$  shocks during the impact tests. Figure 4-13 shows the installation. The transducers were quartz crystal piezoelectric pickups and two different models were used.

The forward transducer No.  $K_1$  was rated to a maximum pressure of 30,000 psi while the remaining two gages, No's.  $K_2$  and  $K_3$  were rated to 15,000 psi maximum pressure loadings. The rise time of these gates was on the order of  $3 \mu\text{sec}$ . Although this response time is not nearly fast enough for the signal traces to follow the true shape of a sharp-edge rapid-decay shock, the time of arrival of the shock at the instrumentation stations can be fairly accurately determined. Shock velocity measurements are sufficiently accurate, however, to form the base for deducing an expression that characterizes the  $\text{LH}_2$  shock.

The signals from the piezoelectric transducers were conditioned and amplified by charge amplifiers and then fed to two or more dual-beam oscilloscopes. Pressure as a function of time traces were photorecorded by still cameras which were mounted on the face of the oscilloscopes. Traces from transducers No.  $K_1$  and  $K_2$  were displayed on one scope and traces from transducers No.  $K_1$  (or  $K_2$  in some runs) and  $K_3$  were displayed on a second

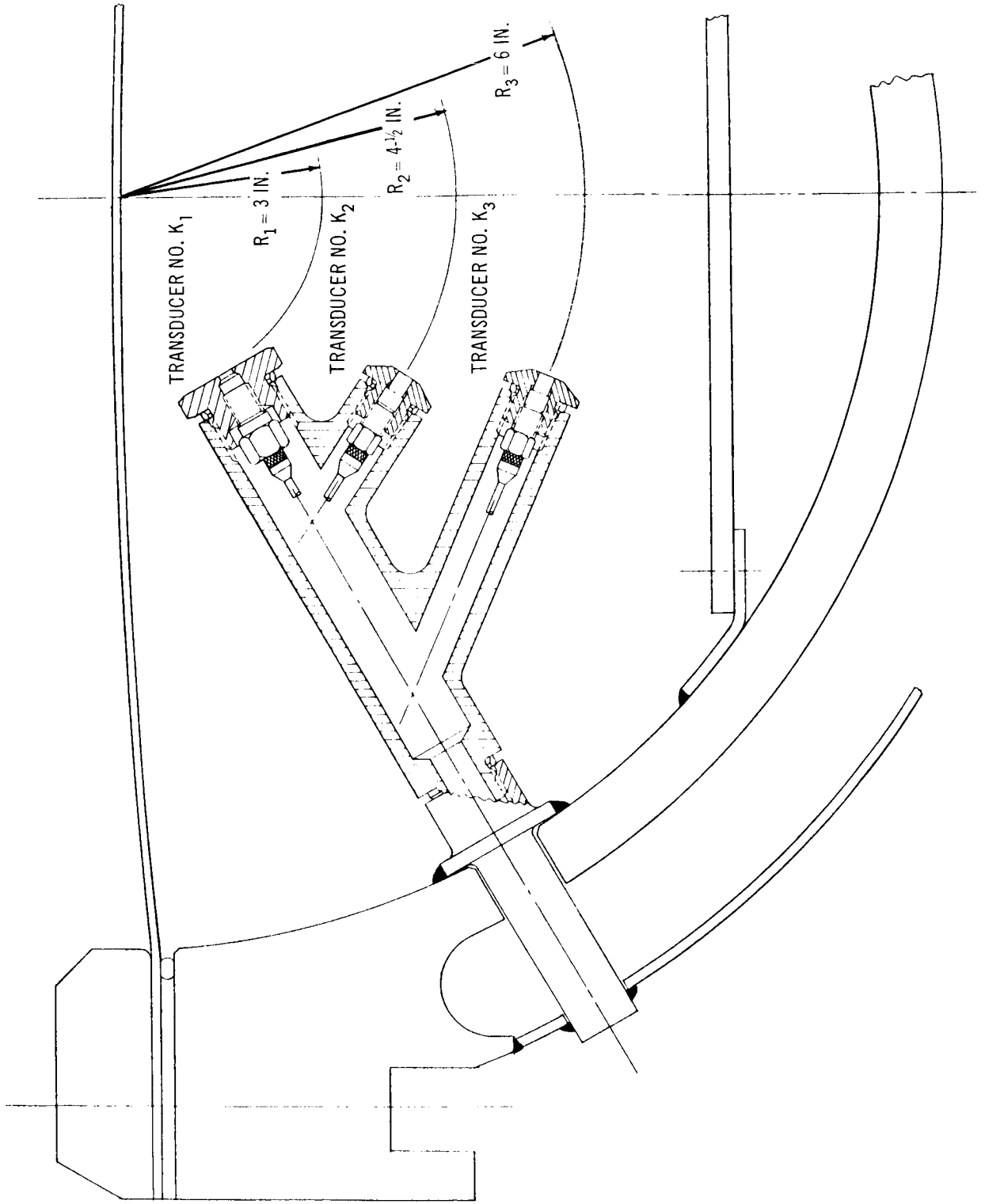


Figure 4-13. Dynamic Pressure Transducer Installation



dual-beam oscilloscope. Thus the time base for each transducer can be related to those of the other pressure pickups.

The dynamic-pressure-recording oscilloscopes were triggered by a signal from a photocell which was focused on the front face of the test panel. During the major part of the test effort, where the entire front of the fixture was enclosed in a helium purge tent, the traces were usually triggered just before the projectile actually impacted the target panel.

Similar electronic systems were used at other locations in the range to provide instrumentation sequencing signals. The array of data recording apparatus is shown in Figure 4-14.

#### 4.3.5 Biaxial Panel Design and Fabrication

The biaxial panels had a 24-in. overall outside diameter with a free 18-in. diameter dimension inside the area of the clamp ring, and were designed to simulate the shell of a 78-in. spherical-radius propellant tank. Two methods

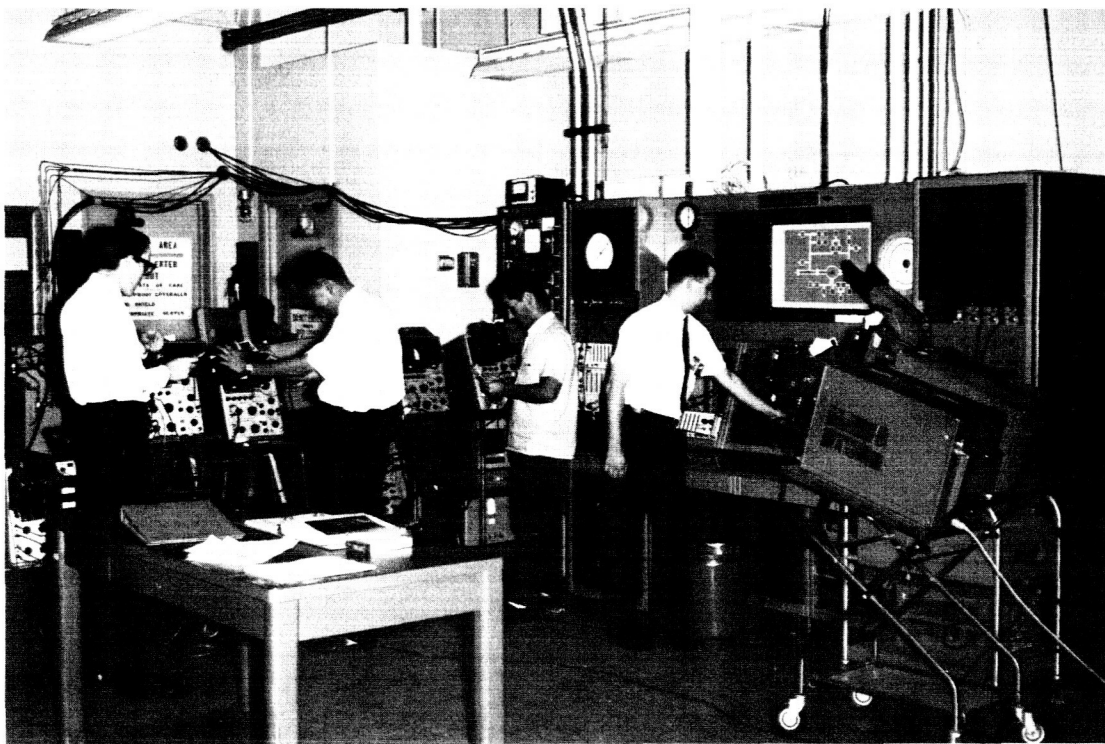


Figure 4-14. Data Readout System and Ballistic Range Control Console

were considered for forming the panels to the desired spherical radius. One approach was to hydropress the panels, and some actual development work with this approach was accomplished. The high spring-back characteristics of the sheet material gave problems, however, and the hydropress approach was abandoned. The use of more complicated manufacturing techniques, such as stretch and hot forming, were considered, but they would have required extensive tooling development, which did not appear warranted.

The biaxial test fixture had been designed so that it was capable of hydrostatically forming the panels and this approach was then evaluated. The results were good and the method was selected for forming the panels. To form the panels by the hydrostatic bulge technique, panels in flat sheet form were bolted in the regular biaxial test fixture, the fixture was connected to a hydraulic stand and a pressure transducer was mounted in the hydraulic system. The pressure transducer output was recorded on a X-Y plotter. Figure 4-15 shows the setup for the hydrostatic forming procedure. Panel shapes were measured during the runs. The dial indicator reading is readily related to spherical radius (Figure 4-16). Also shown are the spreads in dial

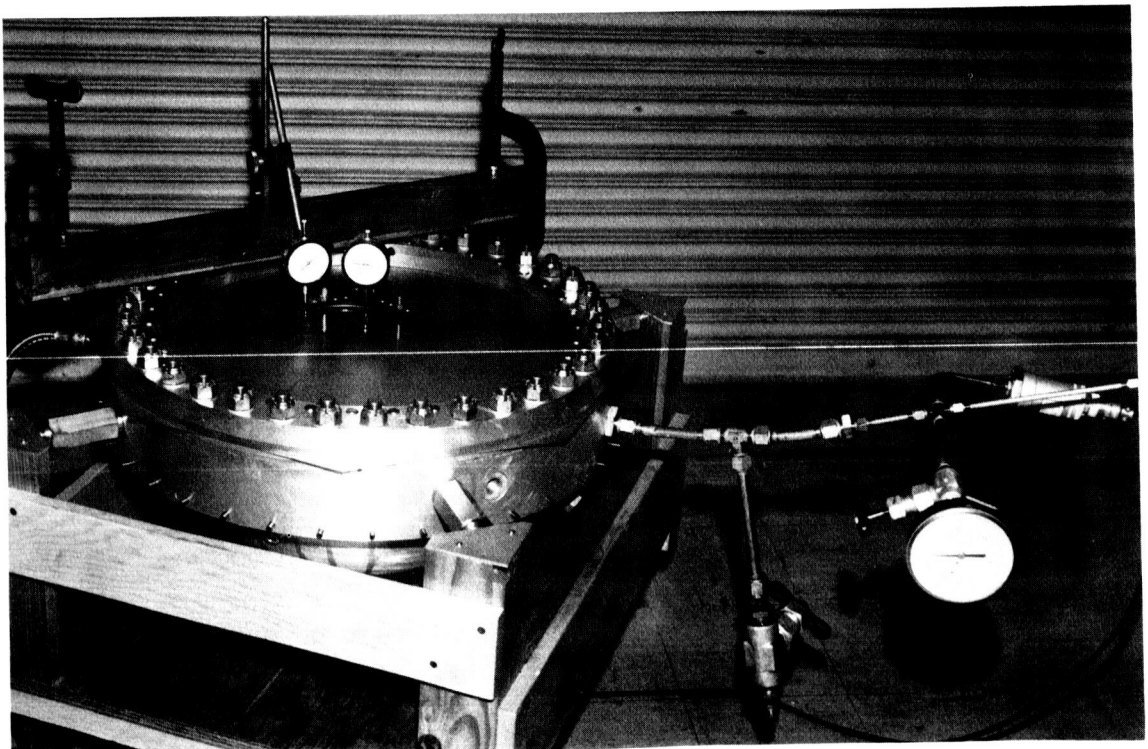


Figure 4-15. Setup for Hydrostatic Bulging of Biaxial Panels

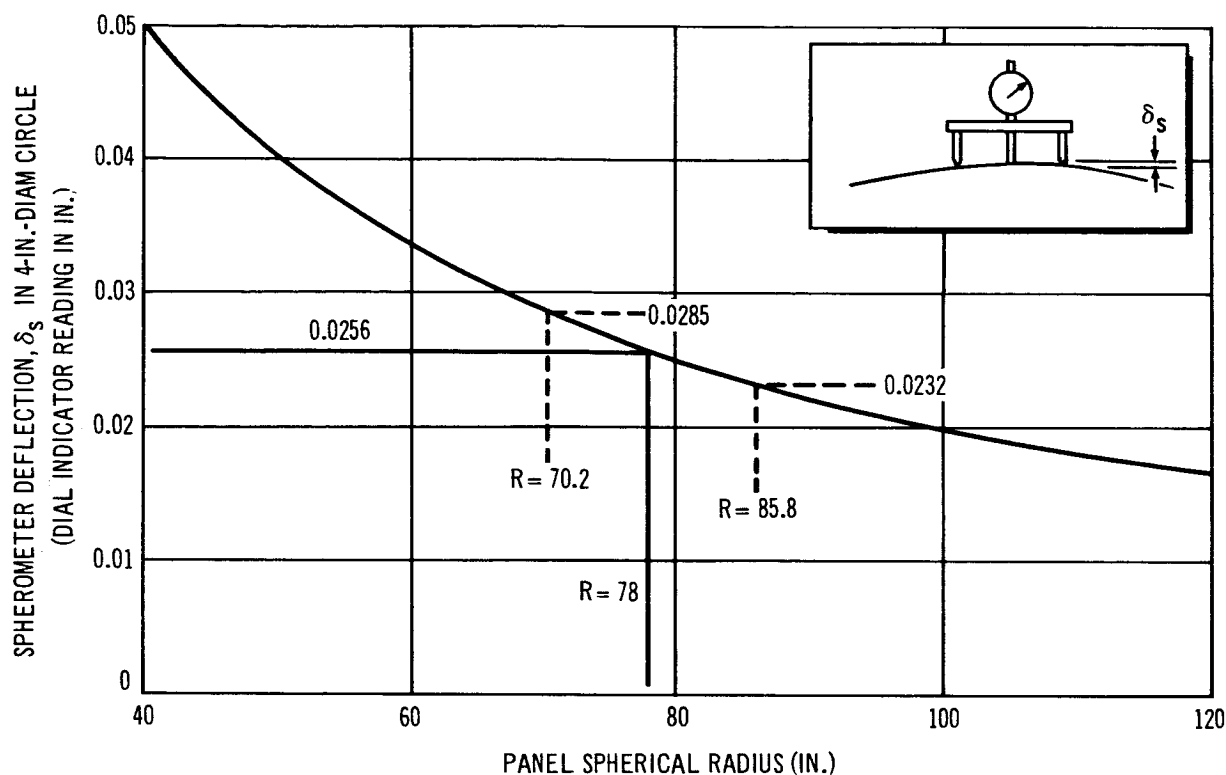


Figure 4-16. Relation of Spherometer Reading to Spherical Radius

indicator reading for a  $\pm 10\%$  tolerance on the spherical radius of the panel. The 10% tolerance was selected as a specimen design configuration requirement. The system was pressurized and panel contour readings were taken. After each increment of load, panel residual contour measurements were taken. By projecting the residual contour measurements it was possible to stop at the proper pressurization level. Figures 4-17 and 4-18 show sample plots of some of the data obtained for the 0.032-in.-thick aluminum panel B02. Figure 4-19 shows the variation of spherical radius with radial locations from the center of the panel at three levels of hydrostatic pressure.

All of the panels as formed were somewhat non-uniform in spherical contour at zero (or very low) internal pressure. A pattern of medium curvature existed at the apex (or center), and this curvature first decreased out in the radial direction, then increased rapidly near the edges of the hold down ring.

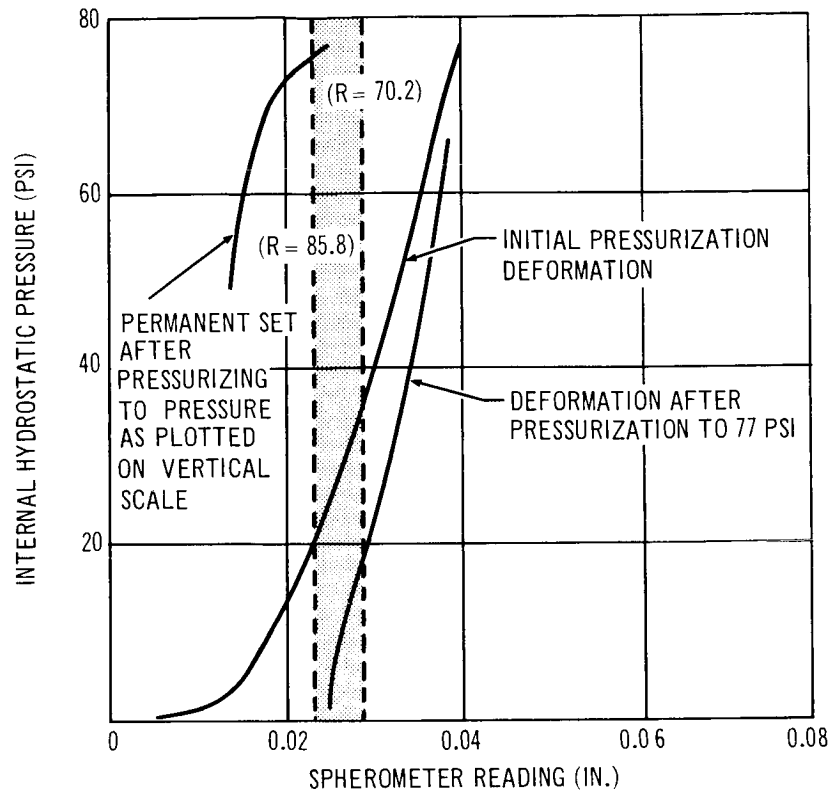


Figure 4-17. Forming of Bulged Biaxial Panels (0.032-Gage Aluminum Panel No. B02)

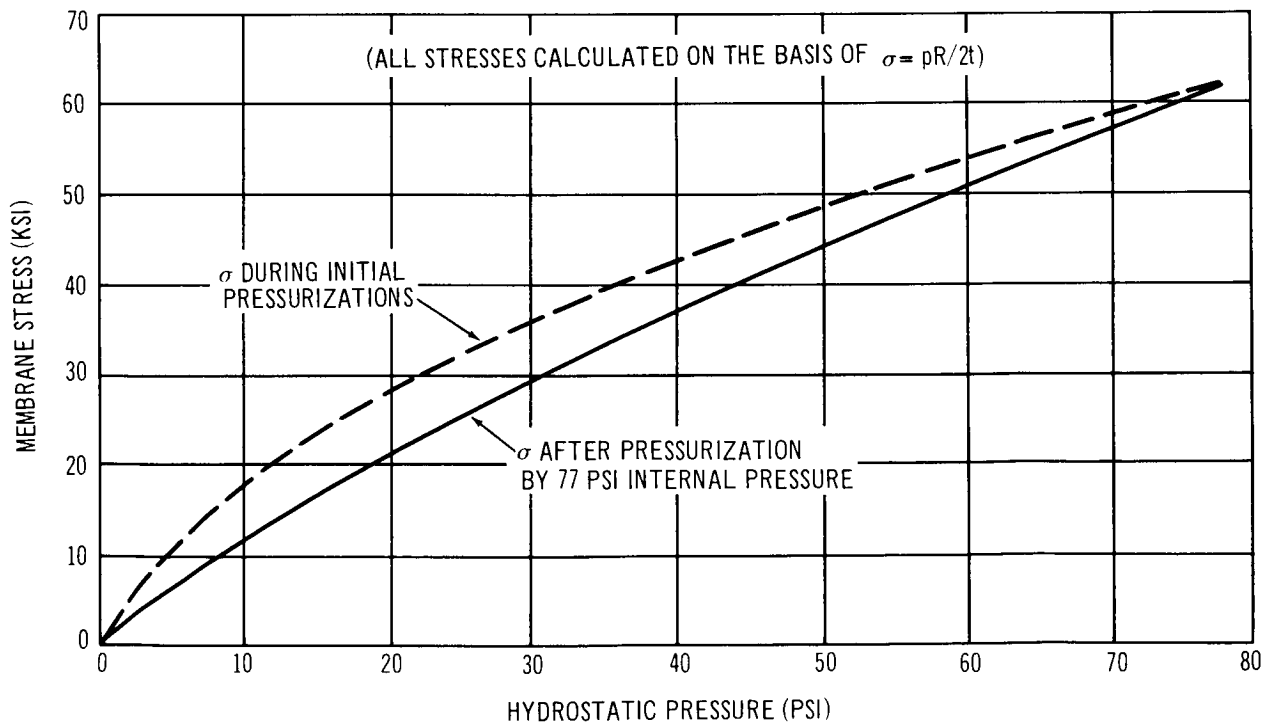


Figure 4-18. Calculated Membrane Stresses in a Biaxial Bulged Panel (0.032-Gage Aluminum Panel No. B02)

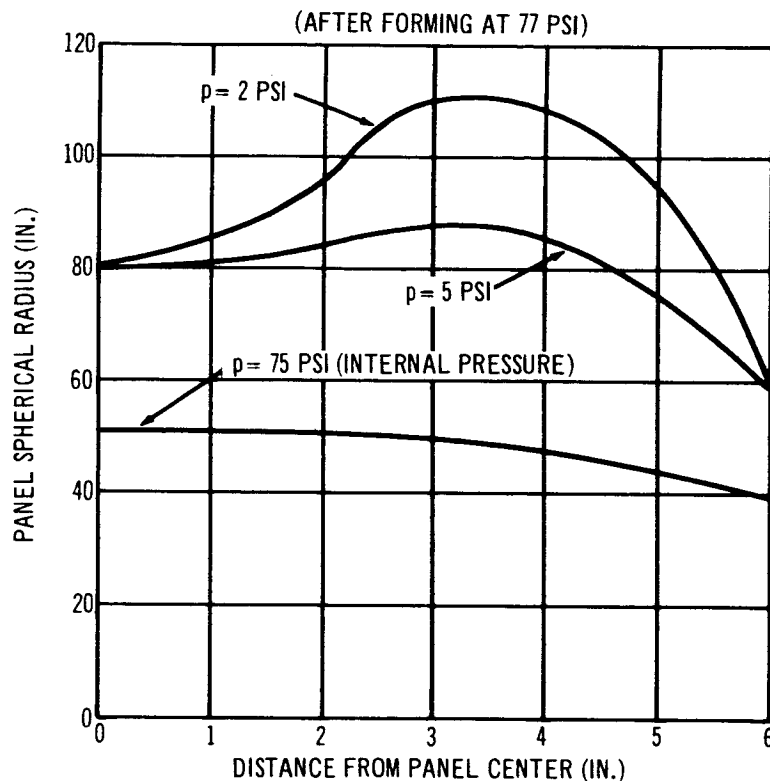


Figure 4-19. Measured Shape of Biaxial Bulged Panel(0.032-Gage Aluminum Panel No. B02)

The application of only a small amount of internal pressure, however, was sufficient to round the panel, at least over a reasonably large central area of the biaxial panels.

#### 4.3.5.1 Biaxial Panel Instrumentation

During the effort that developed techniques for fabricating the biaxial panels, it became apparent that it would be necessary to carefully measure the shape of the panel in the impact area (the center of the panel) during each experiment test run. The shape each panel took during the hydrostatic forming operation was a function of the shape of the stress strain curve in the knee region (stresses slightly less than the 0.2% offset tensile yield). Although the contours of the parts after forming fell within the allowable  $\pm 10\%$  tolerance band, the panel membrane stresses (which are dependent on the panel contour and fixture pressure) at the time of actual impact had to be determined to a

higher degree of accuracy for use during analysis of test data. It was therefore decided to install a device inside the range tank to obtain and record panel shape measurements during each test, and an instrument was designed especially for the program (Figure 4-20). This instrument is basically a spherometer with outer tripod legs located on a 4-in. -diam circle. The center leg, however, is connected to a linear differential transformer, and the biaxial panel displacement at its center relative to the tripod leg contact points was recorded as a function of fixture hydrostatic pressure on an X-Y plotter. The spherometer floated, but was lightly dead-weight loaded against the front face of the biaxial panel. It was held by a swinging lever that was in turn, mounted to a pivot lug on the biaxial test fixture. The device was retracted before each shot.

Four biaxial panels (one of each gage of each material) were instrumented, each with three strain gages. Figure 4-21 shows the geometry of the installation on each panel. The gages each had a grid length and width of 1/8-in. Standard components were used to complete the bridge power supply and data readout systems. Panel strain measurements were recorded as a function of fixture internal pressure. Calibration runs, at both ambient and at  $\text{LH}_2$  temperature, were conducted on each panel. Measured panel strains are shown in Figures 4-22 and 4-23. Also shown are calculated panel strains which are based on panel shape as measured by the spherometer instrumentation. Calculated and measured strains are in reasonable agreement.

The calculated strains include effects of both panel hoop stress loadings from the hydrostatic pressure, and bending strains produced by slight changes of panel curvature as loadings are applied. Bending strains in the thinner gage panels are practically insignificant. Calculated bending strains were as high as 15% of the total strain in the thick aluminum panel.

The total strains at  $\text{LH}_2$  temperature (from assumed zero loadings) were calculated from the panel contours which were measured during the tests of the four instrumented panels. It was not possible, however, to obtain a zero pressure reading for the strain gages after the fixture was charged with  $\text{LH}_2$ . The range was evacuated before the fixture was filled and the fixture

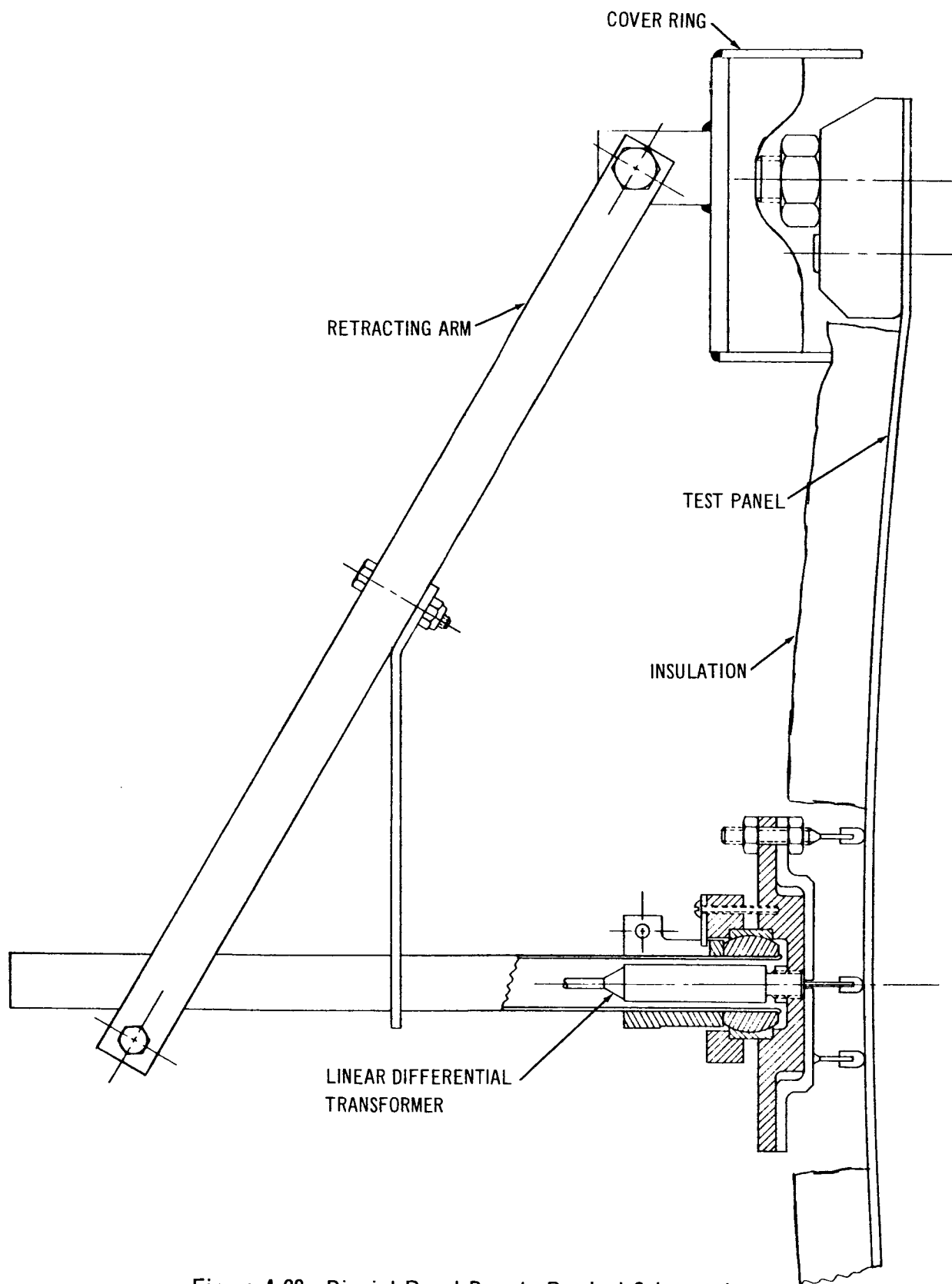


Figure 4-20. Biaxial Panel Remote Readout Spherometer

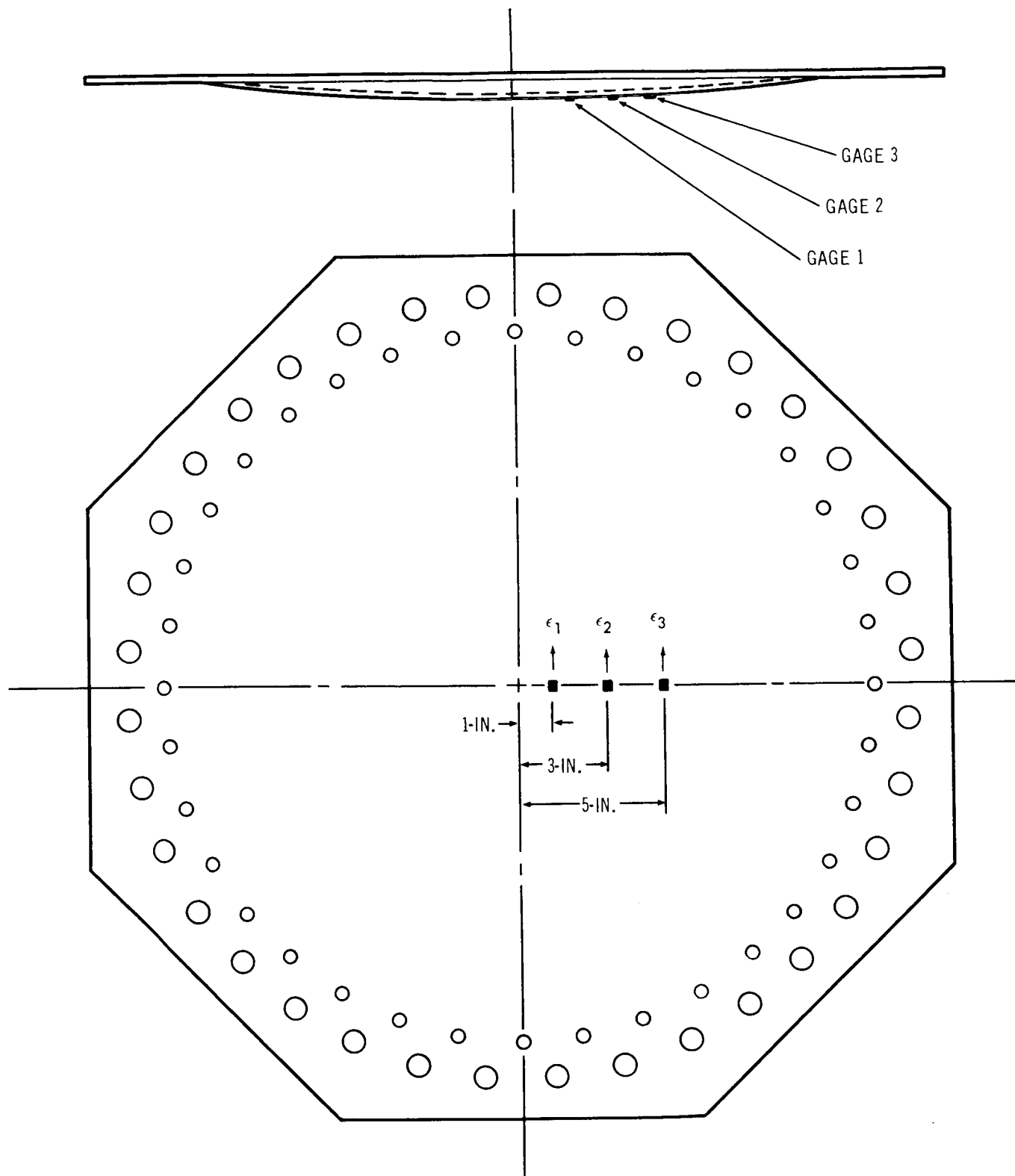
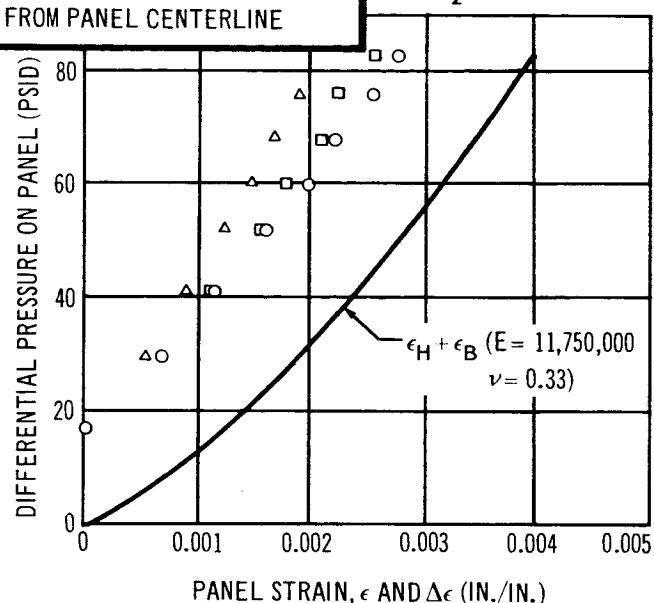
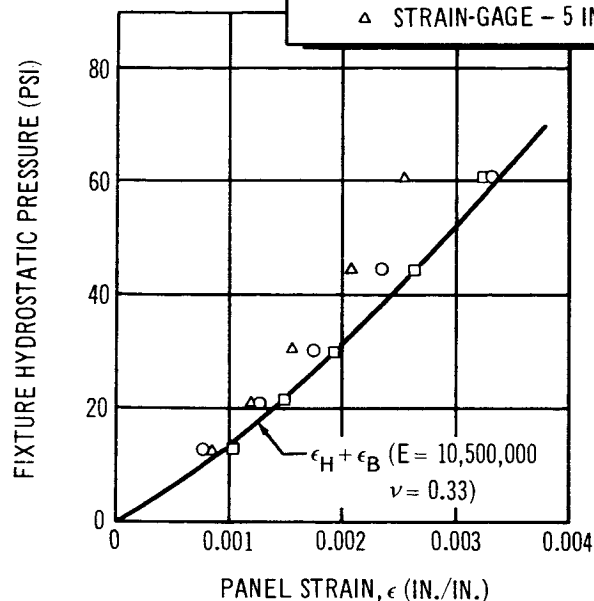


Figure 4-21. Biaxial Panel Strain-Gage Instrumentation



a. 0.032-IN.-THICK  
ALUMINUM PANEL  
AT ROOM TEMPERATURE



b. 0.125-IN.-THICK ALUMINUM PANEL  
AT ROOM TEMPERATURE

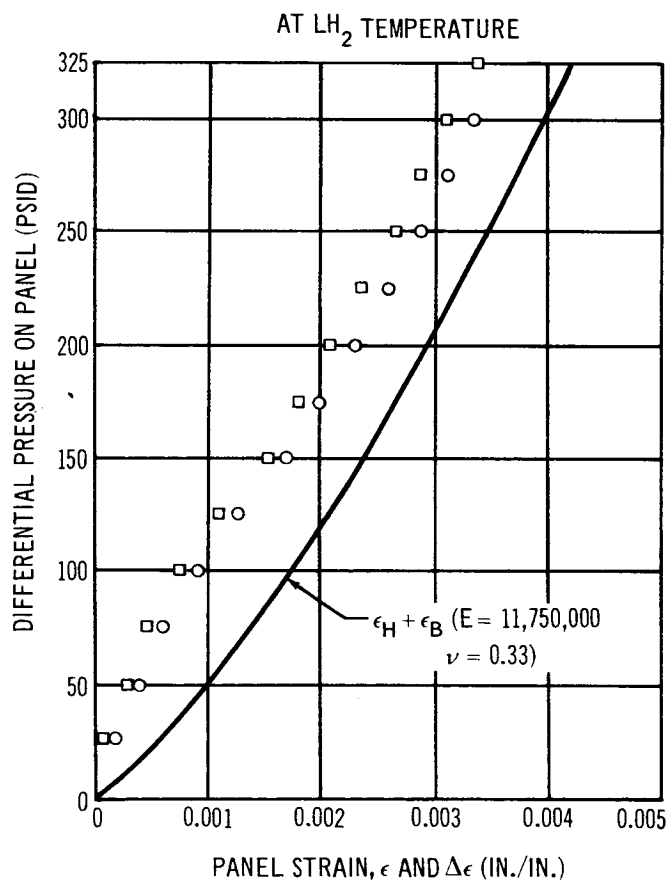
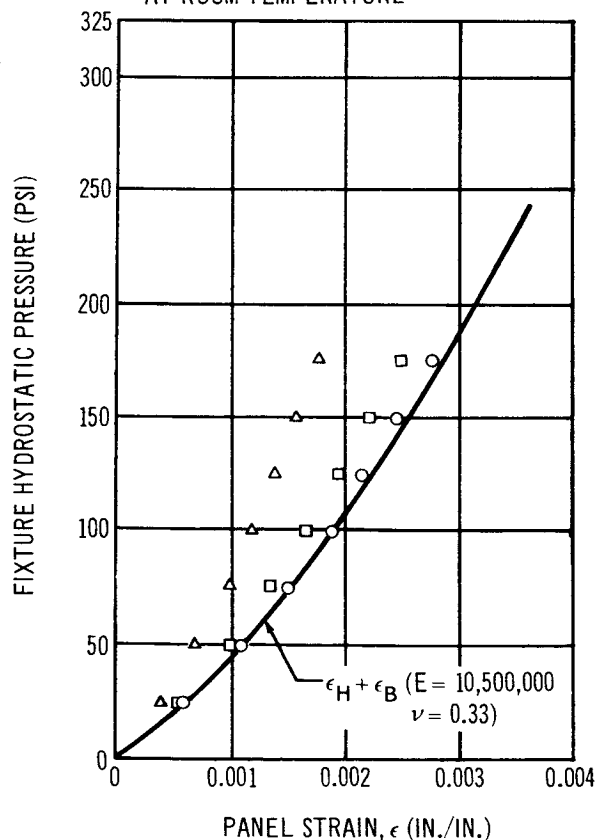
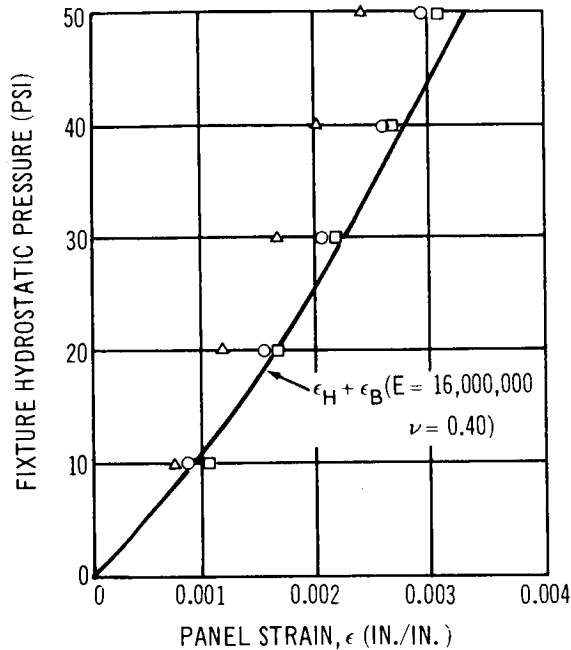


Figure 4-22. Strain-Gage Calibration of Aluminum Biaxial Panels

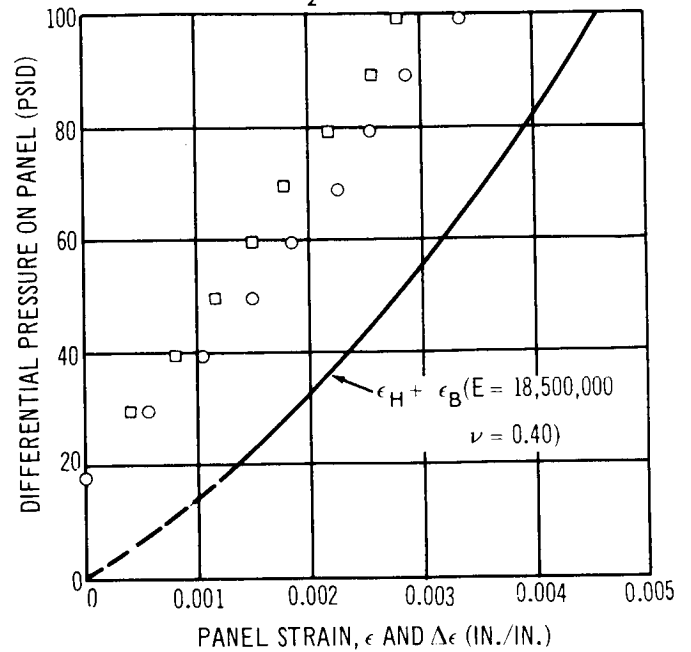
- STRAIN-GAGE - 1 IN. FROM PANEL CENTERLINE
- STRAIN-GAGE - 3 IN. FROM PANEL CENTERLINE
- △ STRAIN-GAGE - 5 IN. FROM PANEL CENTERLINE

———— CALCULATED AT PANEL CENTERLINE

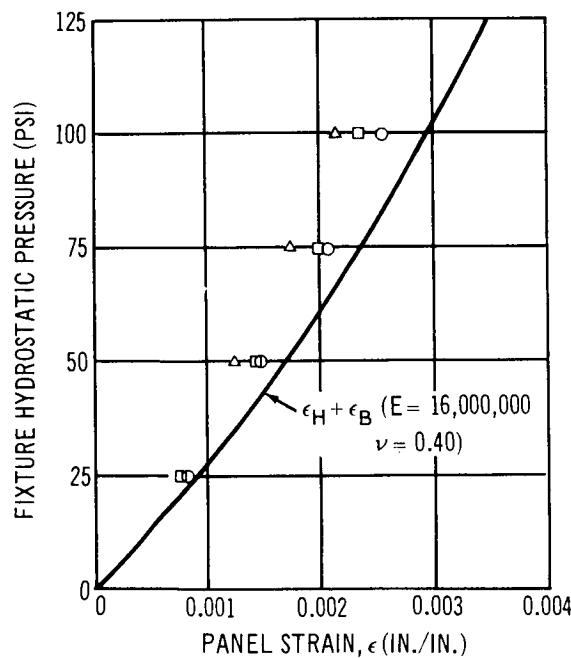
a. 0.015-IN.-THICK TITANIUM PANEL AT ROOM TEMPERATURE



AT LH<sub>2</sub> TEMPERATURE



b. 0.036-IN.-THICK TITANIUM PANEL AT ROOM TEMPERATURE



AT LH<sub>2</sub> TEMPERATURE

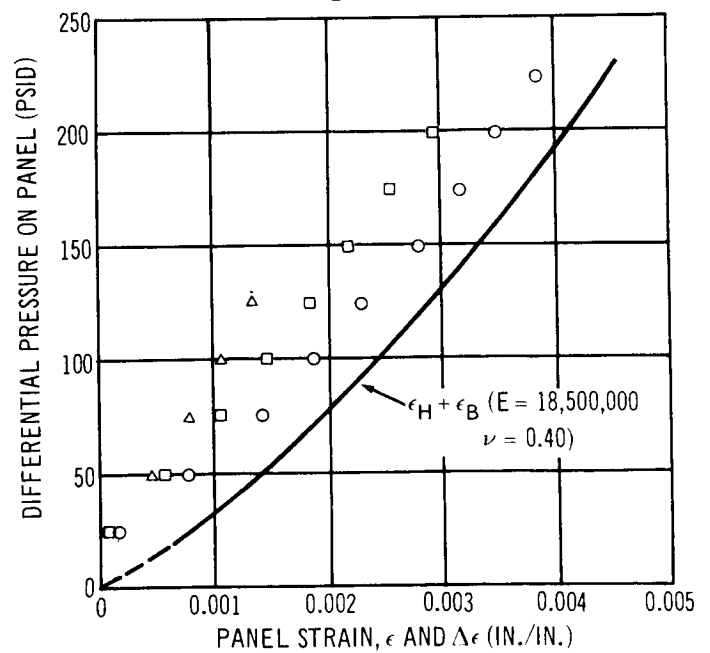


Figure 4-23. Strain-Gage Calibration of Titanium Biaxial Panels

was charged through transfer lines that vent to atmospheric pressure. Hence, there was at least one atmosphere (14.7 psi) pressure differential on the panel. The anchor points of the measured strains are at fixture-range differential pressures in the 15-20 psi range (1 atmosphere plus the head in the LH<sub>2</sub> Dewar). However, calculated and measured values agree if slopes of the curves are the same at corresponding fixture pressures. The LH<sub>2</sub> strain data are shown in this manner in Figures 4-22 and 4-23.

## Section 5

### STATIC FRACTURE TESTS OF PREFLAWED PANELS

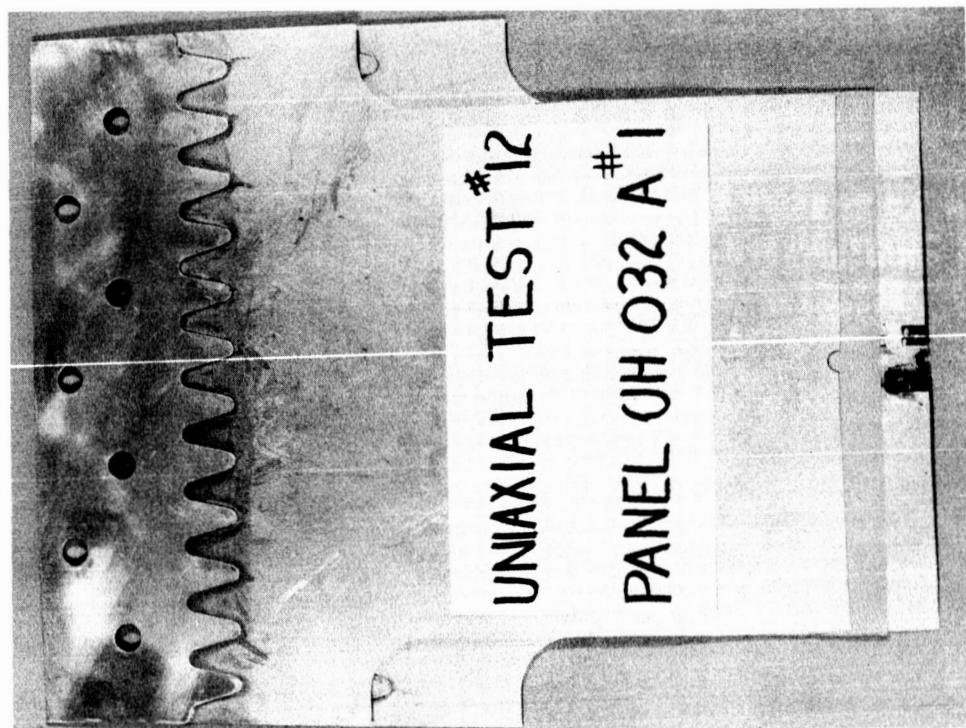
In this program an attempt was made to correlate the fracture strengths of panels preflawed and stressed by a variety of methods. Appropriate to the structures applicable to this investigation all test panels were ruptured at the temperature of liquid hydrogen. Both uniaxially and biaxially (1:1) stressed panels were investigated.

The types of preflaws were: (1) punctures produced by particles on hypervelocity impact and (2) cracks produced by cyclically stressing the panels. All flaws in the panels were centrally located. The fatigue-cracked panels were included for testing since the fatigue crack is known to be the severest type flaw that can be produced. In some cases a flaw by hypervelocity impact may be equivalent to a fatigue crack; in other cases it is not.

The fracture strength and fracture toughness of the two materials under various test conditions were determined. Results of uniaxial tests were compared with known fracture mechanics equations: correlation of the experimental data with the fracture equations was good for both fatigue and impact type preflawed panels. Good agreement is also shown between the experiment results and the predicted behavior under biaxial straining. The biaxially strained characteristics are predicted from uniaxial data of various flaw types. The fracture toughness characteristics of materials determined in this manner have been found useful in correlating the hypervelocity impact point-load tests.

#### 5.1 UNIAXIAL PANEL FRACTURE TESTS

The experiment results of the uniaxial stressed panels are analyzed in this section. Twenty panels were tested and Figure 5-1 shows typical test results. The test data are plotted in all the figures of Section 5 as the gross area



A. IMPACT PREFLOWED ALUMINUM PANEL



B. IMPACT PREFLOWED TITANIUM PANEL

Figure 5-1. Typical Results of Uniaxial Static Fracture Tests

tensile stress at fracture as a function of both the initial flaw length or crack size (in inches) as well as the critical flaw size. In some cases separate graphs are presented for the two types of flaws. The curves on the figures are represented by mathematical formulae and are constructed to closely match the experiment data. The equations and parameters used in the fracture mechanics formulae are discussed below.

#### 5.1.1 Analysis Methods

In the field of fracture mechanics, theoretical and semi-empirical equations have been developed to predict fracture strength of flawed structure under both uniaxial and biaxial conditions. However, the reliability of the methods needs to be continually substantiated. This is mainly due to the newer design and environmental conditions requiring investigation.

The two predominant experimental parameters necessary to check the validity of the analytic formulae are: (1) the type and size of flaw or crack at instability and (2) the level of stress in a structure at the onset of fracture.

It should be recognized that under the complex testing conditions of this program, the critical size of flaw or crack that is formed at the instant of rupture is not always easily measured. An accurate determination of the flaw size preceding instability is required if normal fracture mechanics equations are to be used. The method for determining the size of such cracks is discussed in the section on test procedure.

The method employs bonded continuity gages to measure the propagation of fracture. As fracture progresses across the panels the small wires or strands of the gage are correspondingly fractured. There is some evidence that the continuity gage strands tend to break ahead of a slowly propagating crack, particularly when the gages are installed on titanium and when the tests are conducted at cryogenic temperature. Therefore, analysis based on the continuity gage data readout probably results in an overestimation of the critical flaw sizes,  $2a$  and  $l_c$ . To obtain the possible spread of uncertainty for  $K_c$  and  $R_p$ , a fit was made to the initial flaw sizes  $2a$  and  $l_o$ .

For design purposes, the value of the initial flaw size should be used if the critical length at instability is not accurately known. W.S. Pierce (Reference 9) states that in practice the original crack size is a practical parameter to use in calculating acceptable stress levels for a structure with a known flaw.

The calculated stresses and measured flaw lengths were then introduced into the following equations:

### 1. Irwin Method.

Irwin (Reference 10) has developed a theoretical analysis to define the fracture toughness,  $K_C$ , of finite-width panels under uniaxial tensile loading and containing central flaws or cracks. His formula is as follows:

$$K_C = \sigma \left[ w \tan \left\{ \frac{\pi}{w} \left( a + \frac{K_C^2}{2\pi\sigma_y^2} \right) \right\} \right]^{1/2} \quad (5-1)$$

where

$\sigma$  = gross section stress at fracture

$w$  = panel width

$a$  = 1/2 the crack length in inches at fracture (central crack)

$\sigma_y$  = uniaxial yield strength

$\frac{K_C^2}{2\pi\sigma_y^2}$  = uniaxial plastic zone size correction at crack tip

### 2. Christensen-Denke Method.

A semiempirical method developed at Douglas (Reference 11) is based on physical observations and relies on experiment results to define a single, initially unknown parameter.

It has been demonstrated (References 11 and 13) that the method will predict behavior and strength of flawed structure (through cracks in thin sheets, that is, essentially plane stress conditions) for a wide range of panel widths and for both uniaxial and biaxial strain conditions. The equation is represented in the form:

$$\sigma_{\text{fracture}} = \frac{\sigma_u \left[ 1 - \frac{l_c}{w} \right]}{\sqrt{1 + \frac{3 l_c}{R_p w}}} \quad (5-2)$$

where

- $\sigma_u$  = either uniaxial or multiaxial strain tensile strength
- $R_p$  = notch resistance factor (empirical)
- $l_c$  = total central crack length at instability
- $w$  = panel width

The above methods have both advantages and disadvantages. It was proposed that both approaches be considered in evaluating the experimental results generated in this program. Therefore, experimental data are compared with the predicted behavior of the panels defined by each of the methods.

#### 5.1.2 Correlation of Results with the Irwin Method

Test results of the center-fatigue-cracked and impact-flawed panels in the titanium and aluminum alloys are shown in Figures 5-2, 5-3, and 5-4. In the titanium alloy, slight differences in fracture strengths can be noted between the 0.015- and 0.036-in.-thick panels. Also noted is the lower fracture strengths of the fatigue-cracked titanium panels as compared with the titanium panels containing impact flaws.

Figure 5-4 presents both impact and fatigue preflawed panel data for the aluminum alloy. No difference in fracture strength of statistical significance can be noted for these panels in relation to panel thickness or type of flaw. The fracture strengths of fatigue-cracked aluminum panels appear to be slightly lower than that of impact preflawed panels.

A summary of average fracture toughness values of the materials investigated is given in Table 5-I. A complete tabulation of all uniaxial static fracture test data is given in Appendix C. The value of the stress intensity factor,  $K$ , corresponding to initial flaw size is also given in Appendix C.



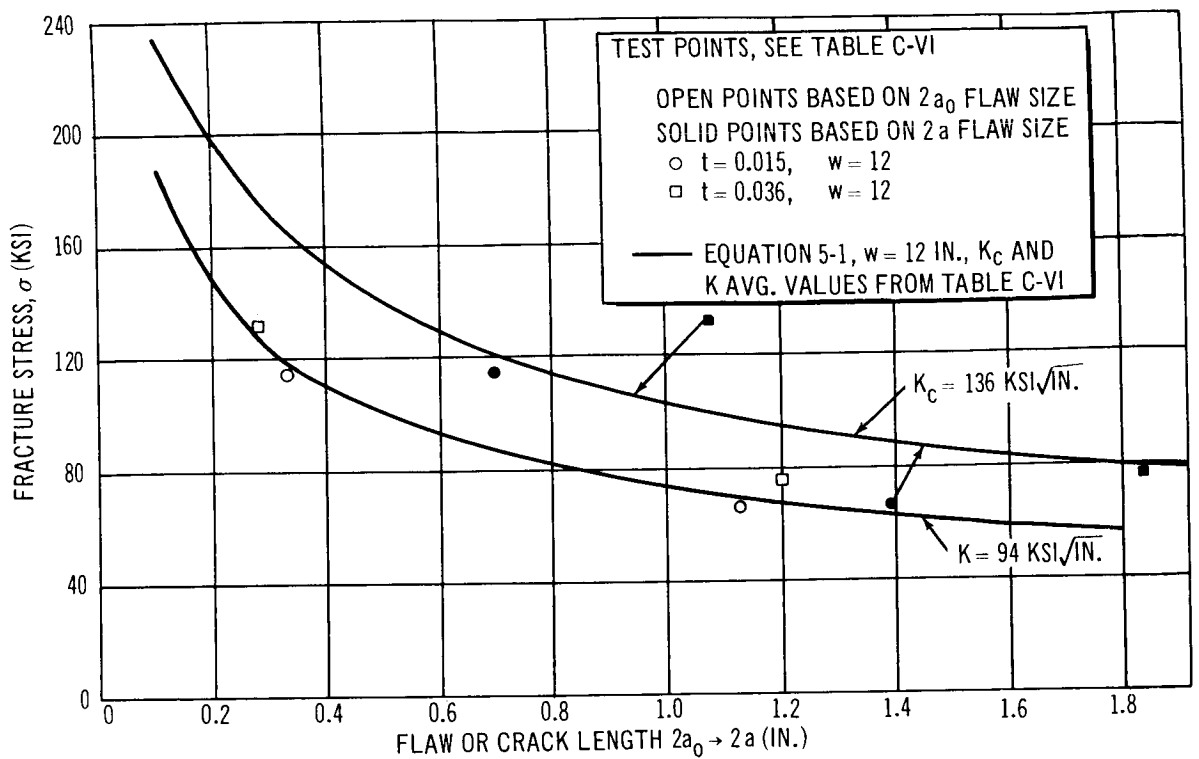


Figure 5-2. Uniaxial Fracture Tests of Center Fatigue-Cracked Panels  
(5Al-2.5 Sn (ELI) Titanium Test Temperature  $-423^\circ\text{F}$ )

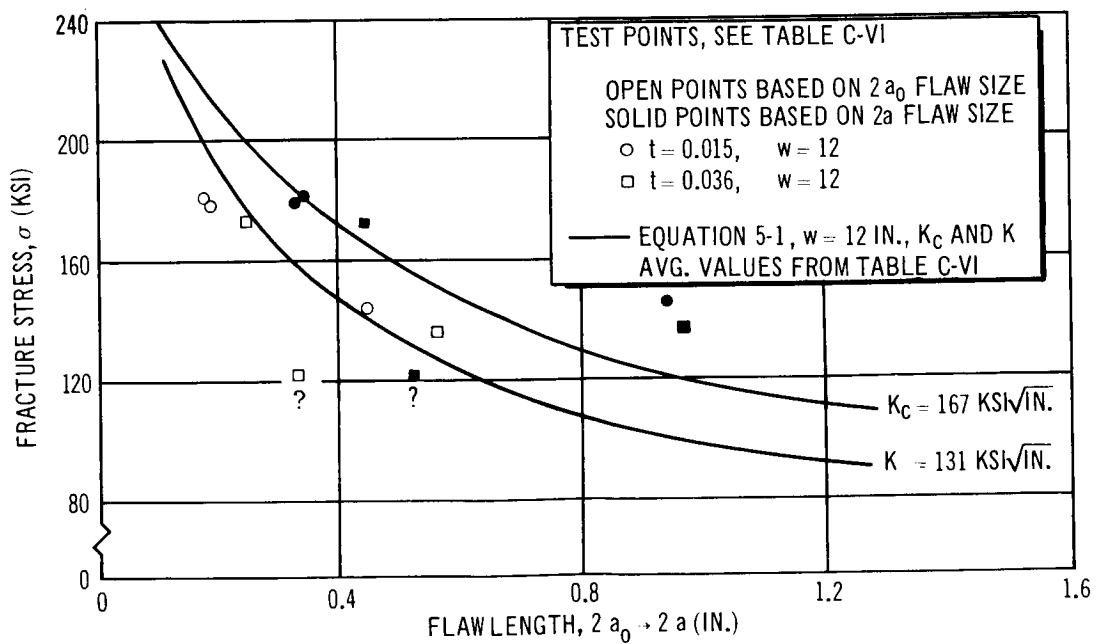


Figure 5-3. Uniaxial Fracture Tests of Impact-Flawed Panels  
(5Al-2.5 Sn (ELI) Titanium Test Temperature,  $-423^\circ\text{F}$ )

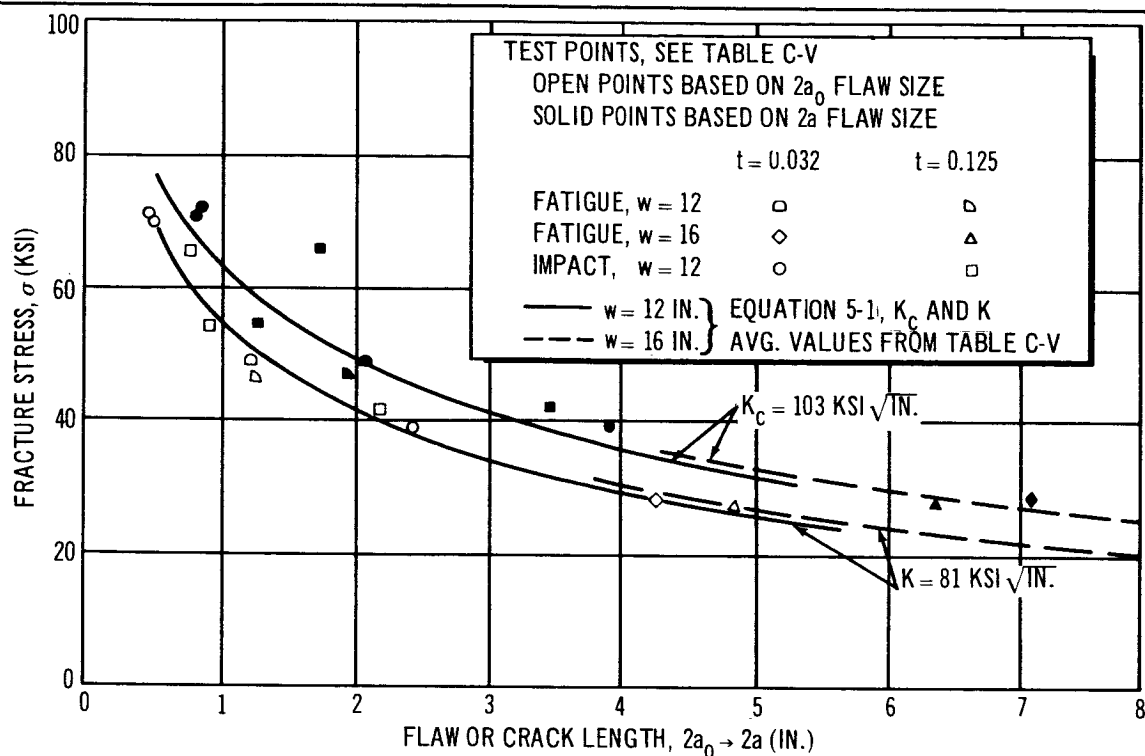


Figure 5-4. Uniaxial Fracture Tests of Center Preflawned Panels  
 (2219-T87 Aluminum Test Temperature,  $-423^\circ\text{F}$ )

Table 5-I  
 FRACTURE TOUGHNESS AT  $-423^\circ\text{F}$

Material	Flaw Type	$K_c$ , (KSI $\sqrt{\text{in.}}$ )*
5Al-2.5Sn titanium (ELI)	Impact (hypervelocity penetration)	167
5Al-2.5Sn titanium (ELI)	Center-fatigue crack	136
2219-T87 aluminum	Impact (hypervelocity penetration)	107
2219-T87 aluminum	Center-fatigue crack	97

\*Values are average values for both thicknesses (thin and thick gage) of each material. See Tables C-V and C-VI for complete tabulation.

### 5.1.3 Correlation of Results with the Christensen-Denke Method

Similar to the Irwin equation, the Christensen-Denke formula can be used to accurately represent the fracture strength envelope for flawed and ruptured panels. Figures 5-5, 5-6, and 5-7 show the fit of the equation (represented by the curve) to the experiment results.

Both fracture mechanics equations used in this program can be modified for the condition of biaxial loading. The modification of the equations and their fit to experimental pressure vessel data is discussed next.

## 5.2 BIAXIAL PANEL FRACTURE TESTS

The experimental results of the biaxially stressed panels are shown in a form similar to that used for the uniaxial panel work. Preflaws were produced by hypervelocity impact and by fatigue cracking. A total of 13 biaxial panels were tested.

### 5.2.1 Analysis Methods

The analytic equations used in treating the biaxially stressed panels are basically the same as those presented above. Irwin's equation can be used for biaxial conditions with slight modifications to correct for sheet bulging (bending) at the flaw tip and radius of curvature effects. R. B. Anderson (Reference 12) has derived a simple expression to account for these effects in Irwin's uniaxial loading equation. The resultant equation which has been used to predict fracture behavior of the flawed pressure vessel panels of this program is given below. Although this equation has been developed for cylinders (2:1 stress ratio), it is used here with no further modifications for a biaxial 1:1 stress ratio.

#### 1. Irwin-Anderson Equation.

$$\sigma_H \text{ or } \sigma_{Hc} = \frac{K_{cn}}{\sqrt{\pi a + \frac{1}{2} \frac{K_{cn}^2}{\sigma_{yB}^2} (1 + C \frac{a}{R})}} \quad (5-3)$$

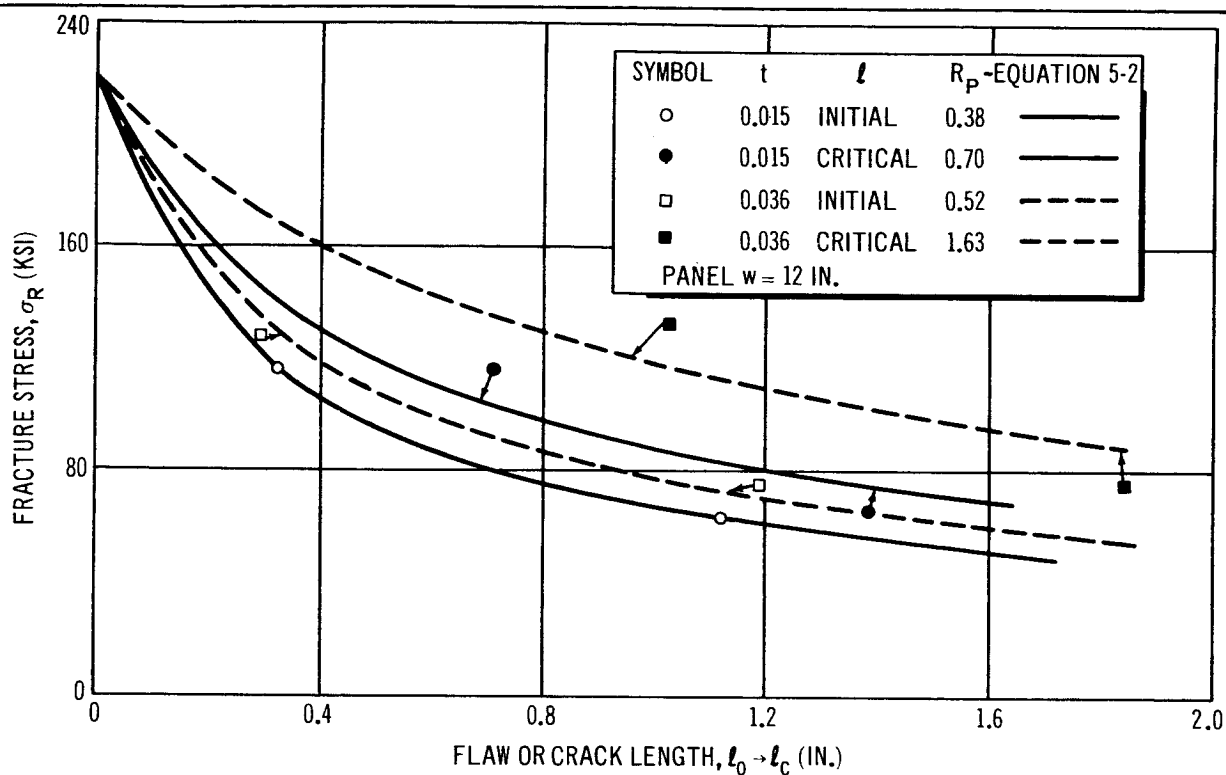


Figure 5-5. Uniaxial Fracture Tests of Center Fatigue-Cracked Panels (5AL-2.5 Sn (ELI) Titanium Test Temperature,  $-423^{\circ}\text{F}$ )

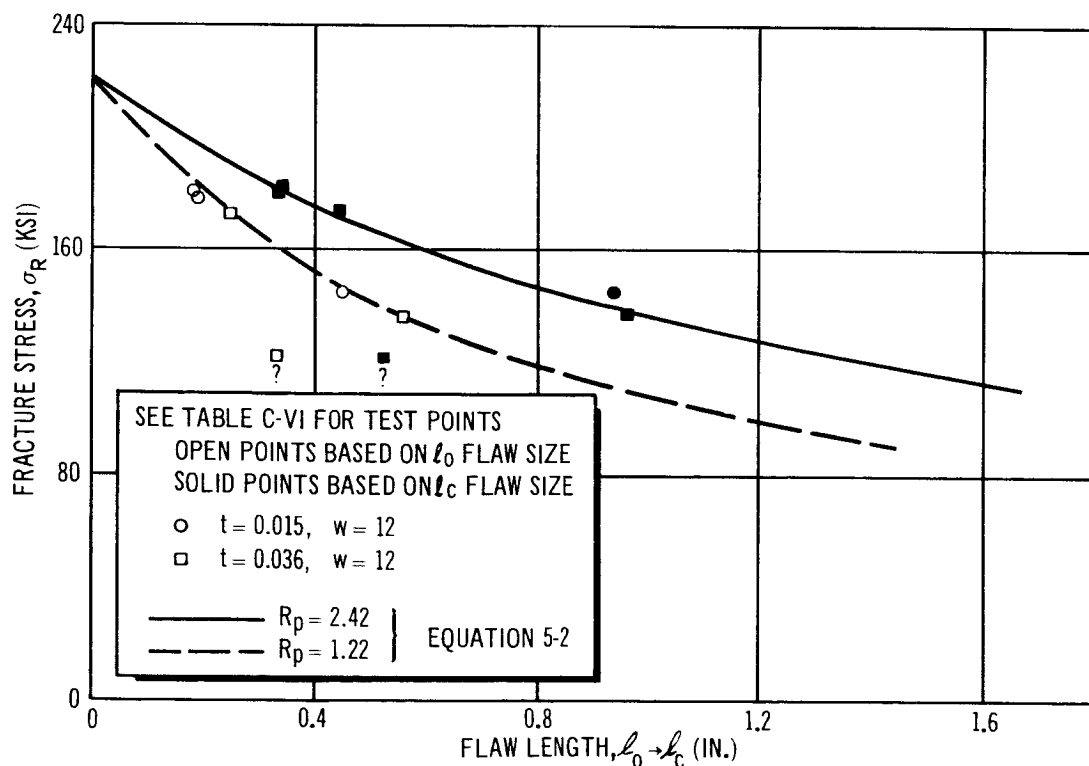


Figure 5-6. Uniaxial Fracture Tests of Center Impact-Flawed Panels (5AL-2.5 Sn (ELI) Titanium Test Temperature,  $-423^{\circ}\text{F}$ )

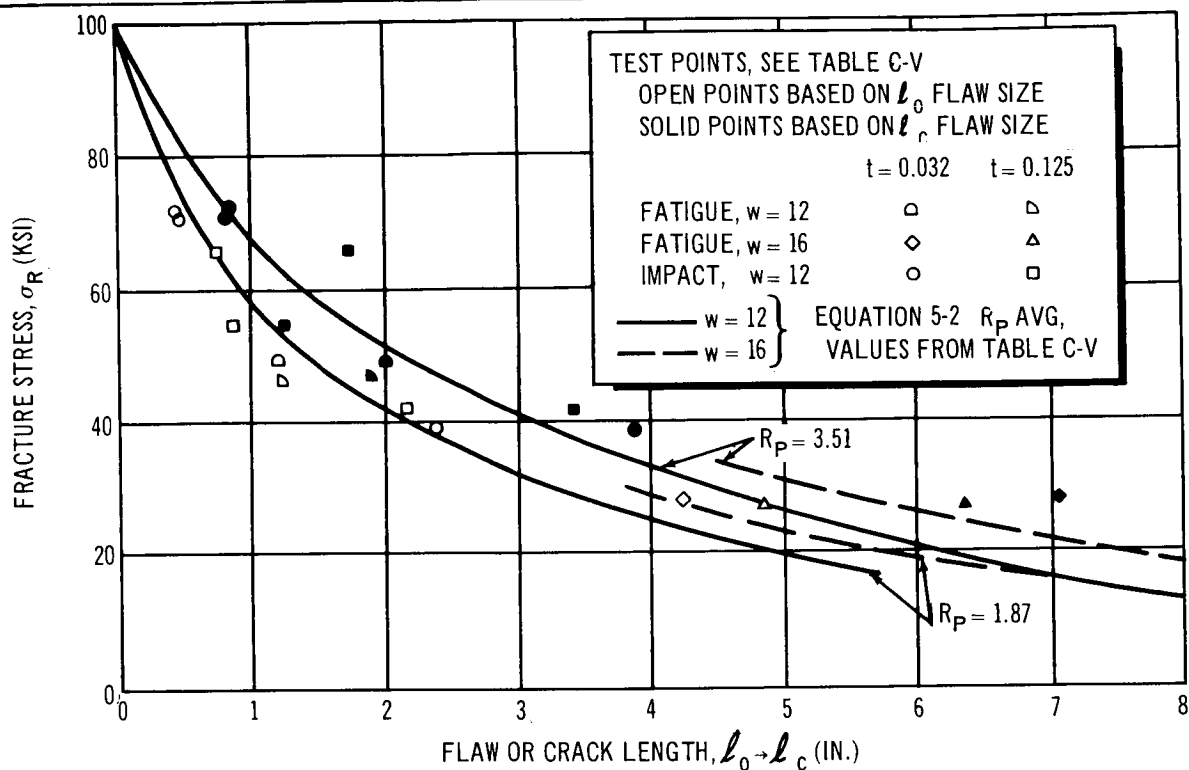


Figure 5-7. Uniaxial Fracture Tests of Center Preflawned Panels (2219-T87 Aluminum Test Temperature  $-423^\circ\text{F}$ )

where

- $K_{cn}$  = nominal fracture toughness (uniaxial) based on critical flaw size  
 $a$  =  $1/2$  critical crack length  
 $\sigma_{yB}$  = biaxial yield strength  
 $\sigma_H$  = membrane or hoop stress at rupture  
 $C$  = bulge coefficient  
 $R$  = radius of pressure vessel

## 2. Christensen-Denke Equation.

It has been observed that the Christensen-Denke equation for uniaxial loading also can be used to accurately represent the fracture envelope for structures subjected to multiaxial loading. In Reference 13, the fracture strength of cylinders 5 to 260 in. in diam predicted by the following equation are compared with experimental results.

$$\sigma_H = \frac{\sigma_u \left(1 - \frac{l_c}{w}\right) \sqrt{1 + 3l_c/R}}{(1 + 4.6 \frac{l_c}{R})} \quad (5-4)$$

where

$(1 + 4.6 \frac{l_c}{R})$  = an empirical correction (Reference 14) developed by Kuhn to account for the effects of biaxiality and remaining symbols are as defined for Equation 5-2.

### 5.2.2 Correlation of Results with the Irwin-Anderson Method

The experiment results of the fatigue preflawed and impact flawed panels ruptured under biaxial loading are shown in Figures 5-8, 5-9 and 5-10. Fracture toughness values,  $K_{cn}$ , of 97 KSI  $\sqrt{\text{in.}}$  for all aluminum, 136 KSI  $\sqrt{\text{in.}}$  for the fatigue-cracked titanium, and 167 KSI  $\sqrt{\text{in.}}$  for the impact-damaged titanium panels were used in the calculations. These values were obtained directly from the uniaxial test results.

The good agreement between the experimental and predicted behavior is shown in the figures. The values of the parameter (C) in the Irwin-Anderson equation were taken from Anderson's work, Reference 12.

### 5.2.3 Correlation of Results with the Christensen-Denke Method

An additional correlation of the experimental results is shown in Figures 5-11, 5-12, and 5-13. In all cases the parameters and equations defined by the uniaxial tests are modified for biaxial loading with Kuhn's correction factor.

The fit of the equation to the results of the fatigue-flawed and impact-flawed panels appears equivalent (based on a limited number of tests) to the Irwin-Anderson equation.

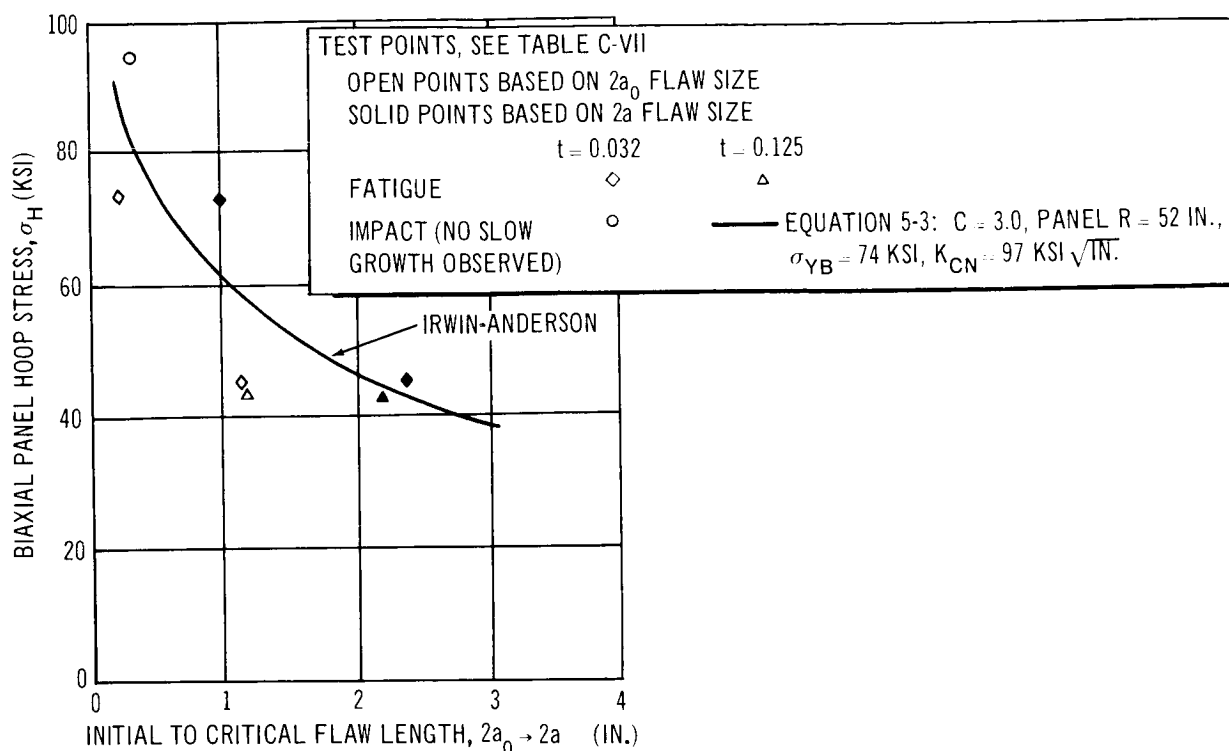


Figure 5-8. Burst Tests of Preflawn Biaxial Panels (2219-T87 Aluminum Test Temperature,  $-423^\circ\text{F}$ )

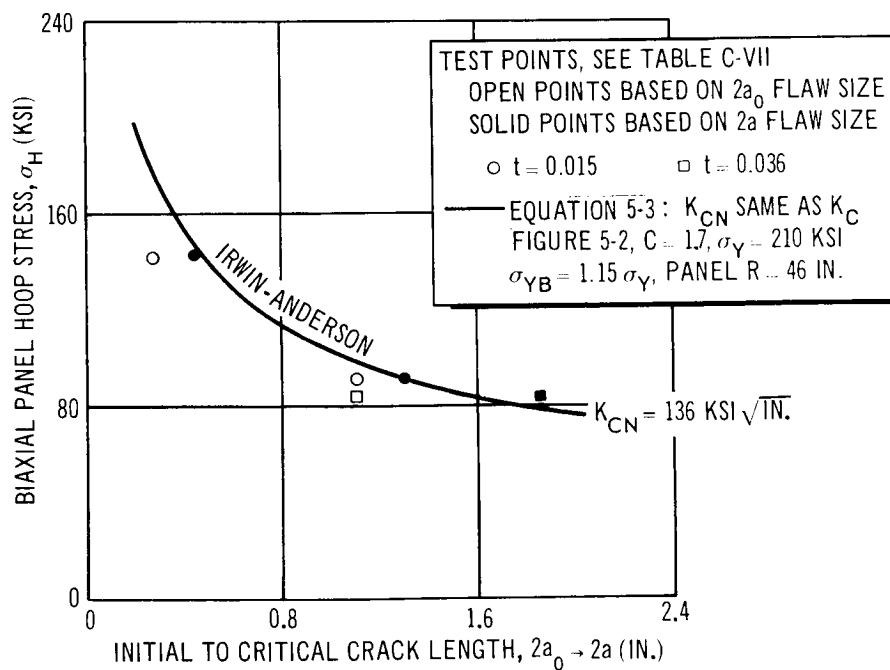


Figure 5-9. Burst Tests of Fatigue-Cracked Biaxial Panels  
 (5Al-2.5 Sn (ELI) Titanium Test Temperature,  $-423^\circ\text{F}$ )

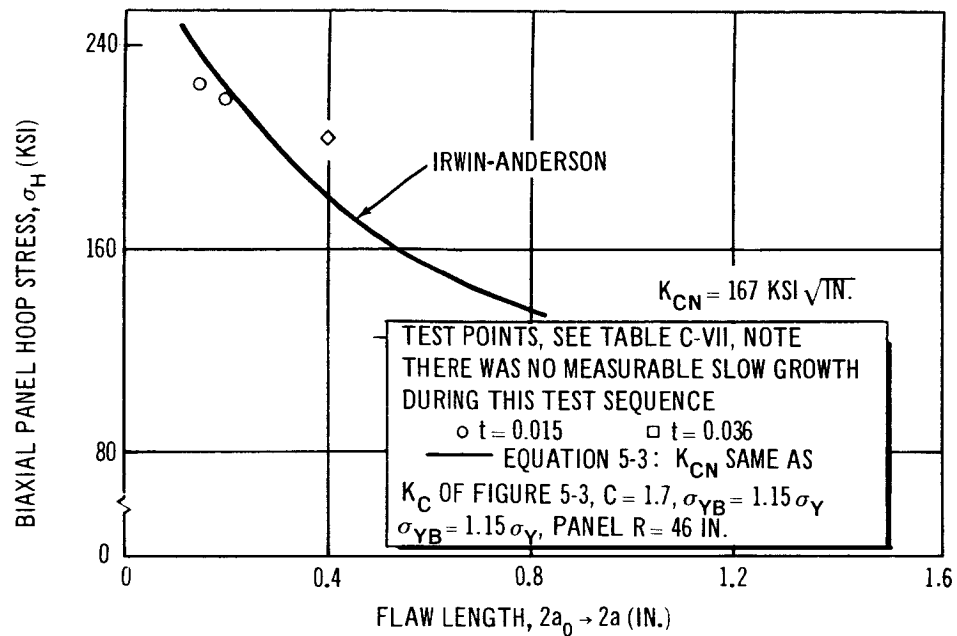


Figure 5-10. Burst Tests of Impact Preflawn Biaxial Panels (5Al-2.5 Sn (ELI) Titanium  
Test Temperature  $-423^\circ\text{F}$

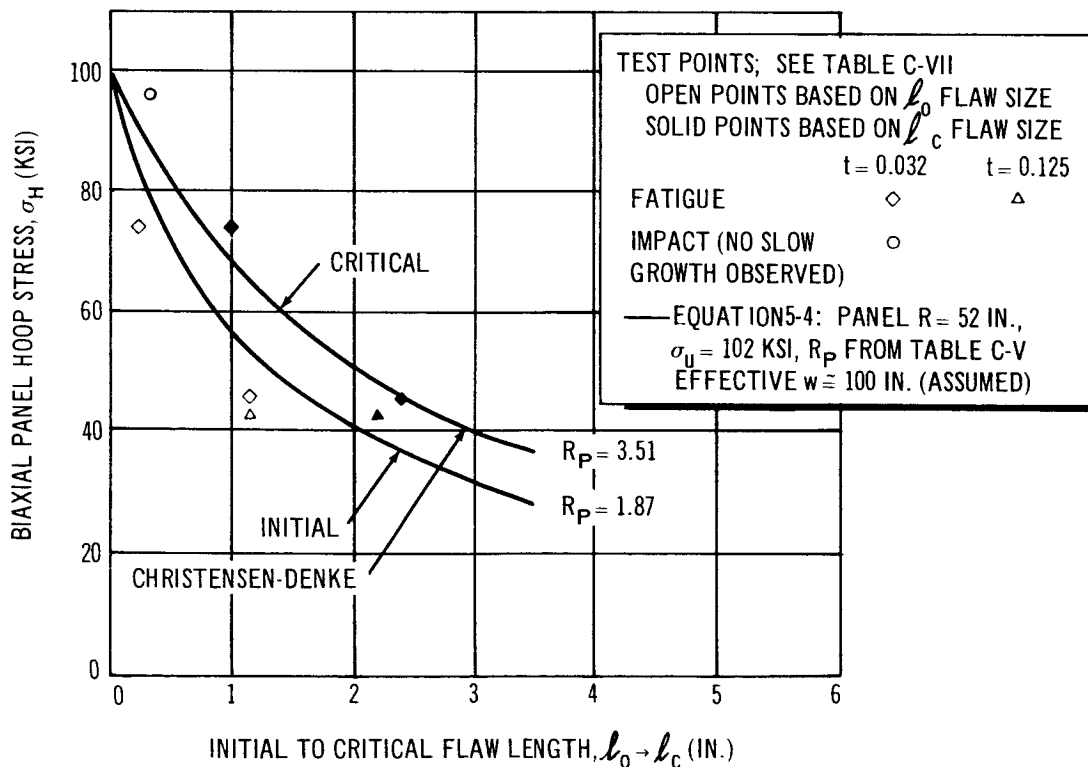


Figure 5-11. Burst Tests of Preflawn Biaxial Panels (2219-T87 Aluminum Test Temperature  $-423^\circ\text{F}$ )



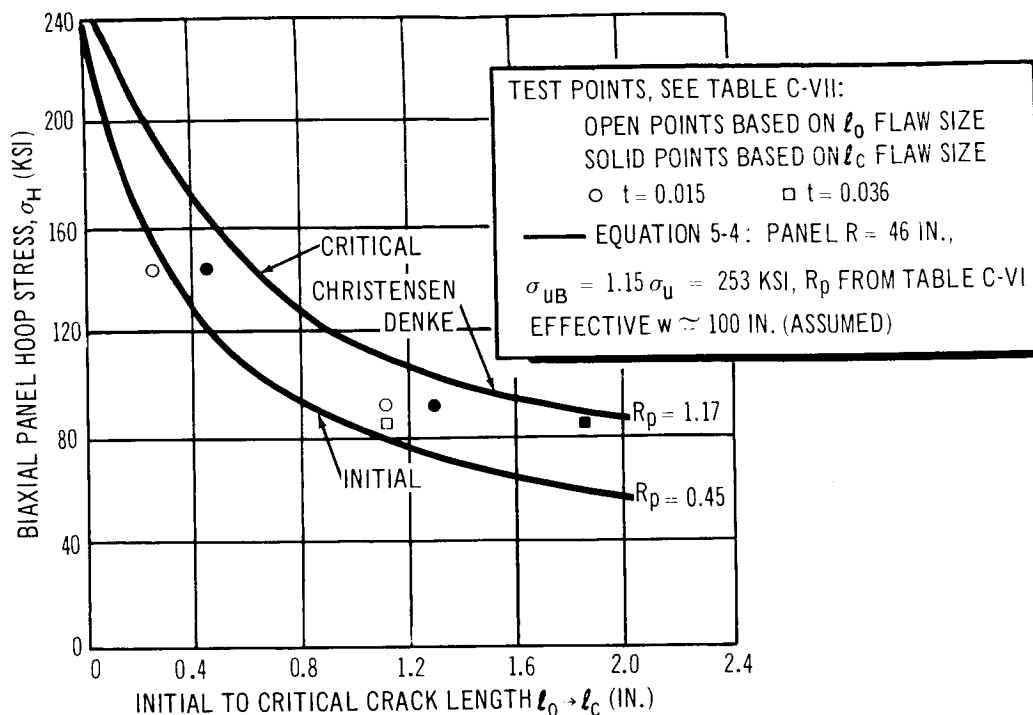


Figure 5-12. Burst Tests of Fatigue-Cracked Biaxial Panels (5Al-2.5 Sn Titanium (ELI) Test Temperature  $-423^{\circ}\text{F}$ )

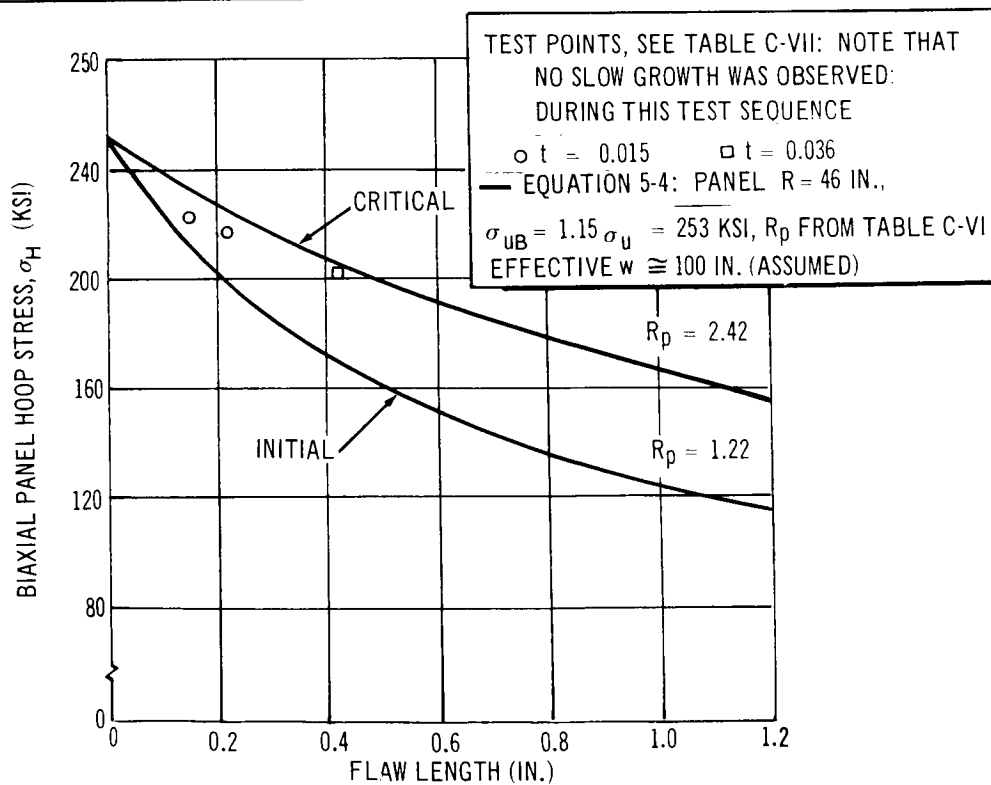


Figure 5-13. Burst Tests of Impact Preflawn Biaxial Panels (5Al-2.5 Sn (ELI) Titanium Test Temperature  $-423^{\circ}\text{F}$ )

## Section 6

### HYPERVELOCITY IMPACT POINT-LOAD TESTS

After completion of installation of the LH<sub>2</sub> system in the ballistic range, system checkout tests were conducted, and some preliminary LN<sub>2</sub> checkout shots were made. The LN<sub>2</sub> shots were all point-load tests, that is, the projectiles were launched against unprotected, biaxially stressed panels. This section presents detail results of all hypervelocity impact point-load tests. A series of LH<sub>2</sub> tests followed the initial LN<sub>2</sub> checkout work and comprised the major portion of the point-load test phase.

The initial sequence of impact shots into LH<sub>2</sub>-pressurized panels was conducted using essentially the same procedure as that used during the LN<sub>2</sub> checkout work. These LH<sub>2</sub> tests produced the following unexpected results: (1) panel damage was quite severe, (2) the region adjacent to the puncture in each panel was deformed inward, (3) there were numerous radial cracks between the fast running tears, and (4) the tips of the sheet at the edges of the puncture were severely curled inward. This behavior of a LH<sub>2</sub>-pressurized shell was first thought to be anomalous to the behavior observed during hypervelocity impact tests of tank shells filled with other fluids. However, additional work disclosed that a heavy layer of condensation (henceforth referred to as ice) had formed on the panels during each LH<sub>2</sub> fill. Interaction of the impacting projectile with the layer produced the strange panel-fracture behavior effects that were observed during the early LH<sub>2</sub> tests. These effects are discussed in detail in Section 6.2 of this report. Panels with a layer of ice frozen on the front surface are representative of certain composite structural configurations; these panels are now defined as quasi-composite. Thus, data from point-load tests of LH<sub>2</sub>-pressurized panels are of two distinct types: quasi-composite panel data and ice-free, or unprotected, panel data.

No condensation of consequence had formed on the panels during the LN<sub>2</sub> checkout tests.

## 6.1 LIQUID NITROGEN CHECKOUT TESTS

Liquid nitrogen and gaseous helium were used as the system pressurizing media during the checkout tests. Three LN<sub>2</sub> shots were made; the first two impacts were made into 0.032-in. -thick aluminum panels. A 1/8-in. -diam glass projectile impact produced a catastrophic fracture, while a 1/16-in. -diam glass projectile impact simply punched a hole in the panel (membrane stress was approximately 40 KSI for both tests). After these tests were conducted, a decision was made to use metal projectiles to provide results more directly comparable with preceding NASA-sponsored research (Reference 15). Some bumper shots later in the current program were made with Lexan projectiles. The third liquid nitrogen shot was made into a 0.036-in. -thick, titanium-panel target, using a 3/32-in. -diam aluminum projectile. This test produced a simple puncture in the titanium panel.

Impact velocities were in the 22,000 fps range. The impact flaws were as expected as results from hypervelocity impact into a pressurized, liquid-filled shell. The entrance holes were typical hypervelocity punctures, and the fluid shock pressures caused outward bulging of the shells in the region adjacent to the punctures.

Basic results of the point-load tests into LN<sub>2</sub>-pressurized panels are shown in Figure 6-1 for 0.032-in. -thick, 2219-T87 aluminum alloy, and in Figure 6-2 for 0.036-in. -thick, 5Al-2.5Sn (ELI) titanium alloy. The plotted points show hypervelocity-puncture flaw size and the panel membrane stress for each test and give a rough indication of the hypervelocity-impact fracture envelope for LN<sub>2</sub> filled shells. It is evident that the hypervelocity-impact fracture-strength characteristics (dynamic) are significantly different than the static fracture-strength characteristics of fatigue preflawed biaxial panels.

The fatigue-fracture curves were calculated by Anderson's method (Reference 12) using uniaxial, fracture-strength, baseline data which was obtained from tests on specimens made from the same alloys at LN<sub>2</sub> temperature.

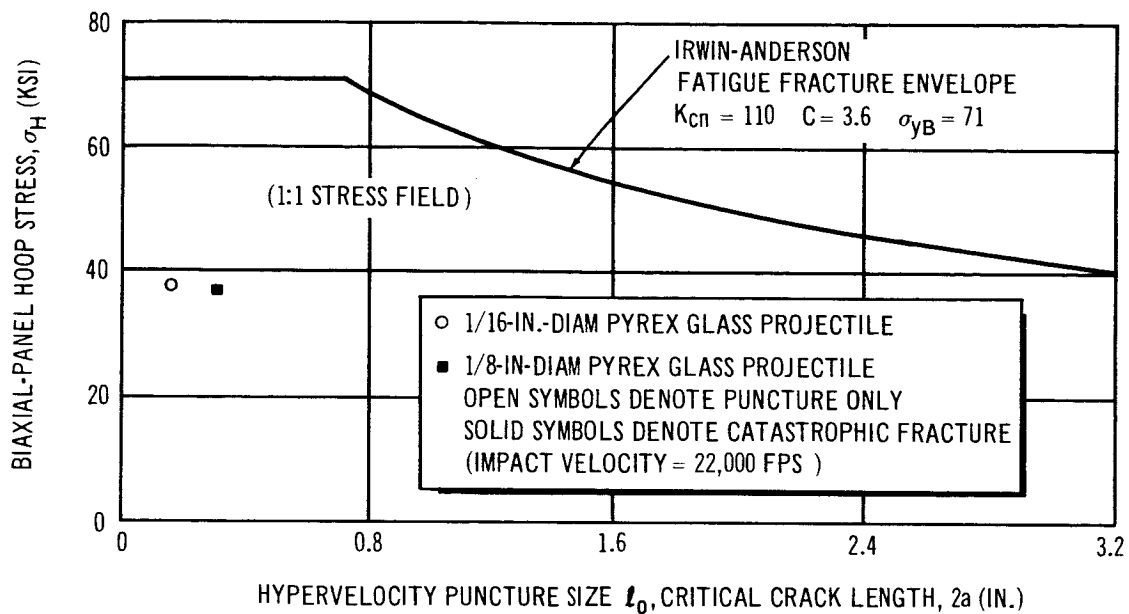


Figure 6-1. Hypervelocity Impact Tests of Stressed Biaxial Panels – Aluminum (Behavior of 0.032-In.-Thick 2219-T87 Aluminum at  $LN_2$  Temperature)

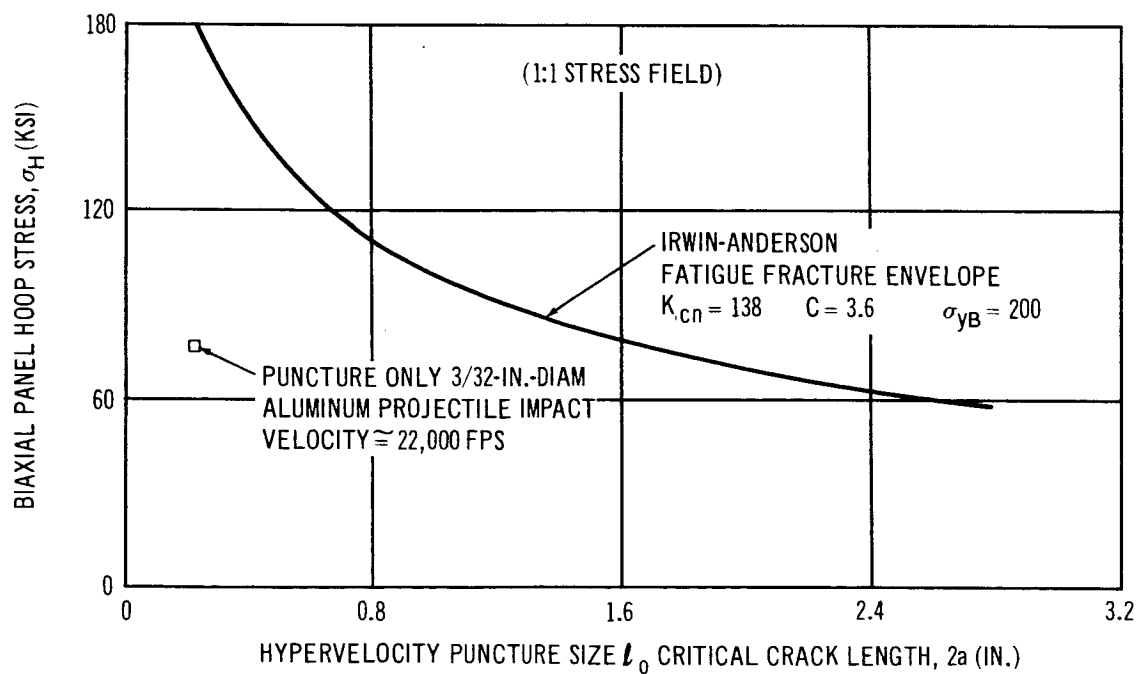


Figure 6-2. Hypervelocity Impact Tests of Stressed Biaxial Panels – Titanium (Behavior of 0.036-In.-Thick 5Al-2.5 Sn (ELI) Titanium at  $LN_2$  Temperature)

Later work on fracture-strength data correlation of  $\text{LH}_2$ -filled panels resulted in development of a general expression describing the behavior of cryogenic tank shells when subjected to point-load impact loads. Correlation of the  $\text{LN}_2$  checkout test results with the proposed equation (the equation is developed in Section 6.3.2) are shown by Figures 6-3 and 6-4.

## 6.2 TESTS OF QUASI-COMPOSITE PANELS AT $\text{LH}_2$ TEMPERATURE

The point-load shots into  $\text{LH}_2$ -pressurized panels that were conducted during the initial phase of this effort produced different results than originally anticipated. Severe inward deformation and large tears were produced in both aluminum and titanium panels. A pattern of failure behavior as a function of stress level and projectile size (impacts essentially at constant velocity) was somewhat evident, but did not fit either basic fracture-mechanics or hypervelocity-impact damage concepts.

It was then discovered that a layer of some substance had formed on the front of the panels during each  $\text{LH}_2$  fill. The layer was dense and thick enough to completely arrest hypervelocity fragments of significant size. The layer was composed of cryopumped, liquified, and frozen elements of the residual common gases that remained after the range was pumped down to the normal operating pressure level. The Douglas Ballistic Range Tank was evacuated to a vacuum of 3mm Hg. absolute during each run. There was no visual check of the panel front-surface condition during the initial testing, because the fixture was inside a closed range tank. The existence of the layer of condensate was first deduced as an explanation of the strange panel behavior, then was verified by a photograph of the fixture taken by a remote-controlled, still camera during a dummy test run.

The basic results of the point-load shots into the quasi-composite panels are presented by Figures 6-5a through 6-5d. Complete details of the basic results of the impact shots are tabulated in Appendix D. This set of data, although inadvertently obtained, is representative of a composite structure composed of a main load-carrying shell upon which a layer of lower density material was directly attached. Some concepts of external insulation for

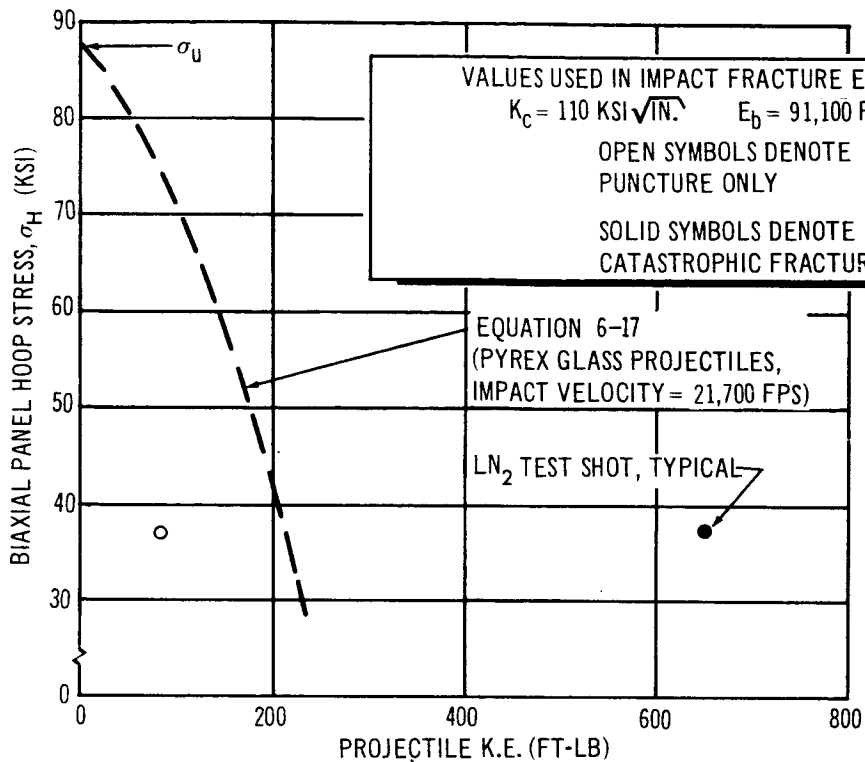


Figure 6-3. Correlation of LN<sub>2</sub> Checkout Tests with Impact Energy (Behavior of 0.032-in.-Thick 2219-T87 Aluminum)

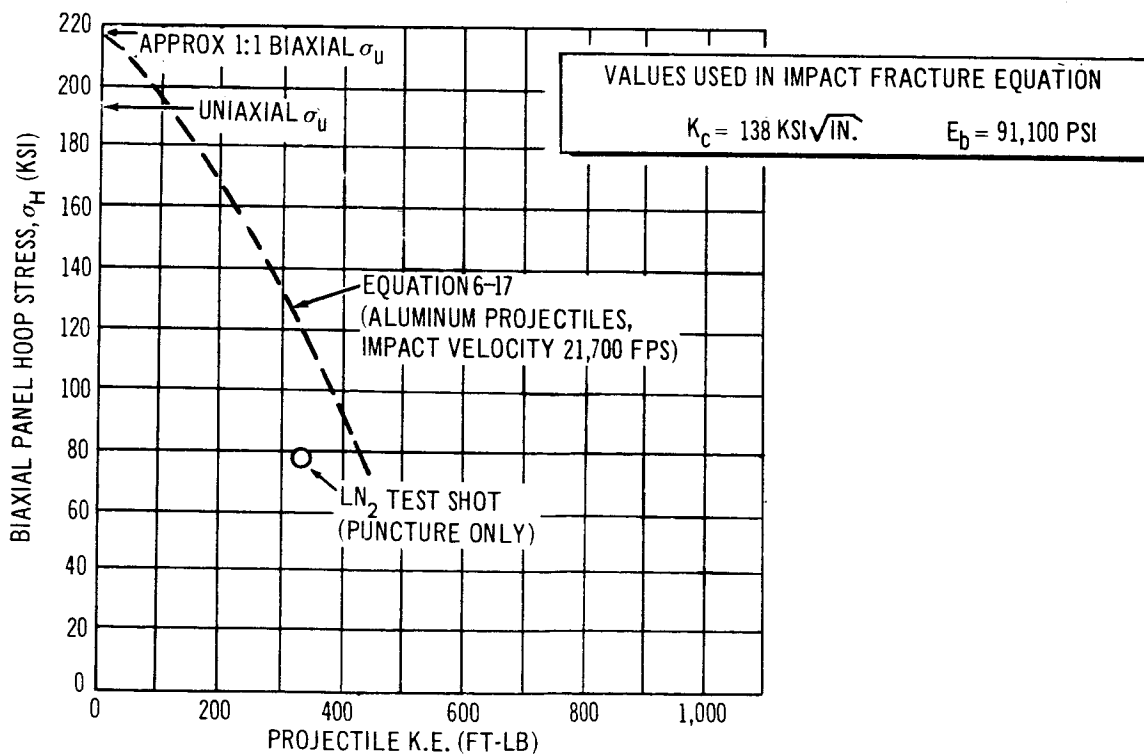
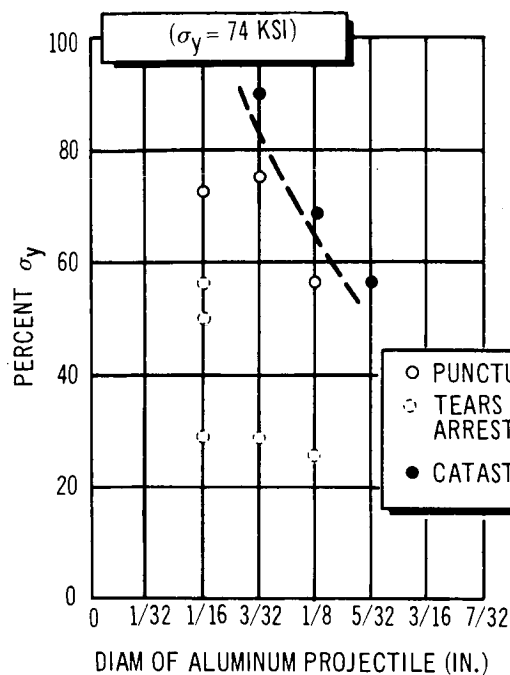
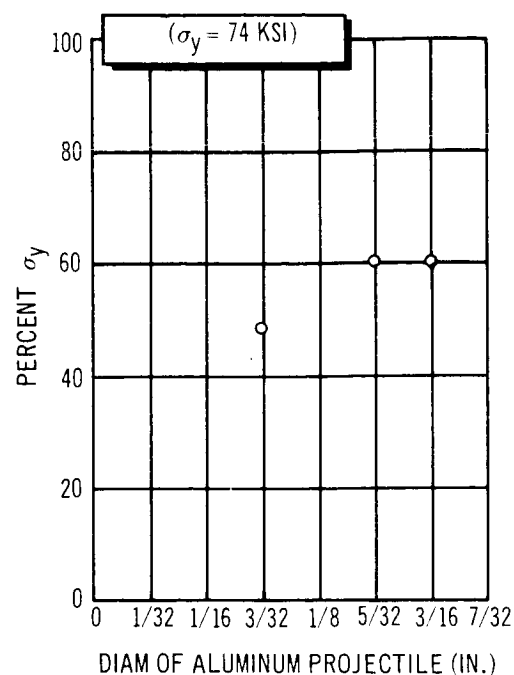


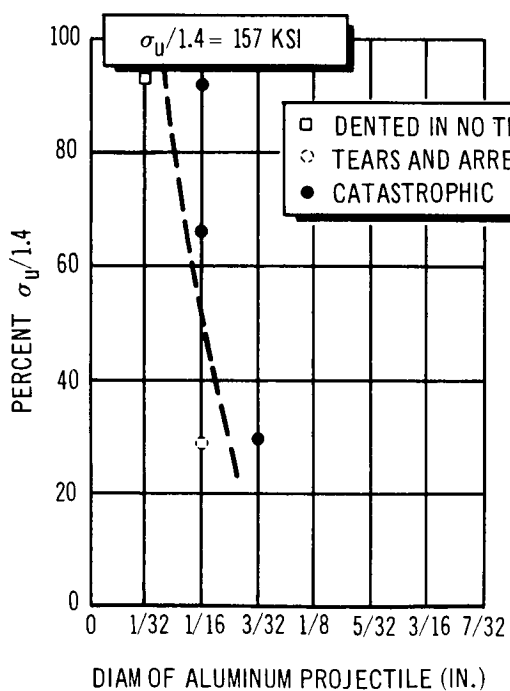
Figure 6-4. Correlation of LN<sub>2</sub> Checkout Tests with Impact Energy (Behavior of 0.036-In.-Thick 5Al-2.5 Sn(ELI) Titanium)



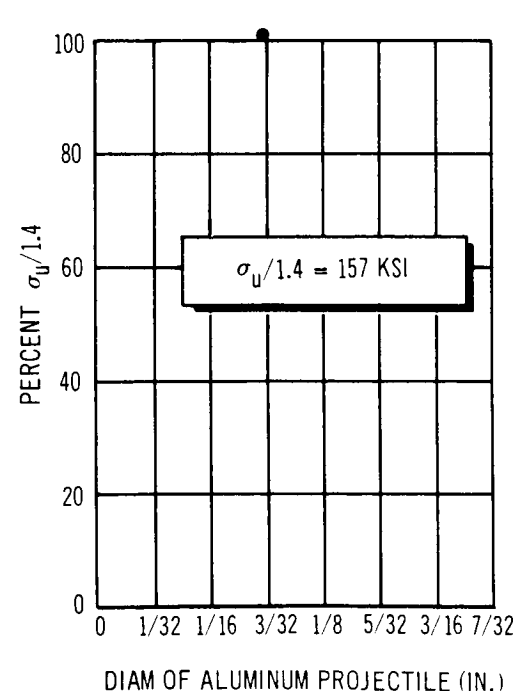
a. 0.032-IN.-THICK ALUMINUM PANELS



b. 0.125-IN.-THICK ALUMINUM PANELS



c. 0.015-IN.-THICK TITANIUM PANELS



d. 0.036-IN.-THICK TITANIUM PANELS

STRESS FIELD = 1:1, BIAxIAL FIXTURE FILLED WITH  $\text{LH}_2$  ( $-423^\circ\text{F}$ )

Figure 6-5. Results of Hypervelocity Impact Tests of Quasi-Composite Panels

cryogenic tanks are similar in physical nature. The damage to a quasi-composite structure can be more severe than the damage produced by direct impact of a hypervelocity projectile against an unprotected shell.

No quantitative measure of composition of the layer of condensate was obtained. The ice was eliminated for all subsequent testing. The actual thicknesses of the layer at the instant of projectile impact undoubtedly varied during each test run (dependent upon the time taken to charge the fixture with liquid hydrogen). Experimental evidence from one of the shots indicates the layer was at least 3/16-in. -thick; spray debris from a preliminary bumper-projectile impact chewed through the foam-rubber-insulation doughnut to within this distance of the panel surface of the panel, then was abruptly stopped.

The fracture characteristics of the  $\text{LH}_2$ -filled, quasi-composite panels as functions of panel hoop-stress and projectile-impact energy are shown by Figures 6-6 and 6-7 for the thin-gage aluminum and titanium panels. No fracture boundaries were obtained from the tests of the thicker gage panels. Also shown are plots of the equation that describes behavior of the unprotected (ice-free)  $\text{LH}_2$  tank shell structures. The composite panels fractured at much lower impact energy levels (for a given panel hoop-stress level) than those that produced catastrophic fracture of an unprotected panel.

Several of the impact shots produced large, jagged holes in the test panels; Figure 6-8 shows the front and back faces of an 0.032-in. -thick aluminum panel after being struck by a 3/32-in. -diam aluminum sphere. The final flaw size for this panel,  $l_f$ , (max. across tip of tears) was 3.0 in. This point, along with results from similar tests (where cracks arrested) are shown by Figure 6-9. Also shown is the fracture strength envelope of fatigue preflawed biaxial panels. It appears that the critical-stress fracture-envelope as a function of arrested tear size,  $l_f$  (under impact conditions), may be safely considered as 75% of the static biaxial burst values.

### 6.3 TESTS OF UNPROTECTED PANELS AT $\text{LH}_2$ TEMPERATURES

After it became evident that ice had formed on the panels during all of the early  $\text{LH}_2$  panels impact test shots and that the severe damage to the panels



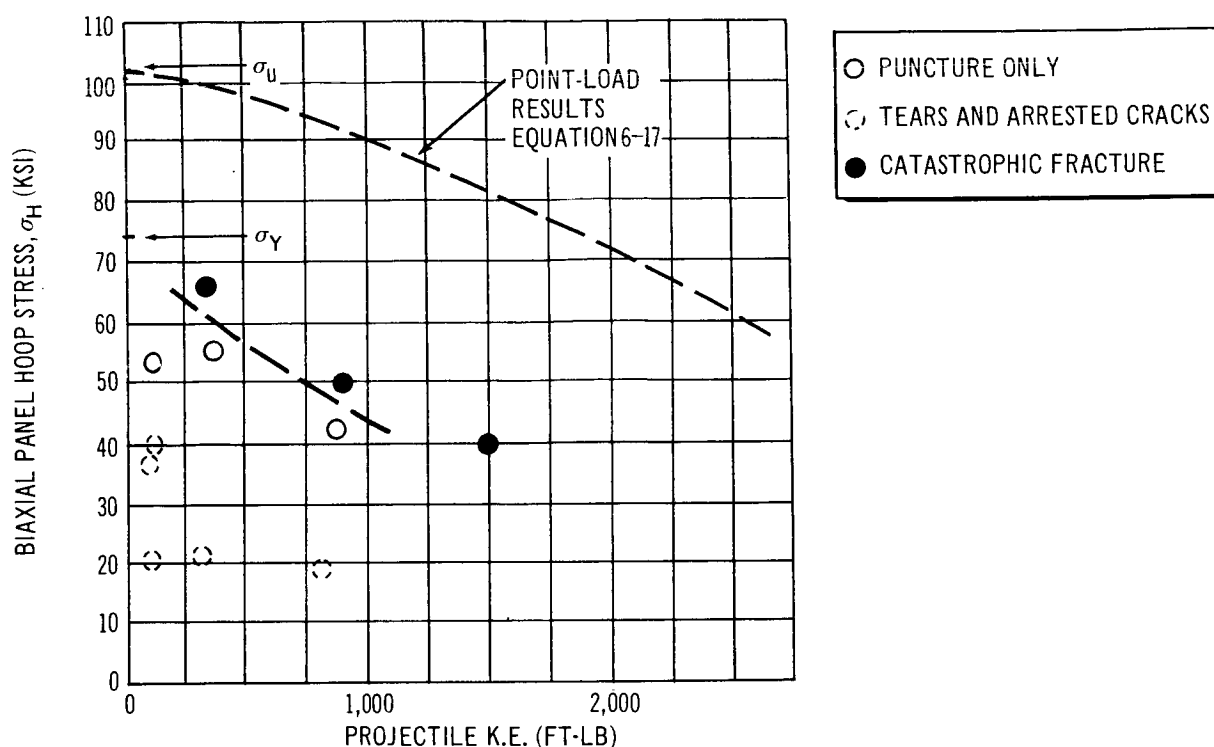


Figure 6-6. Correlation of Quasi-Composite Panel Test Results with Impact Energy (Behavior of 0.032-In.-Thick 2219-T87 Aluminum at LH<sub>2</sub> Temperature)

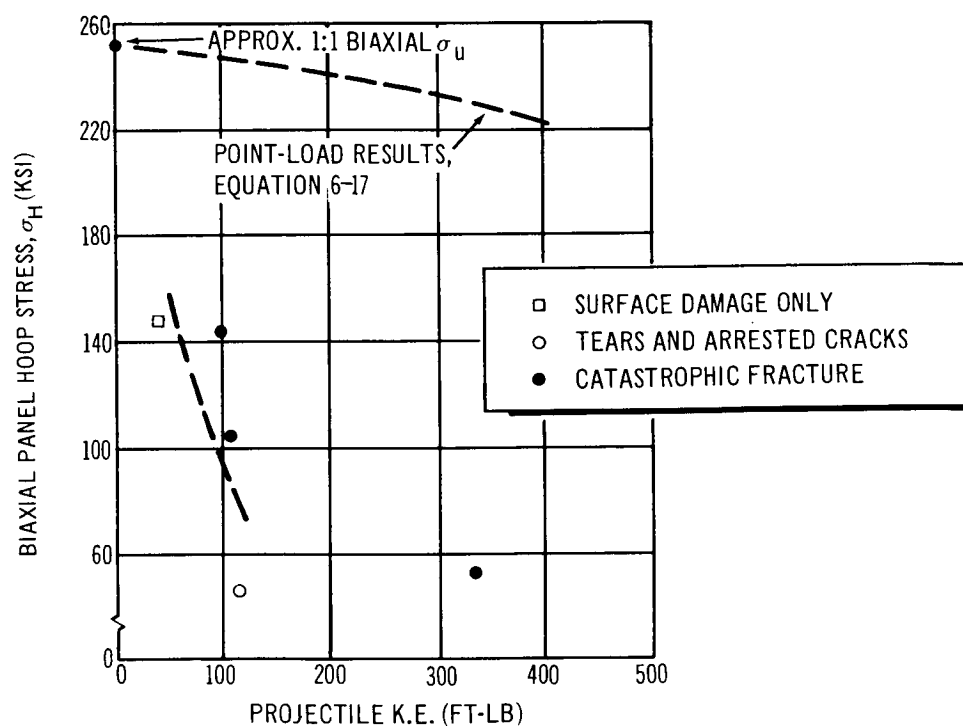
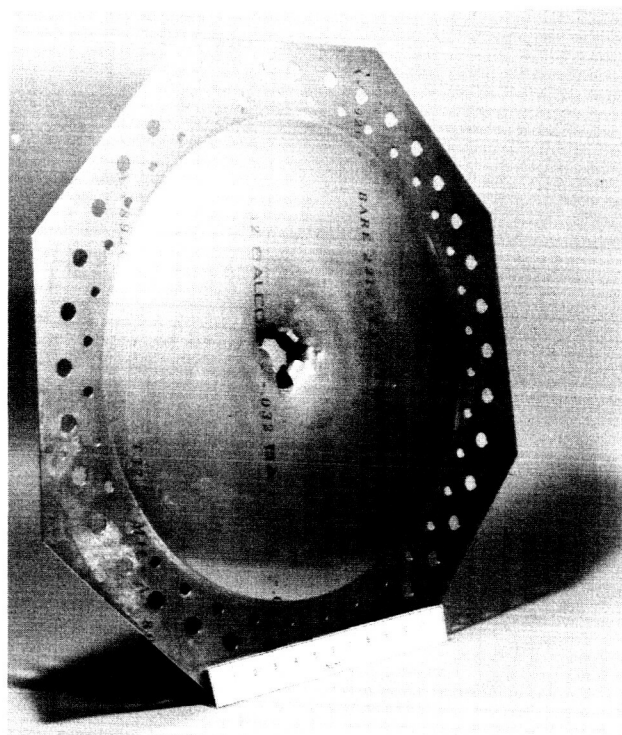
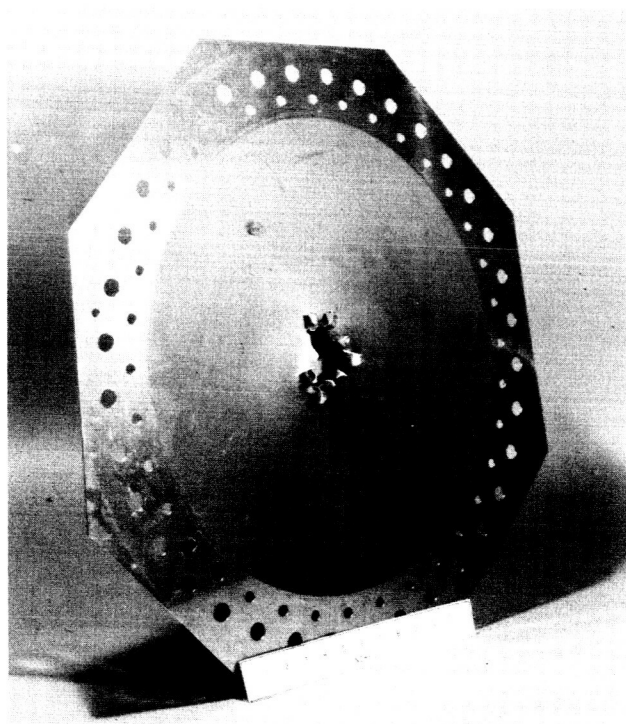


Figure 6-7. Correlation of Quasi-Composite Panel Test Results with Impact Energy (Behavior of 0.015-In.-Thick 5 Al-2.5 Sn (ELI) Titanium at LH<sub>2</sub> Temperature)



FRONT FACE



BACK FACE

Figure 6-8. Typical Results of Point-Load Tests of Quasi-Composite Panels  
(Behavior of 0.032-In.-Thick 2219-T87 Aluminum at LH<sub>2</sub>  
Temperature)

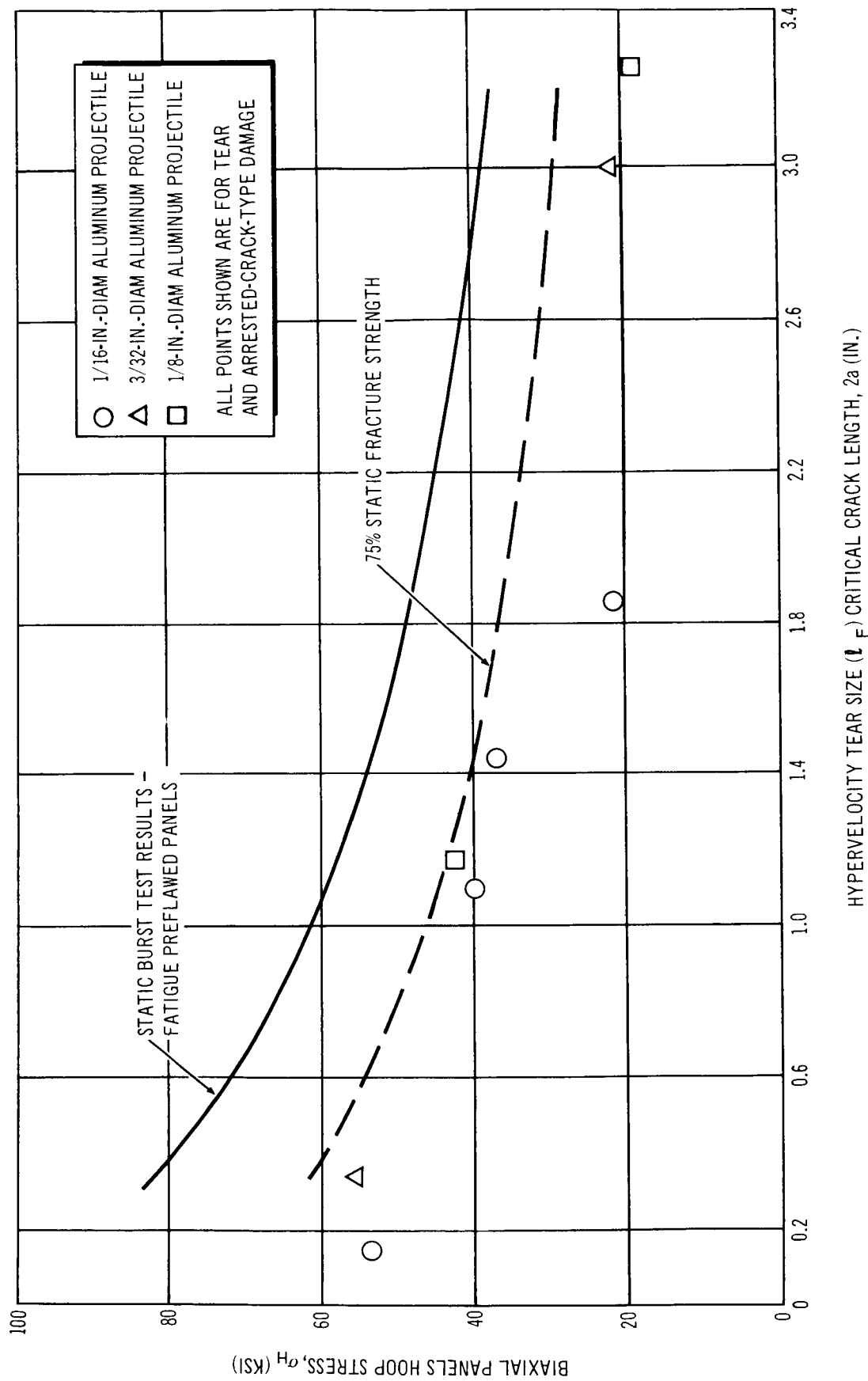


Figure 6-9. Fracture Strength of Impact Damaged Quasi-Composite Biaxial Panels (Behavior of 0.032-in-Thick Aluminum Alloy at LH<sub>2</sub> Temperature)

had been caused by the interaction of the projectile and the ice prior to the actual contact of projectile material with the panel, immediate action was taken to eliminate the ice. The front of the biaxial test fixture was screened from the range atmosphere with a bag or tent made of 1/2-mil polyethylene sheet. The bag was filled and purged with helium during the chill down cycle. Repeat shots were made of tests that had been conducted earlier. A periscope system was also added to visually monitor the apparatus inside the range tank to the time of the shot. The helium blanket eliminated the ice.

During two of the shots (57 and 58) that were conducted shortly after the helium purge tent was added, the projectile broke up preceding impact on the target. The break-up was attributed to interaction of the hypervelocity projectile with the sheet material of the tent that surrounded the front of the biaxial test fixture. Initially the tents were fitted loosely on the fixture; it was hypothesized that the projectiles hit layers of folds of the tent material. The design was modified slightly such that only one sheet (of 1/2-mil polyethylene) of the tent could possibly traverse the line-of-flight of the projectile. Projectile break-up did not reoccur.

The repeat shots proved that the ice formation had a significant effect on panel fracture behavior. The severe deformations and tears did not reoccur. Either simple punctures or punctures plus catastrophic fractures were produced. Testing was then continued with the panels maintained free of any condensates, and a complete set of data on behavior of unprotected panels under point-load impact conditions was obtained. Results are tabulated in Appendix D, and basic results are also shown in graphical form by Figures 6-10 through 6-13. The figures also show the correlation of the basic test data to a master curve representation of impact behavior that is developed in Section 6.3.2 of this report. The fracture behavior of the thin-gage aluminum and the thin-gage titanium panels, under the point-load conditions, was established for two different working-stress levels in each panel material.

Projectiles as large as 0.58g (0.350-in. diam) Lexan cylinders were fired at the thick-gage aluminum panels, but only simple punctures were produced.

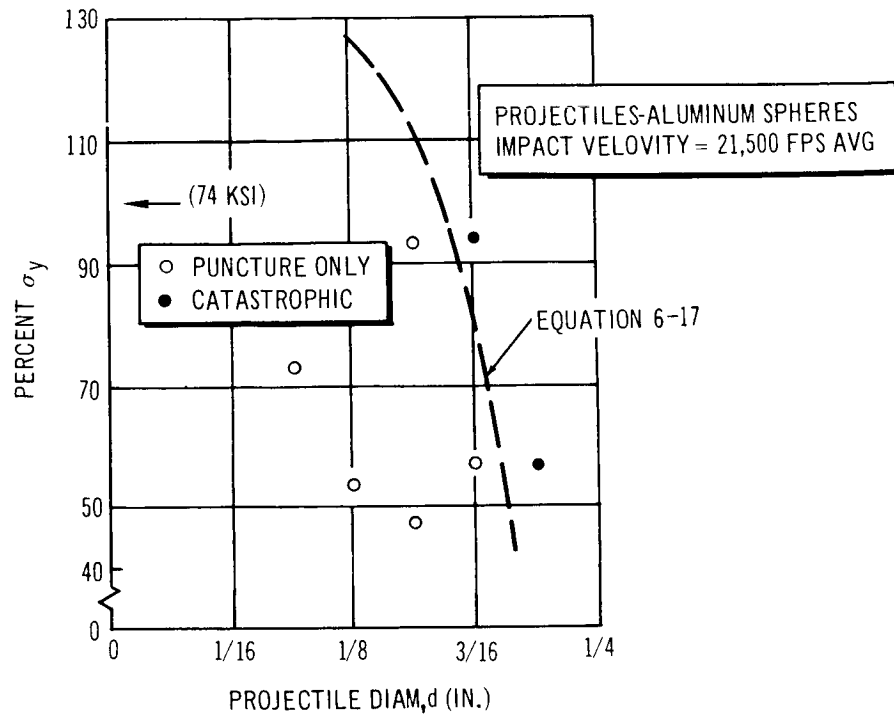


Figure 6-10 Results of Biaxial Panel Point-Load Tests (Behavior of 0.032-In.-Thick 2219-T87 Aluminum at LH<sub>2</sub> Temperature)

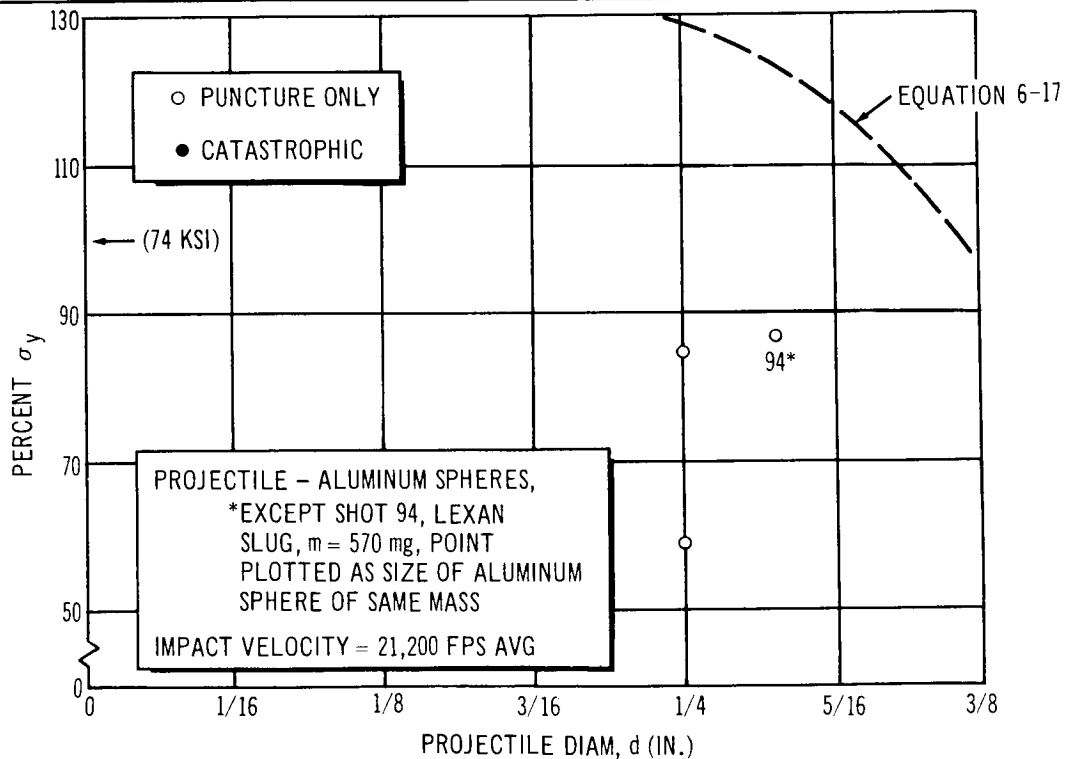


Figure 6-11. Results of Biaxial Panel Point-Load Tests (Behavior of 0.125-In.-Thick 2219-T87 Aluminum at LH<sub>2</sub> Temperature)

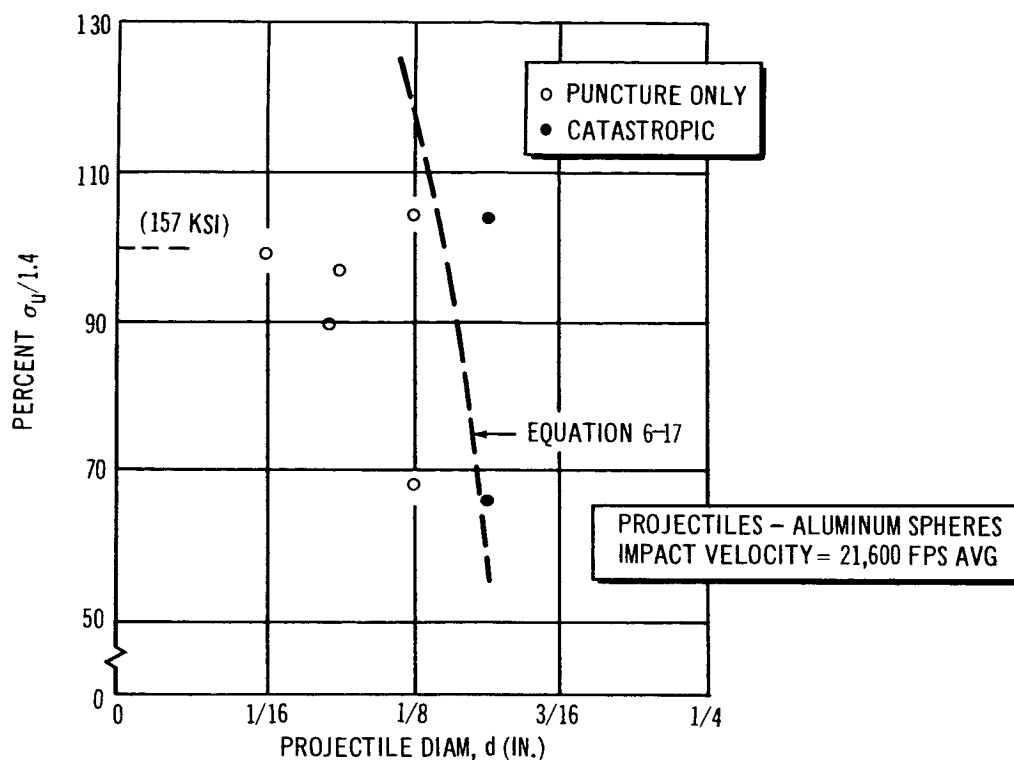


Figure 6-12. Results of Biaxial Panel Point-Load Tests (Behavior of 0.015-In.-Thick 5 Al-2.5 Sn (ELI) Titanium at LH<sub>2</sub> Temperature)

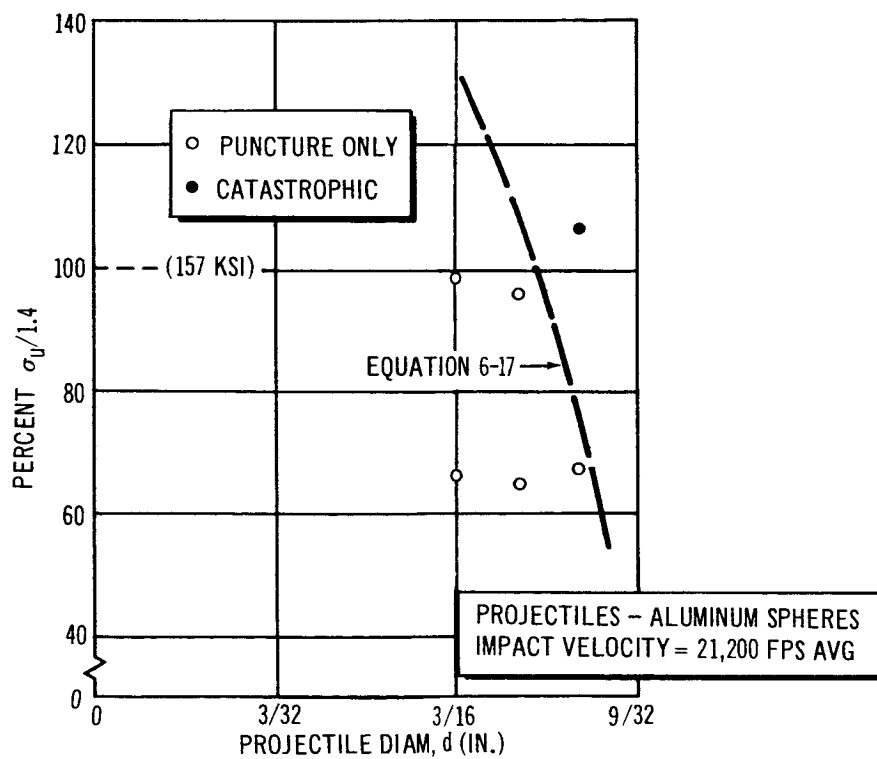


Figure 6-13. Results of Biaxial Panel Point-Load Tests (Behavior of 0.036-In.-Thick 5 Al-2.5 Sn (ELI) Titanium at LH<sub>2</sub> Temperature)

Post-test examination of the panel which was hit by the largest projectile (Panel 125A#B02, Shot No. 94) indicated that the impact-loading parameters of this test were close to those that would produce catastrophic fracture. The degree of general yielding in the region adjacent to the puncture was geometrically similar to that of the thin-gage aluminum panels which were subjected to critical impact loadings. As projectile sizes increased during an impact test sequence, the resulting higher shock overpressures in the fluid contained by the panel produced more severe outward bulge deformations in the panel around the punched hole. During the correlation of the point-load impact test data, it was estimated that the data point for Panel 125A#B02 fell a short distance (qualitatively) below the fracture boundary.

Projectiles as large as 0.38 g (1/4-in.-diam aluminum spheres) were launched against the thick-gage titanium panels. The fracture boundary was established for the higher stress level in the panel. Impact of a large aluminum projectile produced only a simple puncture under lower stress-level conditions. No large Lexan cylinders were launched during the thick-gage, titanium test sequence.

Typical results of point-load tests of unprotected panels are shown by Figures 6-14 and 6-15.

The first approach for analysis of the point-load impact data was to compare impact behavior as a function of hypervelocity puncture size,  $l_0$ , with the results obtained from the static fracture tests of biaxial panels (Figures 6-16 through 6-19). It is evident that the static fracture relations do not describe hypervelocity impact results, and that the overpressure loading from the  $\text{LH}_2$  shock must have a dominant influence on dynamic fracture behavior. The correlation of the impact data with the yet-to-be-described master curve representation is shown.

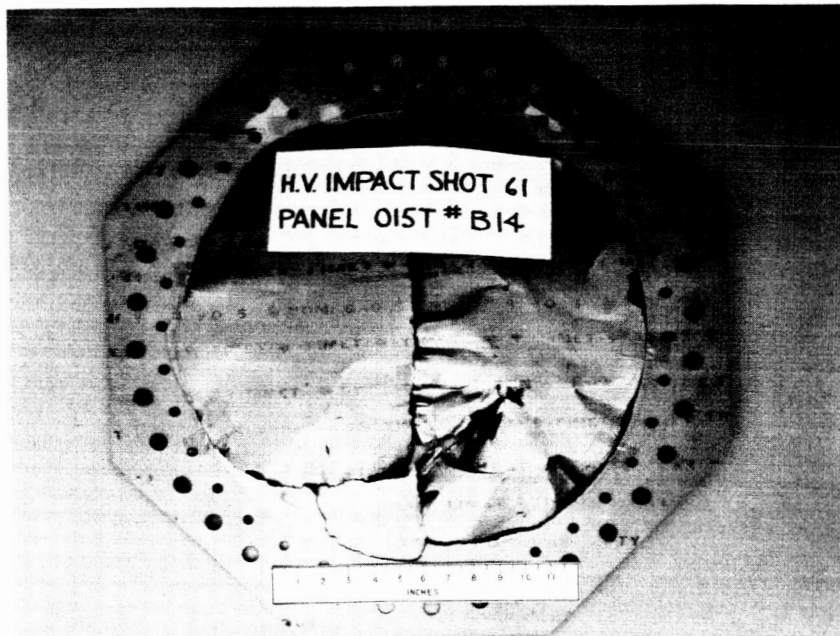
A relation that defines hypervelocity puncture size in thin shields (Reference 16) is the following:

$$D/d = 0.45 V (t_s/d)^{2/3} + 0.90 \quad (6-1)$$



0.032-IN-THICK PANEL  
PROJECTILE = 7/32-IN.-DIAM ALUMINUM SPHERE

Figure 6-14. Results of Point-Load Tests of 2219-T87 Aluminum Panels



0.015-IN-THICK PANEL  
PROJECTILE = 5/32-IN.-DIAM ALUMINUM

Figure 6-15. Results of Point-Load Tests of 5 Al-2.5 Sn (ELI) Titanium Panels



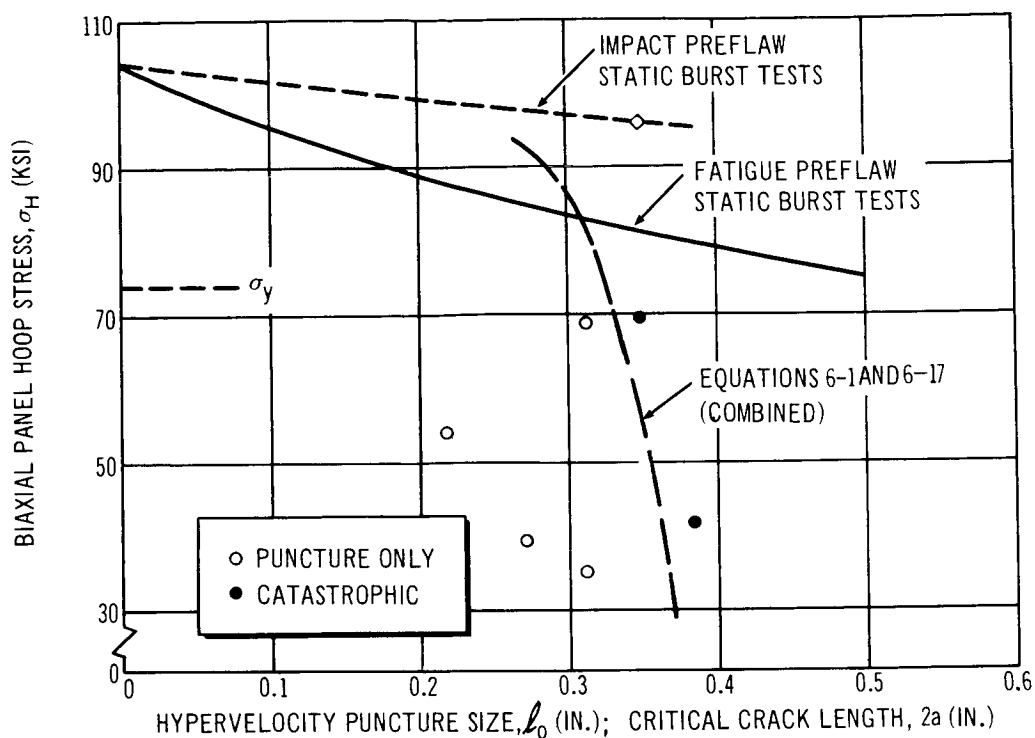


Figure 6-16. Comparison of Biaxial Panel Point-Load Impact Tests with Static Burst Tests of Pre-flawed Panels (Behavior of 0.032-In.-Thick 2219-T87 Aluminum at LH<sub>2</sub> Temperature)

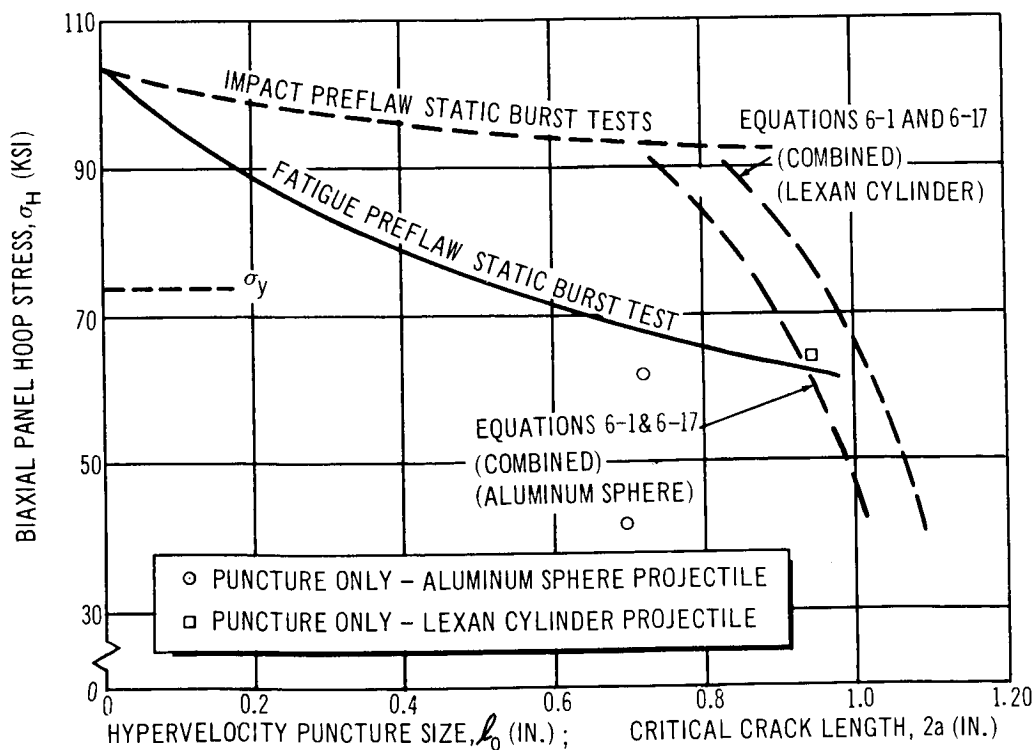


Figure 6-17. Comparison of Biaxial Panel Point-Load Impact Tests With Static Burst Tests of Preflawned Panels (Behavior of 0.125-In-Thick 2219-T87 Aluminum at LH<sub>2</sub> Temperature)

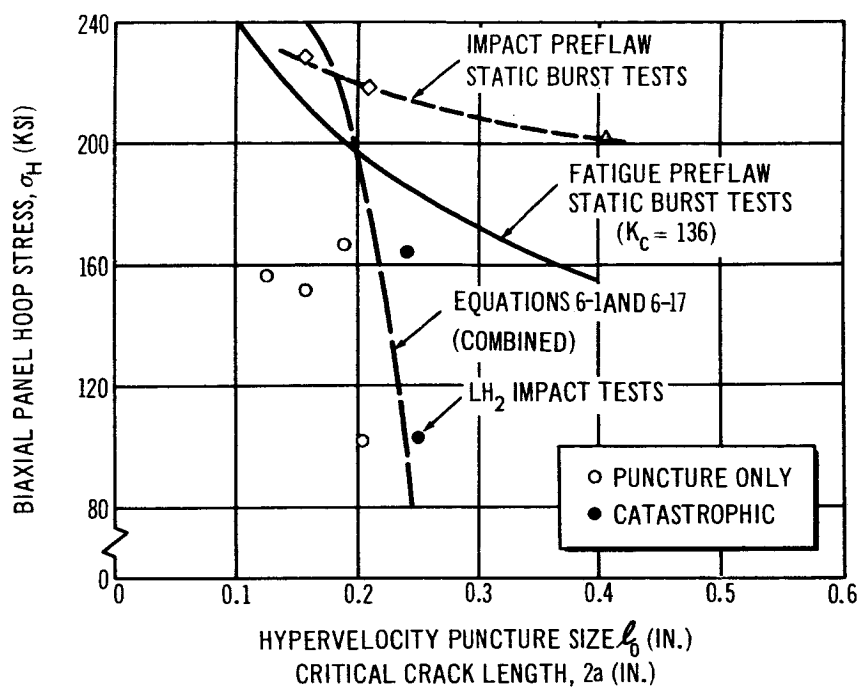


Figure 6-18. Comparison of Biaxial Panel Point-Load Impact Tests with Static Burst Tests of Preflawn Panels (Behavior of 0.015-In-Thick 5 Al-2.5 Sn (ELI) Titanium at  $LH_2$  Temperature)

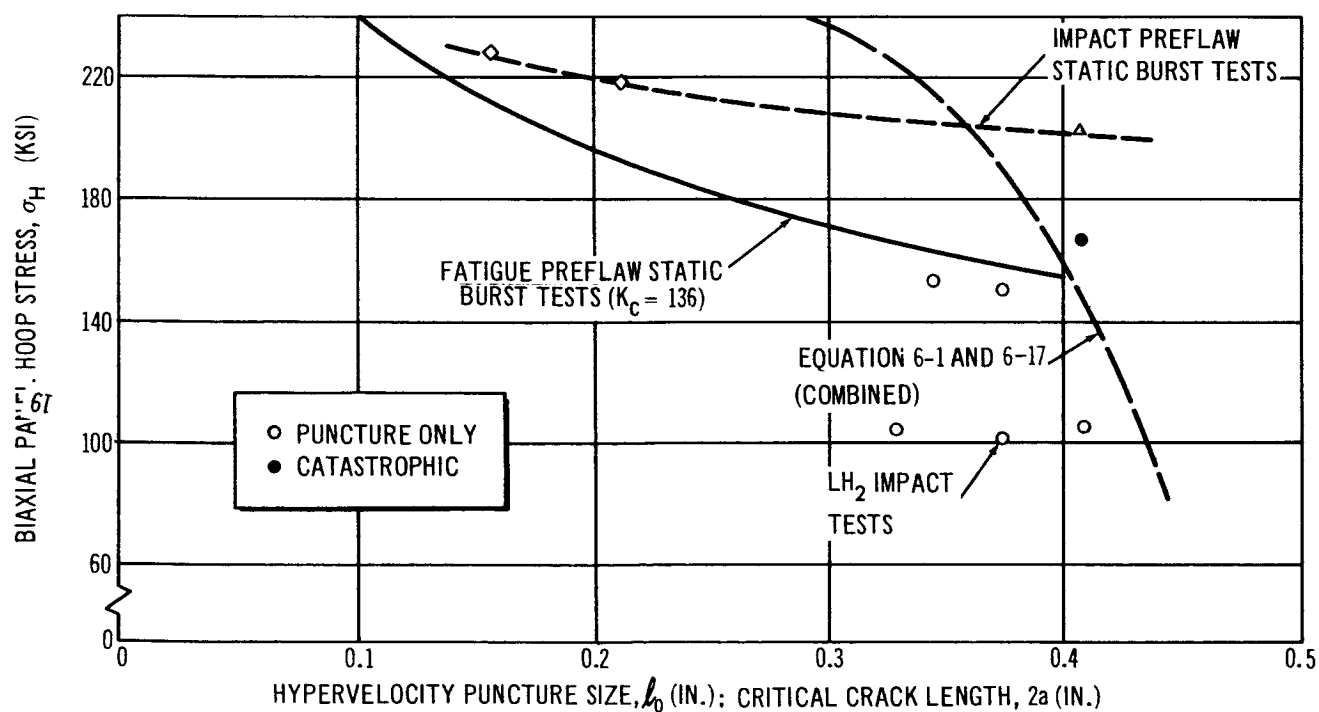


Figure 6-19 Comparison of Biaxial Panel Point-Load Impact Tests with Static Tests of Preflawn Panels (Behavior of 0.036-In-Thick 5 Al-2.5 Sn (ELI) Titanium at  $LH_2$  Temperature)

where

V is measured in km/sec

This relation was combined with the master curve representations to construct the curves shown. Equation 6-1 was checked by comparing the relation with results of Douglas impact tests on actual sheets of the test panel material and on the panels themselves. The prediction of hole size was accurate.

### 6.3.1 Analysis of LH<sub>2</sub> Shock Wave Data

At the onset of the investigation, it was known that a shock wave overpressure would be produced in the LH<sub>2</sub> chamber. It was presumed that an understanding of the LH<sub>2</sub> shock would be essential if impact behavior correlation studies were to be made. This is the reason the dynamic pressure transducers were installed in the LH<sub>2</sub> chamber of the biaxial test fixture.

The relative time of arrival of the LH<sub>2</sub> shock wave at each of the three instrumentation stations was obtained during numerous runs, the radial propagation of the shock as a function of time after impact was calculated, and the nature of the shock as a function of projectile kinetic energy was characterized by the Chou method (Reference 3). This subsection reviews Chou's method, describes special techniques used to handle the LH<sub>2</sub> shock wave data, and presents an equation for LH<sub>2</sub> shock behavior.

Chou assumes (1) that hypervelocity impact into a fluid-filled tank creates a hemispherical shock wave in the contained fluid, (2) that energy is released immediately after impact, (3) that Hopkinson's scaling law applies, and (4) that shock front velocity approaches sonic velocity at long times. He presents the following semiempirical equation for shock wave radius as a function of time.

$$R = c_o t + A (K.E.)^{1/3} \log_e \left[ \frac{2c_o}{R_o} (t + t_o) \right] \quad (6-2)$$

which assumes that the shock can be characterized as a function of kinetic energy. While not strongly advocating the energy correlation, Chou shows

that the relation yields good results for analysis of high-speed impact into water-filled tanks.

The shock front velocity is obtained by differentiating Equation 6-2 with respect to time which gives:

$$U = c_o + \frac{A(K.E.)^{1/3}}{(t + t_o)} \quad (6-3)$$

where

- R = shock wave radius
- t = time
- c<sub>o</sub> = sonic velocity
- K.E. = kinetic energy of the projectile
- R<sub>o</sub> = characteristic length of the projectile
- t<sub>o</sub> = a constant
- A = a constant
- U = shock velocity

Projectile characteristic length was taken as the projectile radius, d/2.

Because R must be zero when t is zero:

$$\log_e \left[ \frac{2c_o}{R_o} (0 + t_o) \right] = 0$$

$$\frac{4c_o}{d} (t_o) = 1$$

$$t_o = \frac{d}{4c_o} \quad (6-4)$$

The basic data for determining the LH<sub>2</sub> shock wave radius as a function of time was furnished by the dynamic pressure transducer oscillograms and by careful measurements of test-apparatus and specimen geometry. The relative time of arrival of the shock at each instrumentation can be read to approximately 1 μsec; a typical time interval between stations is approximately 20 μsec. The location of the impact point of each panel was measured

(post test) and a geometric layout was made to determine shock path distances for each panel (Figure 6-20). Actual panel contours, as measured by the spherometer instrumentation, were used in the layouts.

It was assumed for point-load tests that the shape of the shock was spherical and that it was centered at the impact point on the face of the panel. Shock wave radius as a function of time (after arrival of the shock at transducer  $K_1$ ) can then be readily determined.

The time after impact,  $t$ , is not known directly, but was determined by a fit of the empirical data to Equation 6-2. A typical example is shown by Figure 6-21. Values of  $A$  for several runs, as calculated by the noted procedure, are shown by Figure 6-22. The arithmetic average of  $A$  for the points shown is  $0.0657 \text{ in.}/(\text{ft-lb})^{1/3}$ ; however, the magnitude of the value of the "constant" shows a tendency to decrease as the size of the projectile (also K.E. because shots were made at essentially constant velocity) increases. This implies that  $A$  is not a pure constant. The downward slope of the curve is relatively small; the value of  $A$  changes approximately 30% over a K.E. range that spans three orders of magnitude.

The downward slope of the curve with increasing projectile size can be explained in part by the deviation of the actual impact process from the assumption that energy is released immediately after impact. At a test velocity of 21,000 fps, or approximately  $1/4 \text{ in.}/\mu\text{sec}$ , a  $1/16\text{-in.}$ -diam projectile is engulfed by the target in  $0.25 \mu\text{sec}$ . The larger projectiles require a time period up to  $1.5 \mu\text{sec}$  after initial contact to completely interact with the target. A finite time span for release of impact energy results in a weaker shock than that which would result from an instantaneous release of projectile K.E.

The effect on shock behavior caused by the projectile striking the tank wall before entering the fluid is of some concern. Equation 6-2 does not include assumptions to cover interaction of the projectile with the tank wall. A simple analysis on partition of projectile energy was made. For geometrically similar impact conditions, that is, for a given ratio of projectile diameter,  $d$ , to the tank wall thickness,  $t_s$ , percentages of partition of

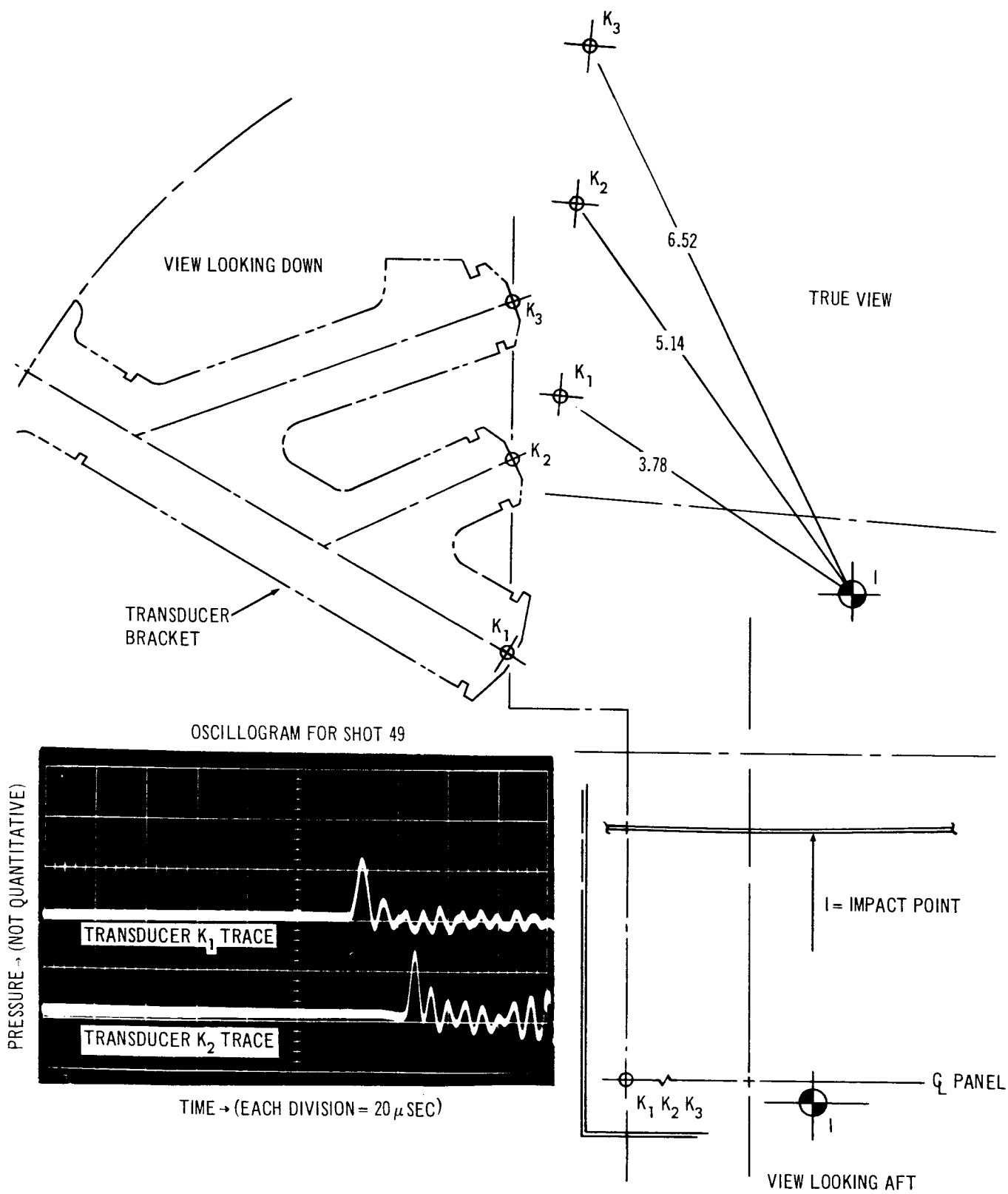


Figure 6-20. Layout to Determine Shock Path Geometry (Shot No. B-8.2-49, Panel No. 032A NO. B20 )

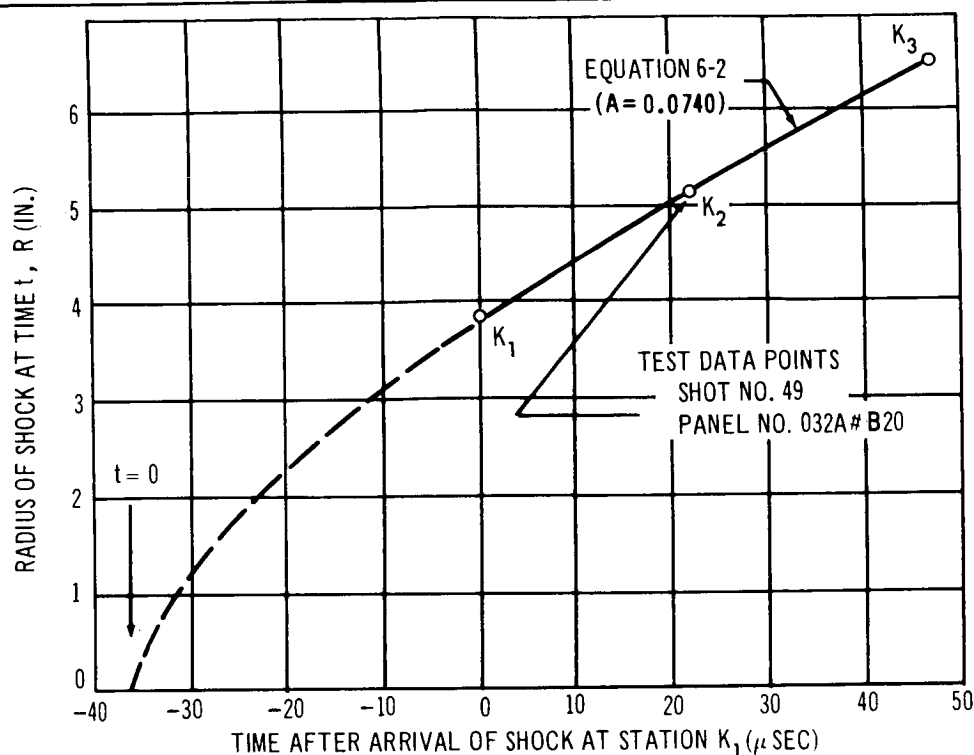


Figure 6-21. Correlation LH<sub>2</sub> Shock Measurements with Chou's Equation

energy to the various energy-absorbing elements should be equivalent (assuming there are no size effects other than discussed above).

The method selected for estimating energy absorbed by the tank wall compared the ratio of tank wall volume removed by the hypervelocity puncture to the volume of the crater in a semi-infinite target of the same material when impacted by the same size projectile. The crater depth in 2219-T87 aluminum is estimated to be the same as that produced by impact into a 2024-T3 aluminum semi-infinite target. From Reference 16, the semi-infinite target penetration depth  $P_\infty$ , is approximately  $(2.0)d$  for the impact of an aluminum projectile into 2024-T3 aluminum at 6.6 km/sec or 21,700 fps. Assuming a hemispherical crater in the semi-infinite target (an approximation; at the impact velocities under consideration, material strength of the stronger aluminum alloys has a significant influence on the type of crater formed, see References 16 and 17) the ratio of the wall-puncture volume,  $v_{ts}$ , to semi-infinite target crater volume,  $v_\infty$  (aluminum projectile impacting a 2219-T87 aluminum target) is:

$$\frac{v_{ts}}{v_\infty} \approx \frac{3}{64} \left( \frac{t_s}{d} \right)^2 (D/d)^2 \quad (6-5)$$

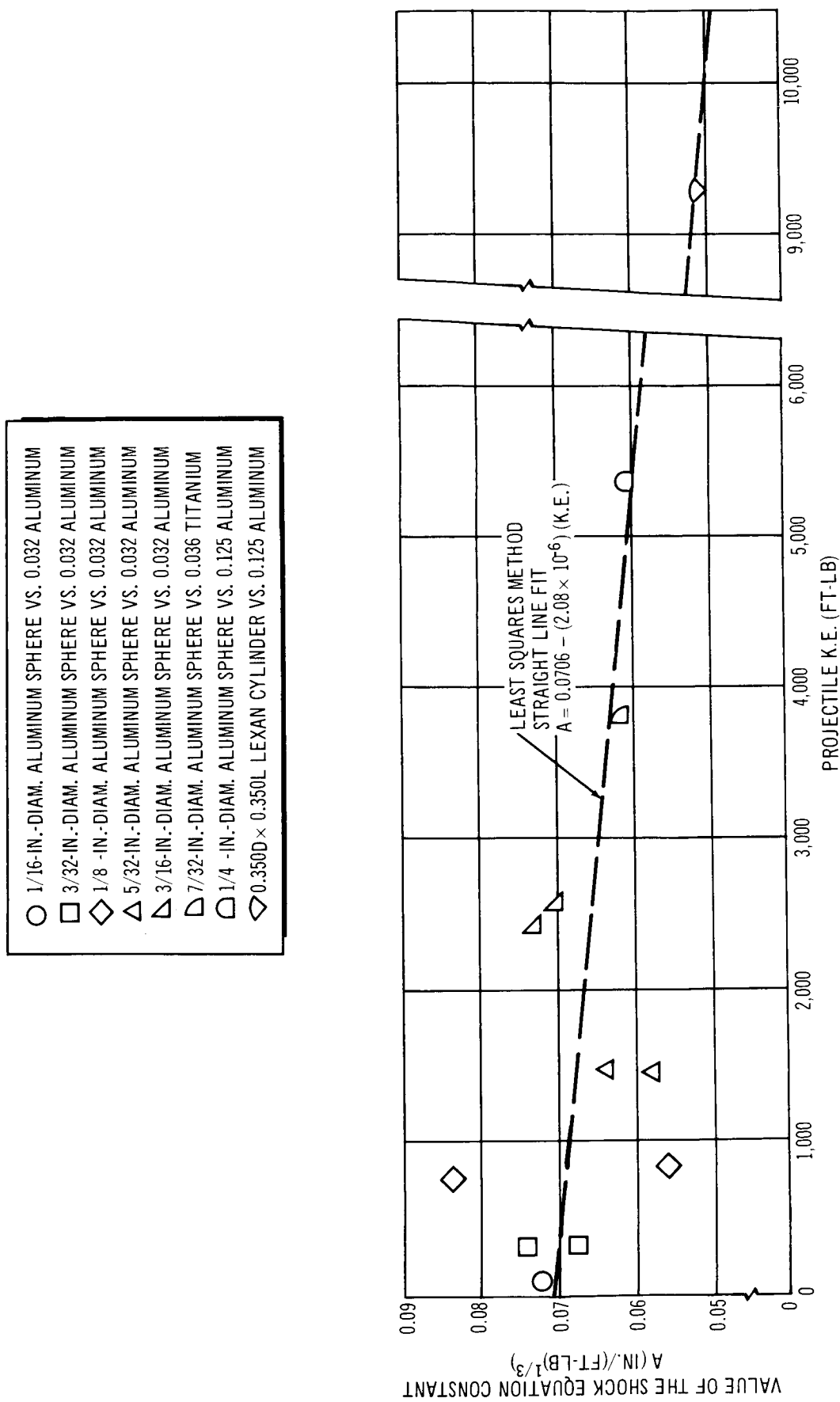
Combination of Equation 6-5 with Equation 6-1 gives the following results:

$d/t_s$	$D/d$	$v_{ts}/v_\infty$
2	2.77	0.180
4	2.08	0.051
6	1.80	0.025

If none of the energy used to form the puncture in the tank wall were transmitted to the contained fluid, the percentage of total projectile K.E. lost would range from approximately 2% to 20% for the panel geometrical configurations tested. Values of  $d/t_s$  for the points shown by Figure 6-22 range from 1.95 to 5.85 for the 0.032 in. -thick aluminum panels and from 2 to approximately 3 (assuming the Lexan cylinder or equivalent aluminum sphere as the projectile) for the 0.125-in. -thick aluminum panel. The  $d/t_s$  for the titanium panel data point is 6.1.

Much of the energy used to puncture the tank wall is in turn transmitted to the contained fluid by wall-fragment debris which are propelled inward. Therefore, the percentages of energy loss noted previously are upper limits; actual percentages are less. Order-of-magnitude estimates are made here that 50% of the tank-wall, hole-formation energy is transmitted to the fluid. A precise correlation analysis of the  $LH_2$  shock data could be made by utilizing the numerical calculations of Bjork (Reference 18), or of Walsh, et al (References 19 and 20); however, such complex analysis is beyond the scope of the current research. Results of data correlation analysis using the residual K.E. concept are shown in Figure 6-23. The residual K.E. is the total projectile K.E. less the K.E. estimated to be irretrievably absorbed by the tank wall during the initial impact process. Corrections were also made using the Summers penetration equation (Reference 17) for the Lexan projectile compared to aluminum panel and the aluminum projectile compared to titanium panel data analysis. These corrections account for materials other than aluminum when using Equation 6-5. Figure 6-23 also shows the distance each point is displaced from the corresponding data point of Figure 6-22. It is evident that for the panel configurations tested the presence of the wall has little effect on the fit of the  $LH_2$  shock data to Chou's equation. The value of the shock constant,  $A$ , still decreases as projectile size increases. The change occurs at essentially the same rate as that shown by Figure 6-22. Since there is always a wall



Figure 6-22. Correlation of LH<sub>2</sub> Shock Data with Chou's Equation



containing the cryogenic propellant, the shock characterization shown by Figure 6-22 is adequate for engineering use.

The LH<sub>2</sub> shock-wave data was obtained at finite times after impact. Data reduction indicates the time of arrival at transducer station K<sub>1</sub> after the instant of impact ranges from 30 μsec for a low-energy impact to 12 μsec for a high-energy impact. Shock velocities at the instrumentation stations for low-energy impacts are only slightly in excess of the sonic velocity. This explains why values of the empirical constant, A, show considerable scatter at the low end of the impact energy range.

Observed shock velocities (calculated by Equation 6-3 using the value of A as determined for each particular shot) that occurred during tests using the higher energy projectiles are significantly in excess of the sonic speed, c<sub>0</sub>, in LH<sub>2</sub>. For example, for shot No. 94, having an impact energy input of 9,300 ft-lb, the observed LH<sub>2</sub> shock velocity at instrumentation station K<sub>1</sub> was 2.6 times the sonic velocity; and at station K<sub>3</sub>, the LH<sub>2</sub> shock velocity was 1.4 times the sonic velocity. Figure 6-24 shows a comparison of typical shock-wave data for high- and low-energy shots.

Therefore, the shock wave in LH<sub>2</sub>, which is contained in a cryogenic tank of the geometry investigated by this research, may be considered characterized by the relation

$$R = 0.0472t + 0.0657 (K.E.)^{1/3} \log_e \left[ \frac{0.189}{d} (t) + 1 \right] \quad (6-6)$$

where

R is measured in inches

t is measured in μsec

K.E. is measured in ft-lb

d is measured in inches

The kinetic energy range of the test data which was used to calculate the constants of the shock equation spans the pertinent range for most meteoroid studies.

There is some evidence that the equation might not accurately describe the shock at smaller times than measured by the dynamic pressure instrumentation system. Additional research at Lewis Research Center (References 21 and 22), beyond the research reported in Reference 2, has recently been

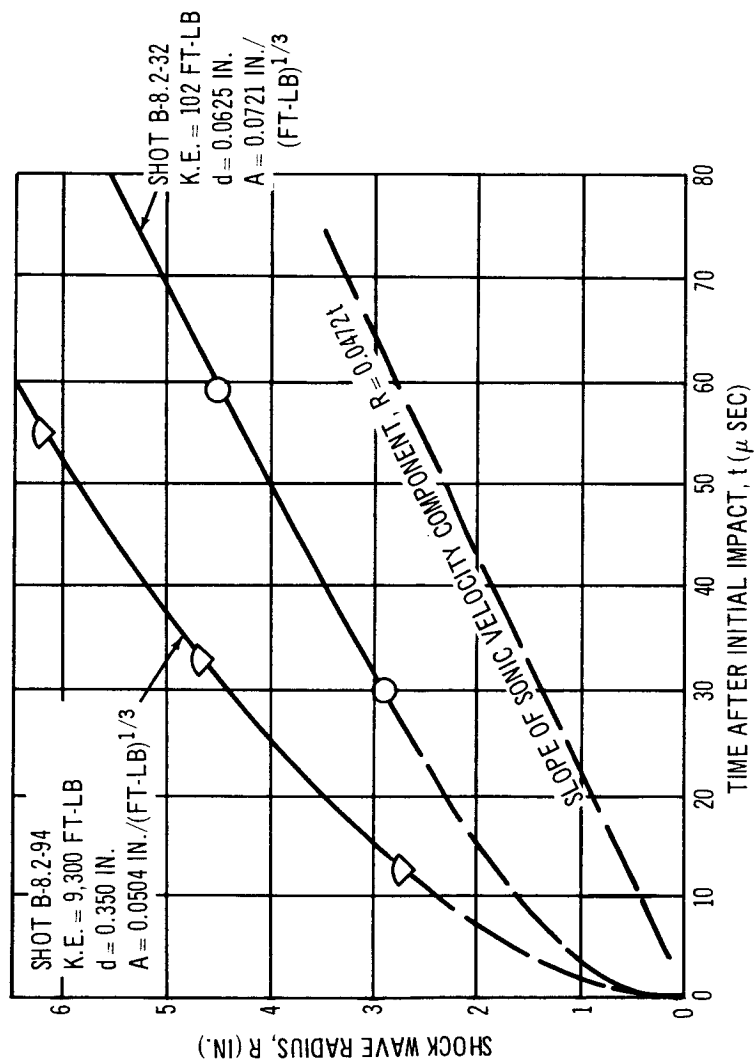


Figure 6-24. Fit of Chou's Equation to High- and Low-Energy Shots

completed on the nature of propagating shock waves in water-filled tanks. The Lewis group reported that correlation of the new water-filled tank data with the method of Reference 3 (basically the same as Equation 6-2), using a projectile characteristic length,  $R_o$ , which was proportional to projectile size, did not give as good results as those obtained when a constant  $R_o$  was used and assumed to apply to all sizes of projectiles. A high-speed framing camera was used to photorecord the propagation of the shock front in water; data was obtained at times as low as approximately a few  $\mu\text{sec}$ . Impacts were made directly into the contained water through prepunched holes in the target panels.

After review of the Lewis work, it was decided that examination of possible lack of dependency of projectile size in the shock equation might yield additional insight regarding the nature of the  $\text{LH}_2$  shock. Some work using this approach was accomplished. It must be recognized that the data from the  $\text{LH}_2$  tests are not directly comparable to the results of the Lewis research. Different experimental approaches and instrumentation techniques were used, and data on the  $\text{LH}_2$  shock at the small times are not available.

Calculations were made to fit the  $\text{LH}_2$  data to Equation 6-2 which was modified by replacing the variable projectile size,  $R_o = \frac{d}{2}$ , by a standard (constant) projectile size,  $R_o = \frac{d_o}{2}$ . A value for the standard projectile diameter,  $d_o$ , was chosen as  $7/32$  (0.219) in. This size is in mid-range of the sizes used during the  $\text{LH}_2$  experiments, and also is essentially the same as that of the projectiles used during the initial water-filled tank research (References 2 and 3).

Correlation of the  $\text{LH}_2$  shock data neglecting the effect of projectile size did not improve the fit of the  $\text{LH}_2$  data to the shock equation shown by Figure 6-22. Calculated values of  $A$  were found to be slightly smaller for data points associated with the larger projectiles, and were slightly larger for data points associated with the smaller projectiles. Thus, the downward slope of the curve of the constant,  $A$ , as a function of K.E. still existed. It was concluded that measurements of the  $\text{LH}_2$  shock at smaller times after impact would be necessary before additional correlation analysis would be warranted.

If the compressibility (Rankine-Hugoniot relation) of the fluid is known, the peak pressure behind the shock can be calculated. A precise relation for

LH<sub>2</sub> at very high pressures is not known;\* however, pertinent LH<sub>2</sub> compressibility, at relatively low pressures as well as sonic velocity, is given by Scott (Reference 23). Pertinent LH<sub>2</sub> characteristics (at temperature = 20°K) are as follows:

1. Sonic velocity,  $c_o$

$$\begin{aligned} c_o &= 1,199 \text{ m/sec} \\ &= 3,930 \text{ fps} \end{aligned}$$

2. Density,  $\rho_o$

$$\rho_o = 0.0712 \text{ g/cm}^3$$

3. Adiabatic compressibility (calculated),  $D_b$

$$\begin{aligned} D_b &= \frac{\left[ \frac{v_o - v}{v_o} \right]}{p - p_o} \\ &= 977 \times 10^{-12} \text{ cm}^2/\text{dyne} \end{aligned} \quad (6-7)$$

The bulk modulus,  $E_b$  (inverse slope of the compressibility curve) at  $p_o = 1$  atm is

$$\begin{aligned} E_b &= \frac{1}{D_b} \\ &= 1.025 \times 10^9 \text{ dyne/cm}^2 \\ &= 14,850 \text{ psi (LH}_2 \text{ at 20°K at 1 atm)} \end{aligned} \quad (6-8)$$

The bulk modulus, shown previously, was later used in correlation work on point-load test results, in conjunction with a corresponding value for liquid nitrogen (also from Reference 17):

$$E_b = 91,100 \text{ psi (LN}_2 \text{ at 77°K at 1 atm)}$$

---

\*Stepka has postulated a method for approximating Hugoniot's of cryogenic fluids and low-density materials for which no experimental high-pressure compressibility data exists (Reference 22). No attempt has yet been made to analyze the LH<sub>2</sub> panel fracture behavior reported in this document using Stepka's estimated LH<sub>2</sub> Hugoniot.

Thus, the correlation analysis, which used ratios of fluid bulk-modulus values as listed, pragmatically assumed that the geometric form of the compressibility curves would be similar at higher pressure levels. The compressibility characteristics must be better defined before precise values of shock strengths can be calculated.

### 6.3.2 Master Curve Correlation of Point-Load Impact Test Results

Because first examination of the basic test results indicated that the action of the  $\text{LH}_2$  shock-wave overpressure was an important factor influencing panel fracture behavior and that the shock could essentially be characterized as a function of projectile kinetic energy, it appeared appropriate to examine panel fracture behavior on an energy basis. First, the point-load test results were correlated with panel stress level and projectile energy, (Figures 6-25 through 6-28). The data appeared to correlate well (for each particular material and thickness) with energy, and a definite pattern of behavior was evident.

It was then postulated that a general relation could be derived to describe the behavior of all of the point-load panels tested. It was assumed that fracture behavior could be expressed as a function of projectile kinetic energy. Material strength,  $\sigma_u$ ; fracture toughness,  $K_c$ ; panel thickness,  $t_s$ ; a projectile characteristic dimension,  $R_o$ ; and compressibility of the contained fluid (bulk modulus,  $E_b$ , used to make the analysis tractable) each influence panel fracture behavior (Reference 2).

It was hypothesized that the data could be normalized to nondimensionalized form of a hoop-stress ratio (static conditions prior to impact),  $R_\sigma$ , and an impact-loading and material-strength parameter,  $R_I$ . The following definitions are made:

$$R_\sigma = \frac{\sigma_H}{\sigma_u} \quad (6-9)$$

$$R_I = f(t_s, R_o, K_c, E_b, \text{K.E.}) \quad (6-10)$$

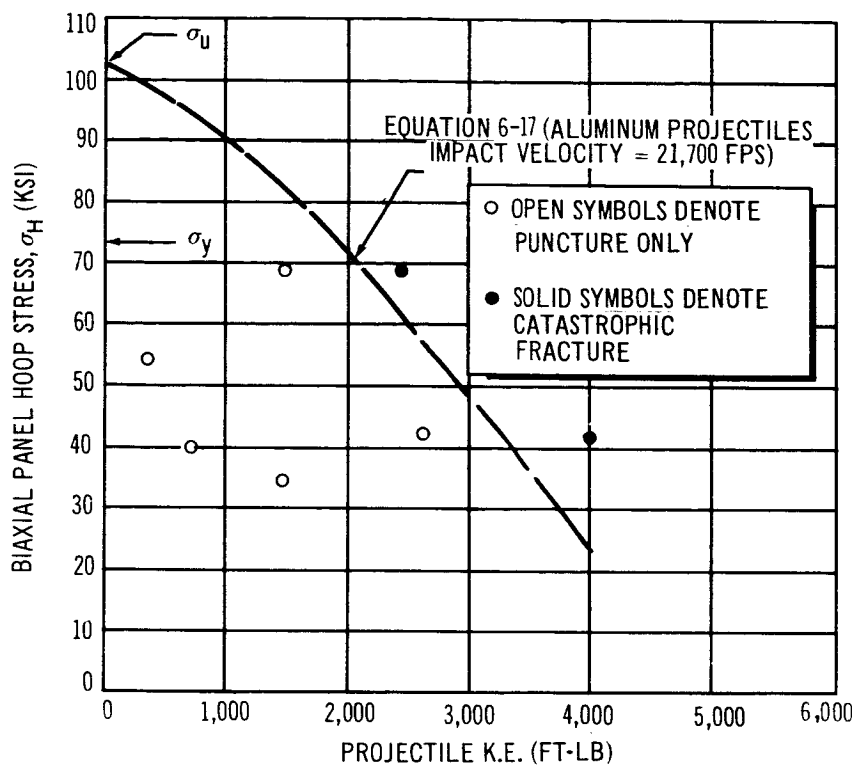


Figure 6-25. Correlation of Point-Load Test Results with Impact Energy (Behavior of 0.032-In.-Thick 2219-T87 Aluminum at LH<sub>2</sub> Temperature)

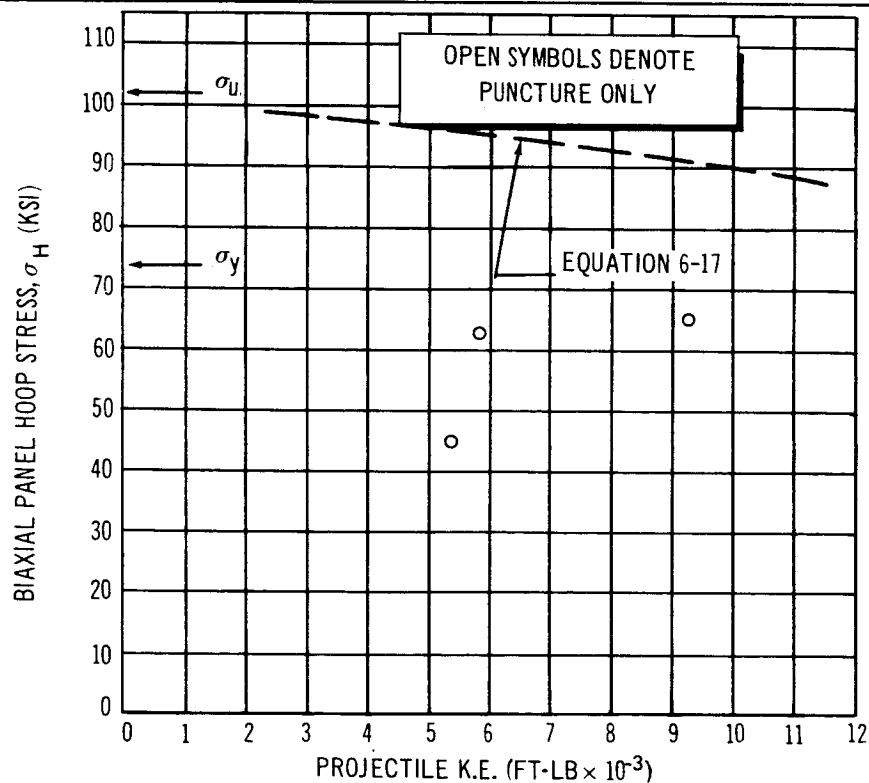


Figure 6-26. Correlation of Point-Load Test Results with Impact Energy (Behavior of 0.125-In.-Thick 2219-T87 Aluminum at LH<sub>2</sub> Temperature)



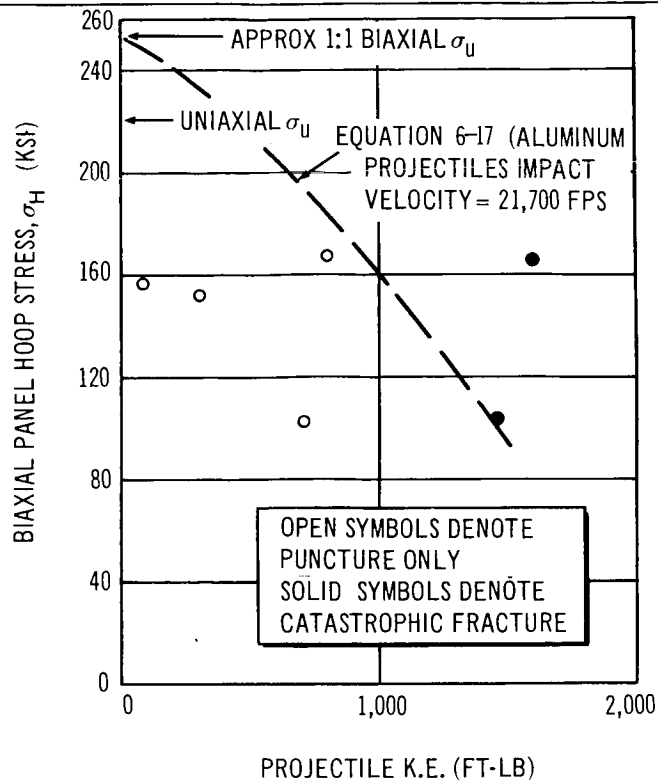


Figure 6-27. Correlation of Point-Load Test Results with Impact Energy (Behavior of 0.015-In.-Thick 5Al-2.5 Sn (ELI) Titanium at LH<sub>2</sub> Temperature)

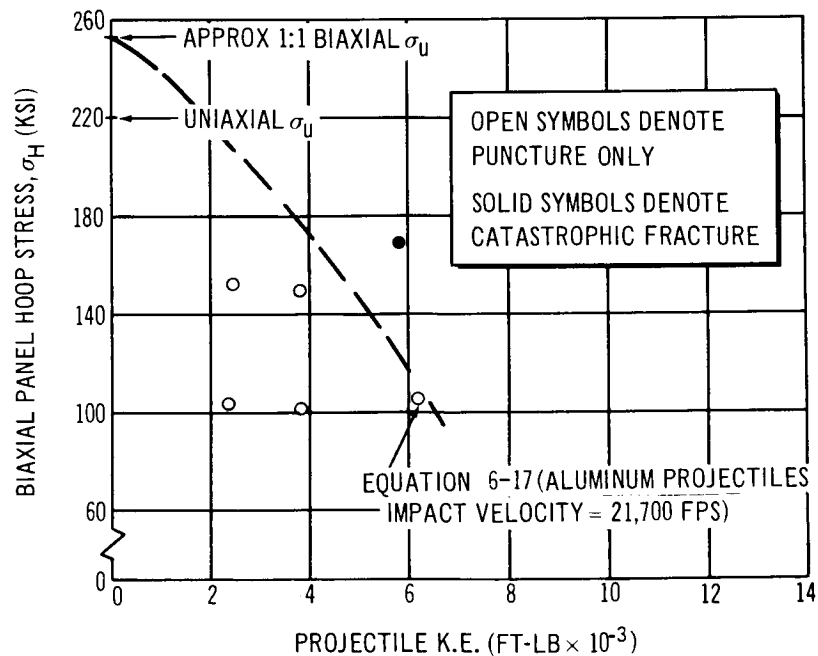


Figure 6-28. Correlation of Point-Load Test Results with Impact Energy ( Behavior of 0.036-In.-Thick 5Al-2.5 Sn (ELI) Titanium at LH<sub>2</sub> Temperature)

and

$$R_I = \frac{(E_b)^\alpha (R_o)^\theta (K.E.)^\xi}{(K_c)^\beta (t_s)^\gamma} \quad (6-11)$$

The maximum pressure generated behind a shock wave front as a function of shock velocity can be approximated by an equation of the form

$$p = k (U - c_o)^m \quad (6-12)$$

where

$k$  is a constant

$m$  is a nondimensional exponent

Examination of available compressibility data on various liquids indicates that  $m$  has an approximate value of 1.5 to 2.0 in the pertinent pressure range.

Combination of Equation 6-12 with Equation 6-3 yields a relation for maximum shock pressure as a function of projectile K.E. and time after impact,  $t$ .

$$p = k \left[ \frac{A (K.E.)^{1/3}}{t + t_o} \right]^m \quad (6-13)$$

If Equation 6-4 is correct for determining  $t_o$  as a function of projectile size,  $d$ , then  $t_o$  is also a function of projectile K.E., and Equation 6-13 becomes

$$p = k \left[ \frac{A(K.E.)^{1/3}}{t + f (K.E./V^2)^{1/3}} \right]^m \quad (6-14)$$

According to Equation 6-14, the pressure generated at the instant of impact ( $t = 0$ ) is independent of projectile K.E., but is a function of impact velocity to the  $2m/3$  power. As time increases, the denominator of the expression inside the brackets tends toward  $t$  plus a small number (in comparison to  $t$ ;  $t_o$  is of the order of a microsecond) and shock pressure becomes essentially a function of K.E. to the  $m/3$  power.

If the term  $t_0$  in Equation 6-13 does not depend upon projectile diameter (as suggested by the recent Lewis research discussed in paragraph 6.3.1), shock pressure is a function of K.E. to the  $m/3$  power throughout the wave propagation process.

Thus, it appears if  $t_0$  is either independent or dependent upon projectile size, the exponent for K.E. in Equation 6-11 is on the order of  $m/3$  at the instant of critical loading. A value of  $\xi = 0.5$  (corresponding to  $m = 1.5$ ) was chosen for data reduction; final results indicate this choice was satisfactory. Note that the correlation assumes that the critical loading is a function of maximum pressure at the shock front. The total stress in the panel wall--at the instant cracks are initiated at the edge of the impact puncture and begin to propagate--is a function not only of the peak pressure but also of the shape of the pressure pulse behind the front and the preceding load history. The complex dynamic load, stress wave, and high-rate-of-strain material strength effects are considered to be reducible to the nondimensional relations.

Comparison of the data obtained from the  $LN_2$  checkout shots with corresponding values obtained from  $LH_2$  shots indicated that  $R_I$  was perhaps a direct function of  $E_p$ , that is,  $\alpha = 1$ . This assumption was made on the basis of meager  $LN_2$  data; future correlations could easily indicate a different value.

Shock overpressure at some finite time after the puncture is fully formed in the panel (that is, after the direct cratering process is completed) loads the panel in some complex combination of hoop-membrane and plate-bending stresses. Hoop stress only would imply that  $\gamma = 1$ ; bending stress only would imply that  $\gamma = 2$ . Several trials were made at correlating data with values between 1 and 2. It appeared that hoop-membrane loadings were predominant and  $\gamma = 1$  was selected as the best estimate. The observed behavior of the thick-gage aluminum panels influenced the decision to select the low value for  $\gamma$ .

Unfortunately, it was not possible to launch projectiles with sufficient energy to produce catastrophic fracture in the 0.125-in.-thick aluminum panels. The highest energy data point for this panel configuration was plotted at a level significantly below the nondimensional critical impact-fracture boundary that

was determined by correlating data from tests of the thin-gage panels. The thick-gage aluminum panel that was struck by the high-energy projectile had a post-test appearance that indicated catastrophic fracture was perhaps impending. The plastically deformed zone adjacent to the hypervelocity puncture was compared with similar areas on the series of thin-gage aluminum panels that were tested below and above the critical loading conditions. Use of a value for  $\gamma$  greater than 1 would move the thick-gage aluminum panel data points farther away from the impact-fracture master curve.

Values of  $\beta$  and  $\theta$  were then calculated from Equation 6-11.  $R_I$  is nondimensional if

$$\begin{aligned}\alpha + \xi &= \beta \\ -2\alpha + \xi + \theta &= -(1.5)\beta + \gamma\end{aligned}\tag{6-15}$$

and a consistent set of units are used. Substitution of values of  $\alpha = 1$ ,  $\xi = 0.5$  and  $\gamma = 1$  yields values of  $\beta = 1.5$  and  $\theta = 0.25$ . Results of correlation of all of the point-load data (points near the fracture boundary), using the noted exponents with Equation 6-9 and 6-11 are shown in Figure 6-29.

It is now postulated that the dynamic fracture boundary can be described by the equation

$$R_\sigma = 1 - B (R_I)^n\tag{6-16}$$

Correlation to test data of Figure 6-29

$$\begin{aligned}B &= 0.180 \\ n &= 2.25 \\ R_\sigma &= 1 - 0.180 (R_I)^{2.25}\end{aligned}\tag{6-17}$$

and the relation is closely bracketed by the 0.032-in. -thick aluminum and the 0.015- and 0.036-in. -thick titanium data points.

It is recommended that the equations not be used at stress levels higher than approximately 70% of the ultimate strength of the material, the upper limit of the current test data. A practical procedure would be to cut the top of the equation off with the fatigue preflaw burst test fracture envelope.

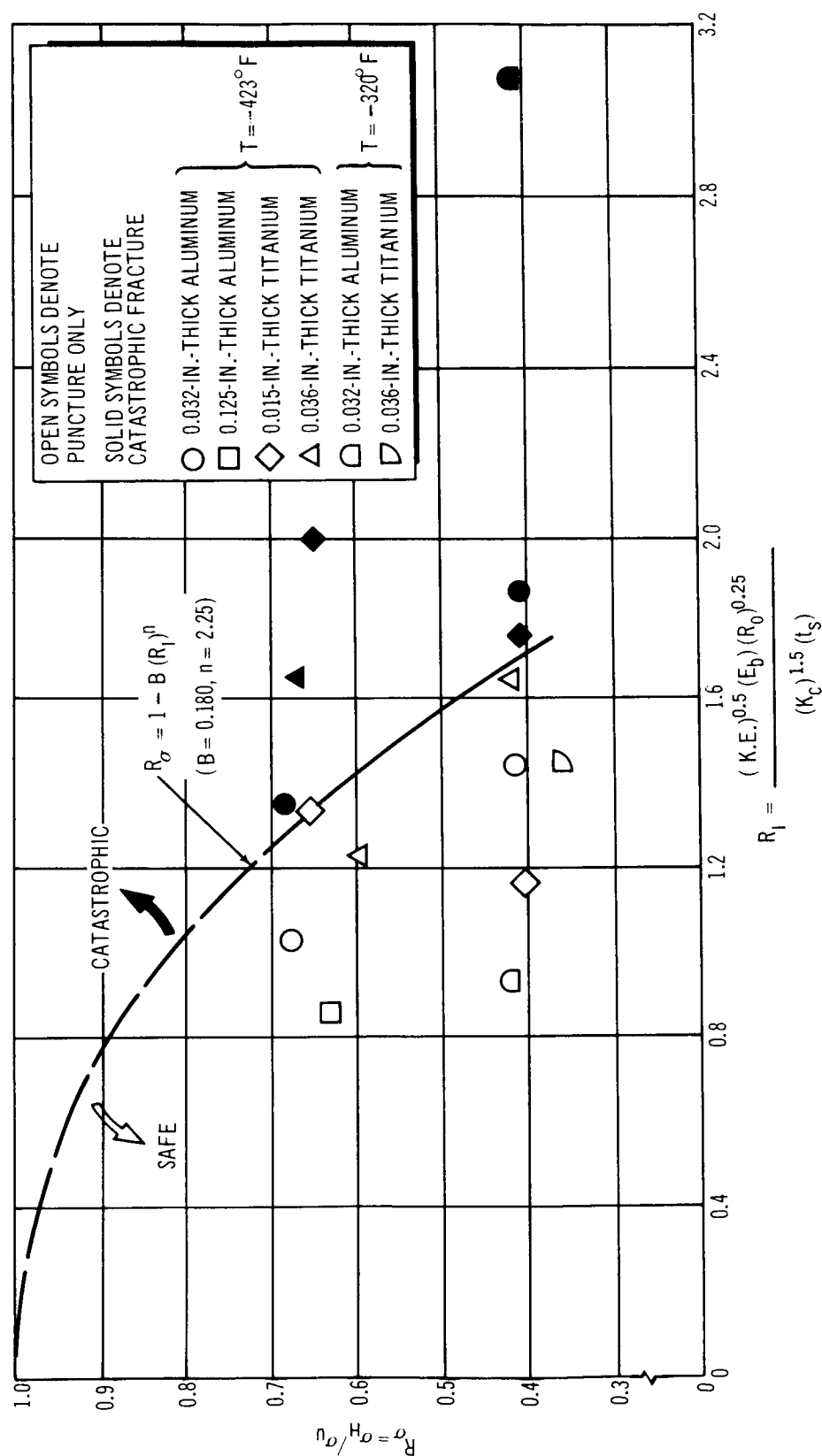


Figure 6-29. Master Curve -- Results of Biaxial Panel Point Load Tests (Behavior of 2219-T87 Aluminum and 5Al-2.5Sn (ELI) Titanium at LH<sub>2</sub> and LN<sub>2</sub> Temperatures)

One final note of caution. Values of  $K_c = 97 \text{ KSI } \sqrt{\text{in.}}$  for the aluminum and  $118 \text{ KSI } \sqrt{\text{in.}}$  for the titanium alloys were used in this section to reduce data. The fracture toughness value for the 2219-T87 aluminum was taken directly from Table 5-1. The fracture toughness of the 5Al-2.5Sn titanium was taken at  $118 \text{ KSI } \sqrt{\text{in.}}$  which is 15% less than the  $136 \text{ KSI } \sqrt{\text{in.}}$  shown by Table 5-1 for fatigue type preflaws. This reduction was made since it was estimated that the crack gage instrumentation overestimated critical flaw size,  $2a$ , by a factor of significant magnitude. The parameter  $R_I$  is sensitive to the value used for  $K_c$ ;  $K_c$  obtained by uniaxial tests on titanium panels showed significant scatter and varied with the type of preflaw. Therefore, one should be conservative when selecting  $K_c$  for use in the master curve equation. The uniaxial fatigue  $K_c$ 's were used as the basic research objective which is to develop general relations that describe complex hypervelocity impact behavior but use material properties which are either already available or can be determined using standard test procedures.

## Section 7

### HYPERVELOCITY IMPACT DISTRIBUTED-LOAD TESTS

Distributed-load impact test configurations consisted of simple sheet metal bumpers that were spaced various distances in front of the biaxial panels. No fillers were inserted in the space between the bumpers and the panels. The test plan was designed to complement a preceding meteoroid shield research program conducted by J. F. Lundeberg, et al. (Reference 15), and concurrent meteoroid-bumper interaction studies conducted by the Space Research Institute of McGill University (NASA Contract No. NAS 3-4190). Two basic projectile-bumper configurations were investigated; one group of tests was made with aluminum projectiles shot into aluminum bumpers, and a series of Lexan projectile-lead bumper impact tests was made.

#### 7.1 METEOROID SHIELD TEST PROGRAM

A meteoroid shield program was arranged to provide design information on the behavior of stressed biaxial panels which were protected by the following meteoroid bumper or shield configurations:

1. Bumper, 0.032-in. -thick aluminum, spaced 3 in. and 6 in. from the panels.
2. Bumper, 0.020-in. -thick lead sheet, spaced 3 in. and 6 in. from the panels.
3. Panel membrane stress (nominal),  $0.9 \sigma_y$  and  $0.6 \sigma_y$  for aluminum panels;  $\sigma_u/1.4$  and  $67\% (\sigma_u/1.4)$  used for titanium panels.

A complete outline of the test plan and detail results are shown by Tables D-IV and D-V of Appendix D.

The 0.032-in. -thick bumpers (and associated spacings) were chosen as representative of a typical spacecraft sheet metal outer structure that would enclose a  $\text{LH}_2$  tank. The aluminum projectiles simulate the density of stony type meteoroids for impacts at the low end of the meteoroid velocity range, which is 11 km/sec (36,000 fps) minimum. It is thought that the aluminum-

projectile, aluminum-bumper results are conservative (at a certain impact K. E. level) when extrapolated to higher velocities, because the debris spray will tend to break up into smaller individual particles as impact velocity increases. Some of the theoreticians believe that meteoroids (and portions of the bumper) will be completely vaporized during the projectile-bumper interaction process at actual meteoroid velocities.

An impact of a Lexan projectile against a thin lead shield can produce a finely dispersed debris cloud. This testing may closely simulate the impact at meteoroid velocity of a stony type meteoroid against a shield constructed of one of the standard structural materials. Such tests may also simulate the lower density meteoroids (cometary type) for impacts that occur throughout the complete meteoroid velocity range (11 to 72 km/sec). Therefore, it was decided to include a series of Lexan projectile against lead (Pb) bumper impact tests in the distributed-load test program.

The distributed-load tests were conducted using the same general techniques that were developed during the point-load effort. Placement of the shields at the proper position in front of the main target required special testing techniques. Because panel contour measurements had to be taken, using the remote control spherometer during each test, the shield could only be inserted in position after the spherometer was retracted. Figure 7-1 shows the method used to handle the bumper during the distributed-load tests.

A guard plate had been placed on the front of the fixture prior to the point-load tests to protect the spherometer. Guides for suspension lines for the shield were placed on the guard plate to ensure proper bumper spacing. The bumper was held by two thin wires that ran from the bumper upper corners, through the guides, to the spherometer retracting cable (Figure 7-1). After the fixture was filled with  $\text{LH}_2$ , and the  $-423^\circ\text{F}$  panel shape, contour measurements were taken, the spherometer was retracted, and the bumper was automatically lifted to the proper test position. Figure 7-1 also shows the helium purge tent that was placed on the front of the biaxial test fixture. All of the apparatus in this figure is actually inside the tent; the photograph was taken through the polyethylene tent material.



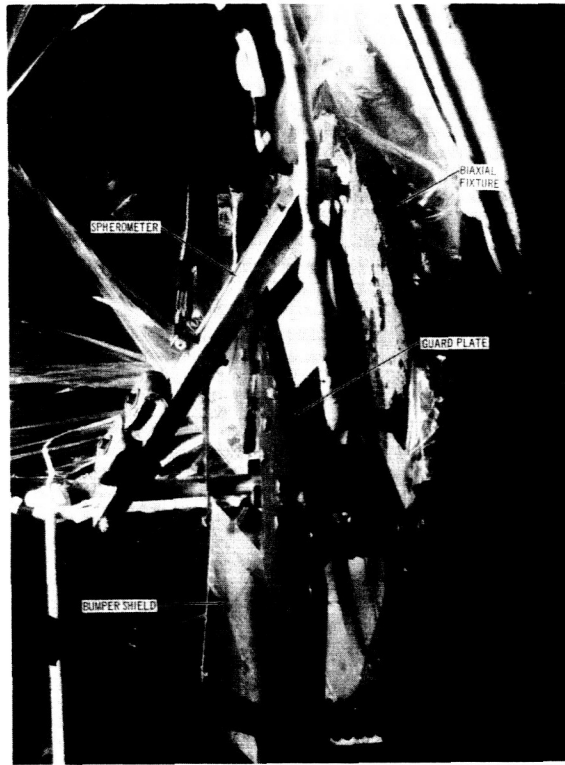


Figure 7-1. Fixture Setup for Distributed-Load Tests

## 7.2 BASIC TEST RESULTS

Table D-V of Appendix D gives detail results of the distributed-load test results. The basic results of the tests are also shown in Figures 7-2 and 7-3. Three effects are immediately apparent: (1) an increase of shield spacing,  $S_s$ , from 3 to 6 in. increases the efficiency of the shield in relation to the catastrophic-fracture failure mode; (2) catastrophic fracture can occur at significantly lower impact energy levels for a bumper shot than that for a point-load test when aluminum projectiles are used (target panels of the same gage under equivalent prestress loadings); and (3) the surface damage produced by a Lexan projectile -- lead-bumper debris cloud -- is much less severe than that produced by an aluminum projectile -- aluminum-bumper debris spray (Figure 7-4). The aluminum projectile situation then results in catastrophic fracture of the main target panel for a much lower projectile energy input than that associated with a Lexan projectile test.

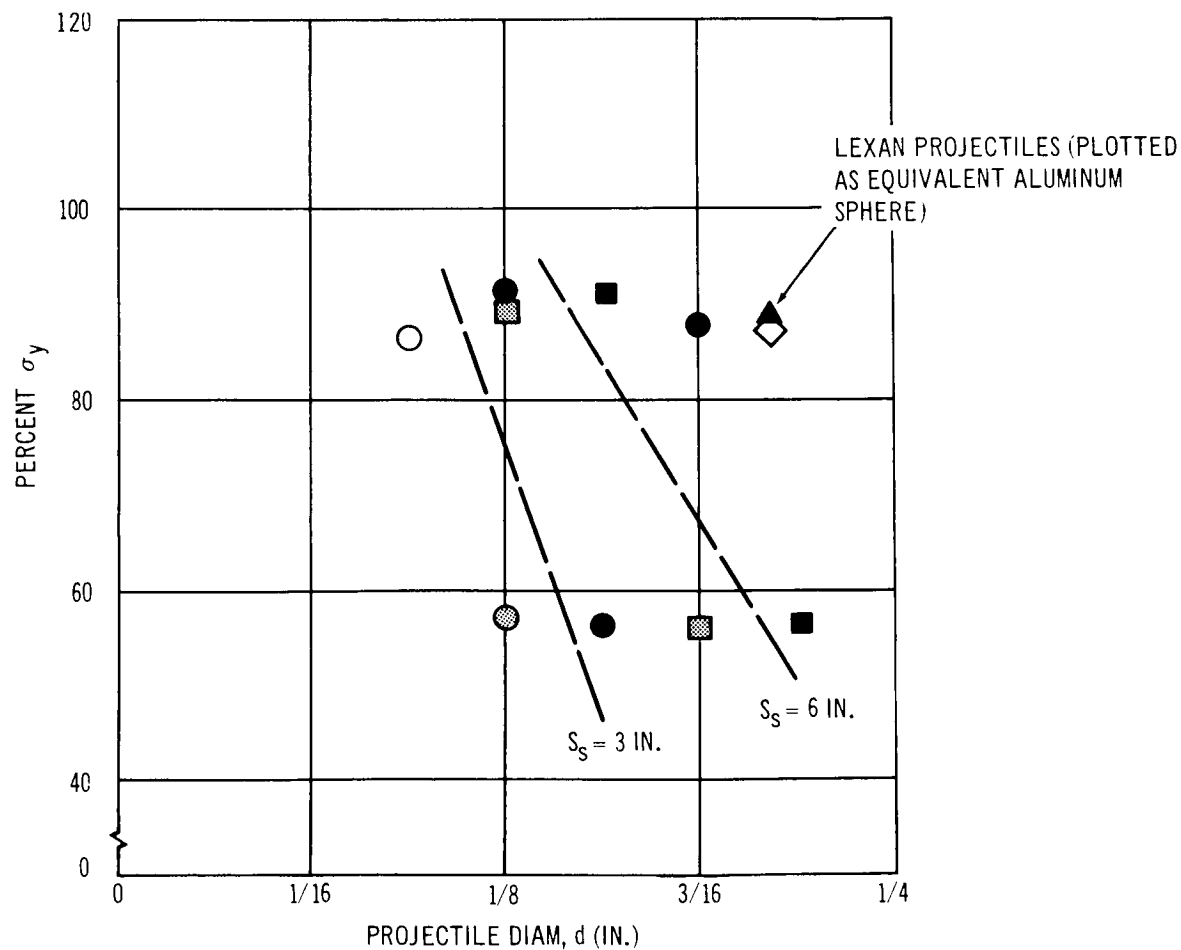
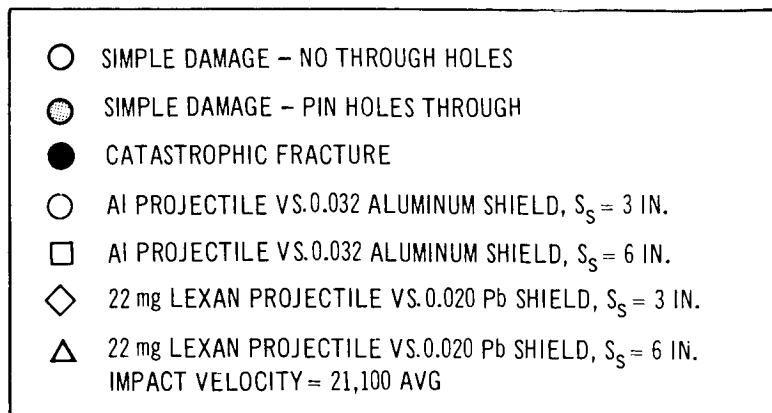


Figure 7-2. Results of Biaxial Panel Distributed-Load Tests (Behavior of 0.032-In.-Thick 2219-T87 Aluminum at LH<sub>2</sub> Temperature)

- SIMPLE DAMAGE – NO THROUGH HOLES
  - SIMPLE DAMAGE – PIN HOLES THROUGH
  - CATASTROPHIC FRACTURE
  - AI PROJECTILE VS. 0.032 ALUMINUM SHIELD,  $S_s = 3$  IN.
  - AI PROJECTILE VS. 0.032 ALUMINUM SHIELD,  $S_s = 6$  IN.
  - △ 22 mg LEXAN PROJECTILE VS. 0.020 Pb SHIELD,  $S_s = 3$  IN.
  - ◇ 22 mg LEXAN PROJECTILE VS. 0.020 Pb SHIELD,  $S_s = 6$  IN.
  - ◻ 22 mg LEXAN PROJECTILE VS. 0.010 Pb SHIELD,  $S_s = 6$  IN.
- IMPACT VELOCITY = 22,000 FPS AVG

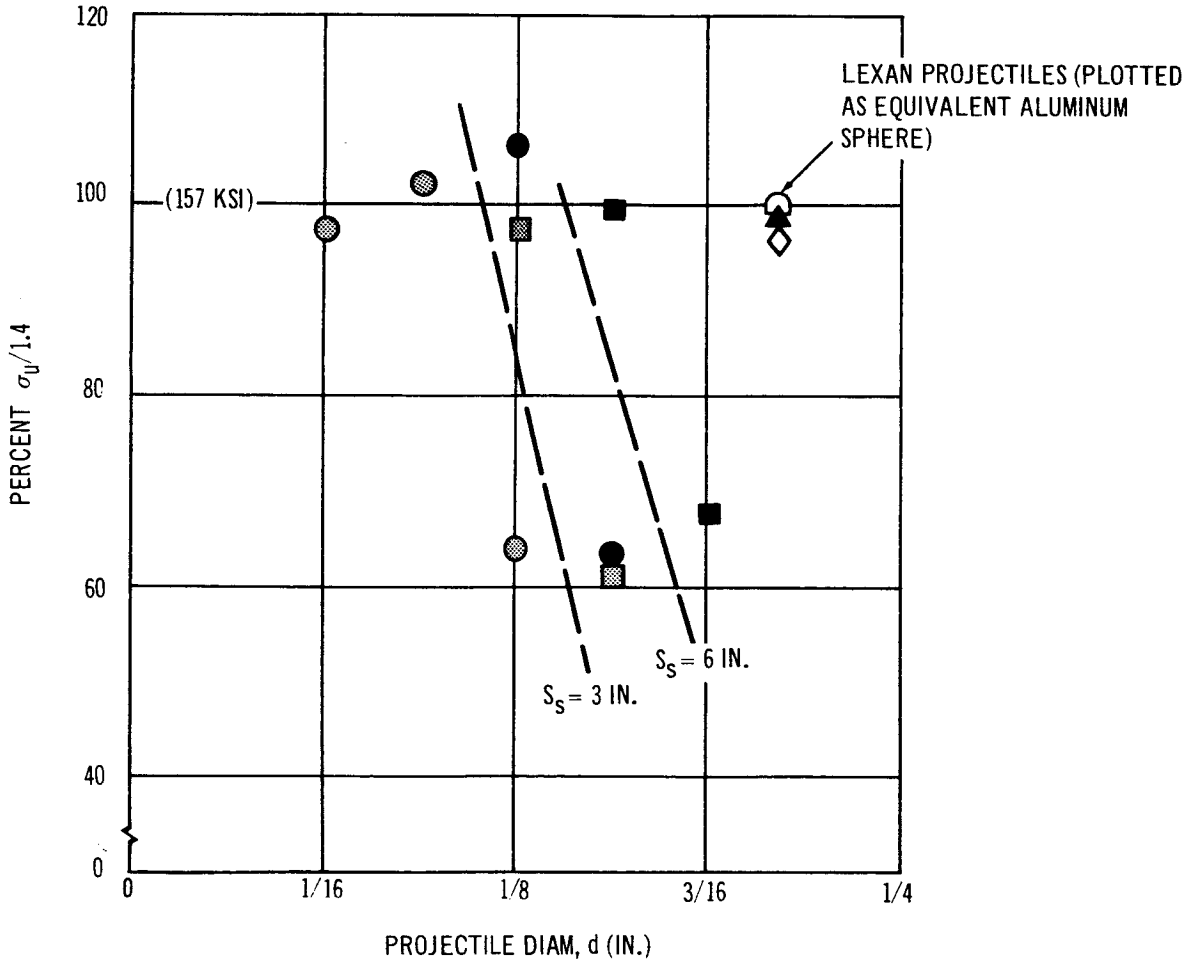
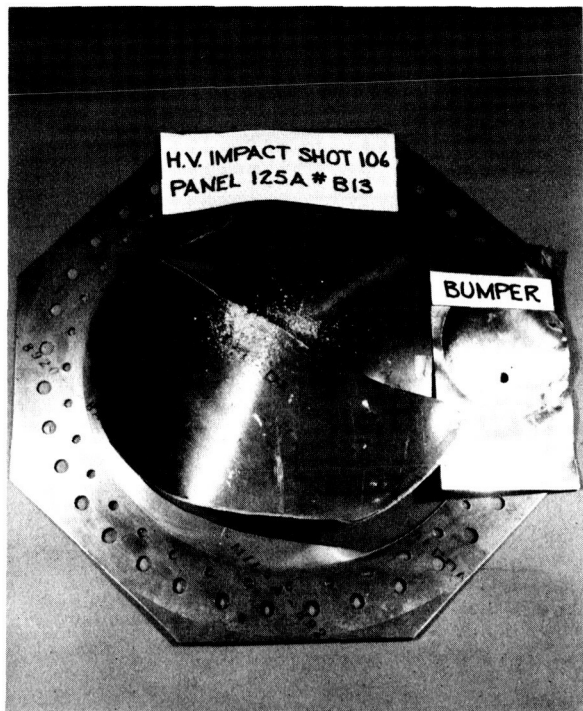
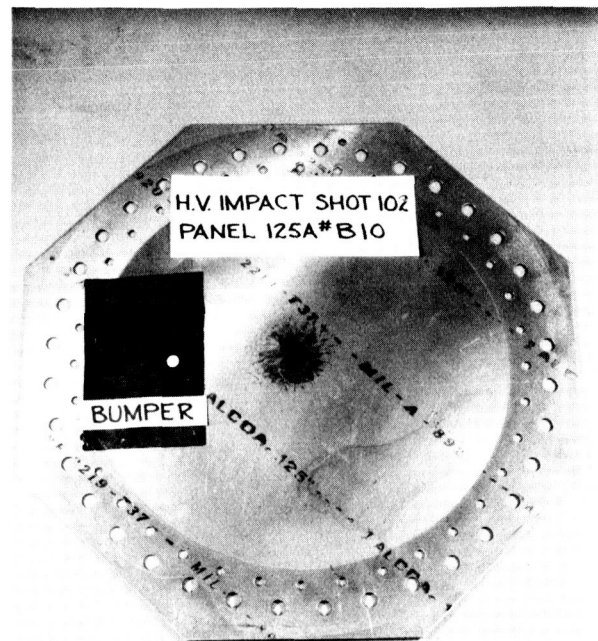


Figure 7-3. Results of Biaxial Panel Distributed-Load Tests (Behavior of 0.015-In.-Thick 5Al-2.5 Sn (ELI) Titanium at LH<sub>2</sub> Temperature)



ALUMINUM BUMPER TEST, 0.250-IN.-DIAM ALUMINUM  
PROJECTILE, IMPACT K.E. = 5,020 FT-LB



LEAD BUMPER TEST, 0.350-IN. DIAM  
LEXAN PROJECTILE, IMPACT K.E. = 9,600 FT-LB

Figure 7-4. Typical Distributed-Load Test Results

### 7.3 CORRELATION OF TEST RESULTS WITH IMPACT ENERGY AND SHIELD SPACING

The basic distributed-load test data were correlated with impact energy and shield spacing in much the same manner the point-load data were treated (Figures 7-5 through 7-8). Some point-load data are actually shown as base-line points on the figures. The assumption here is that point-load test results are equivalent to the case where the bumper spacing,  $S_s$  (and, in effect, also the bumper), equals zero. The figures thereby illustrate in graphic detail that a bumpered target can indeed fracture catastrophically under lower energy input conditions than that of point-load impact. The reason is evident; aluminum projectile and bumper debris produced a large preflaw in many of the tests, and the static fracture strength of the material is thereby reduced. The impact energy differential at a given panel stress and shield spacing between the aluminum-aluminum and the Lexan-lead fracture boundaries, as shown in the figures, must be controlled dominantly by material fracture strength behavior under dynamic loading conditions.

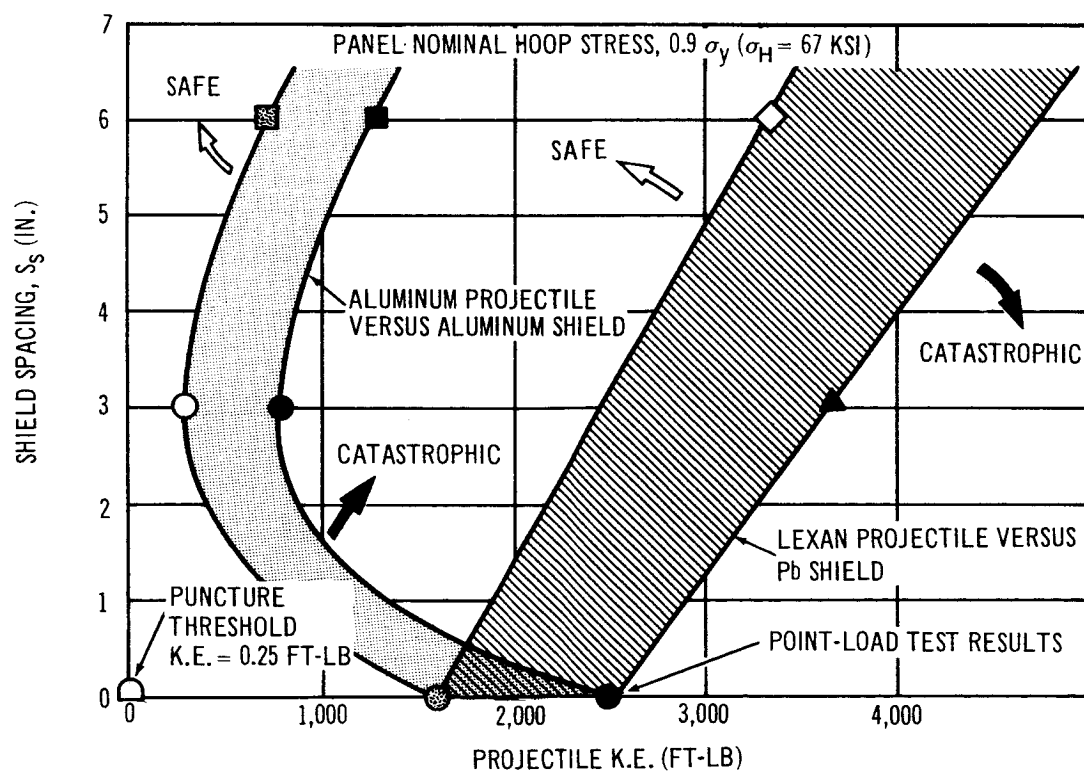
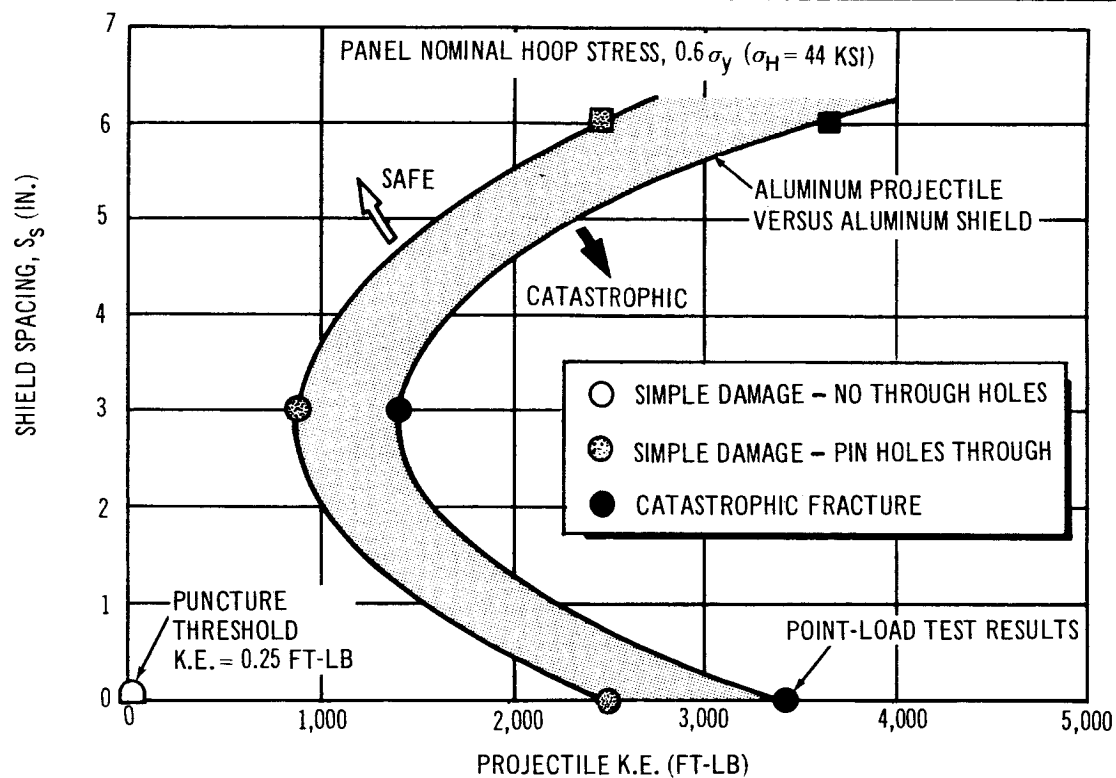


Figure 7-5 Correlation of Distributed-Load (Meteoroid Shield) Test Results with Impact Energy and Shield Spacing (Behavior of 0.032-In.-Thick 2219-T87 Aluminum at  $LH_2$  Temperature)

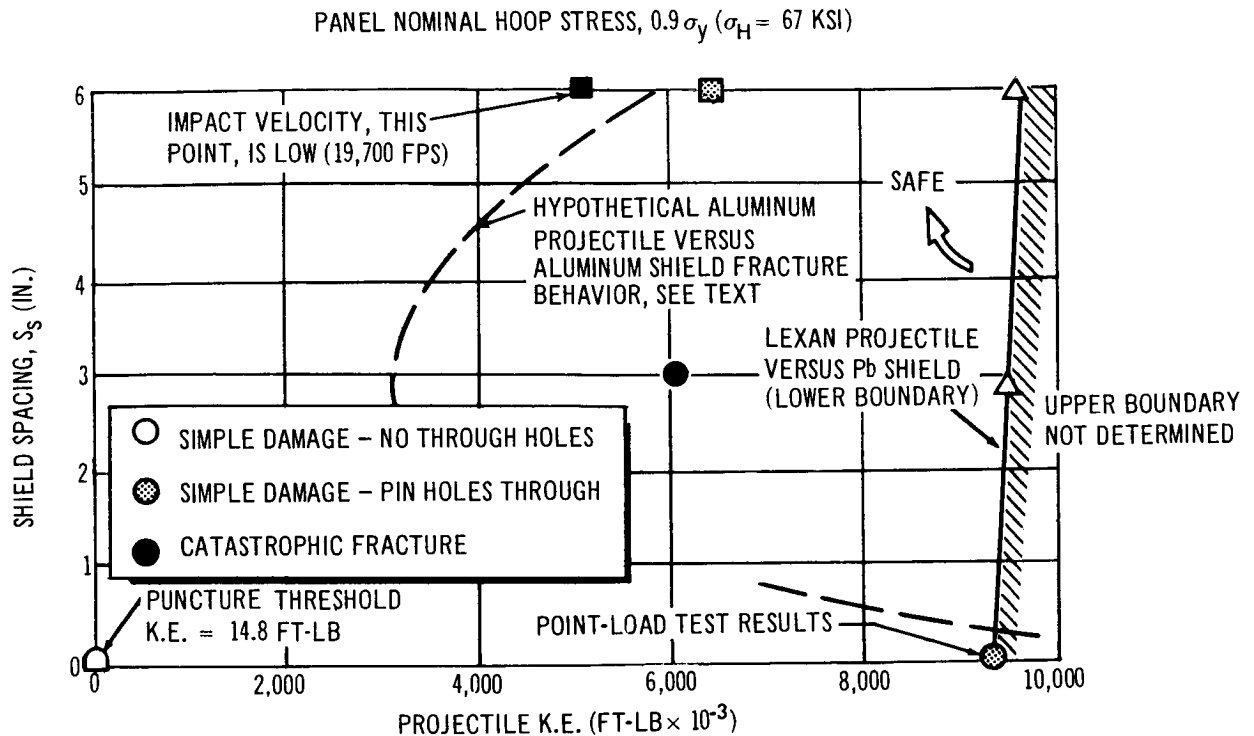


Figure 7-6. Correlation of Distributed-Load (Meteoroid Shield) Test Results with Impact Energy and Shield Spacing (Behavior of 0.125-In.-Thick 2219-T87 Aluminum at LH<sub>2</sub> Temperature)

Results of tests using Lexan projectiles and lead bumpers indicate there are significant increases in panel fracture strengths for these test conditions over those resulting from point-load impact. If the premise that Lexan-lead projectile-bumper tests, conducted at relatively low velocity, simulate meteoroid impact against typical spacecraft structure bumpers (such as thin aluminum sheets) at much higher velocities is true, bumper configurations are efficient as devices to prevent both puncture and catastrophic fracture of pressure-stressed tank-shells.

Tests conducted with projectiles launched in the 20,000 fps range do not provide sufficient data to fully resolve the bumper design problem. In this research, two different projectile-bumper configurations were selected to be tested. Results obtained from each set of tests are radically different. Various research workers studying hypervelocity impact have different opinions as to which test best simulates a meteoroid strike against a bumper-protected structure. The question has considerable import because many

spacecraft design studies have been made which assume (based on numerous tests of spaced, but unstressed, sheet panels) that bumper configurations are more efficient than unprotected vehicle hulls.

Another phenomenon relating to the efficiency of meteoroid bumpers is indicated in Figures 7-5 through 7-8. For the test points plotted as "safe" point-load results, holes were punched in the panels. Puncture sizes ranged from about 1/8-in. diam to almost 1-in. diam. If the puncture were not repaired, the tank would leak. Calculations to determine the threshold of puncture of the panels tested were made. The data of Reference 16 indicate that, for aluminum spheres impacting finite-thickness 2024-T3 aluminum targets at 7.4 km/sec, the thickness required to prevent perforation is approximately 4 times the projectile diameter. The aluminum projectile K. E. value corresponding to threshold puncture of each panel configuration was calculated; corrections were made using Summers' penetration equation (Reference 17) to estimate the behavior of the titanium panels. The K. E. values for threshold perforation are extremely low when compared with projectile K. E. values that produce the catastrophic-fracture mode of failure. If the criterion for design is that no leaks may result from a meteoroid strike, both bumper configurations that were investigated will increase the efficiency of the structure.

The fracture boundaries are reasonably well established for the thin-gage aluminum panels for the projectile-bumper configurations tested. For the thick-gage aluminum, the data are sufficient only to indicate trends. The hypothetical aluminum-projectile, aluminum-bumper fracture curve of Figure 7-6 is estimated as a simple ratio of the thin-gage aluminum behavior (with point-load data providing the anchor-point and basic panel strength increase factors). Lexan projectiles only were used during the tests of thick-gage titanium panels.

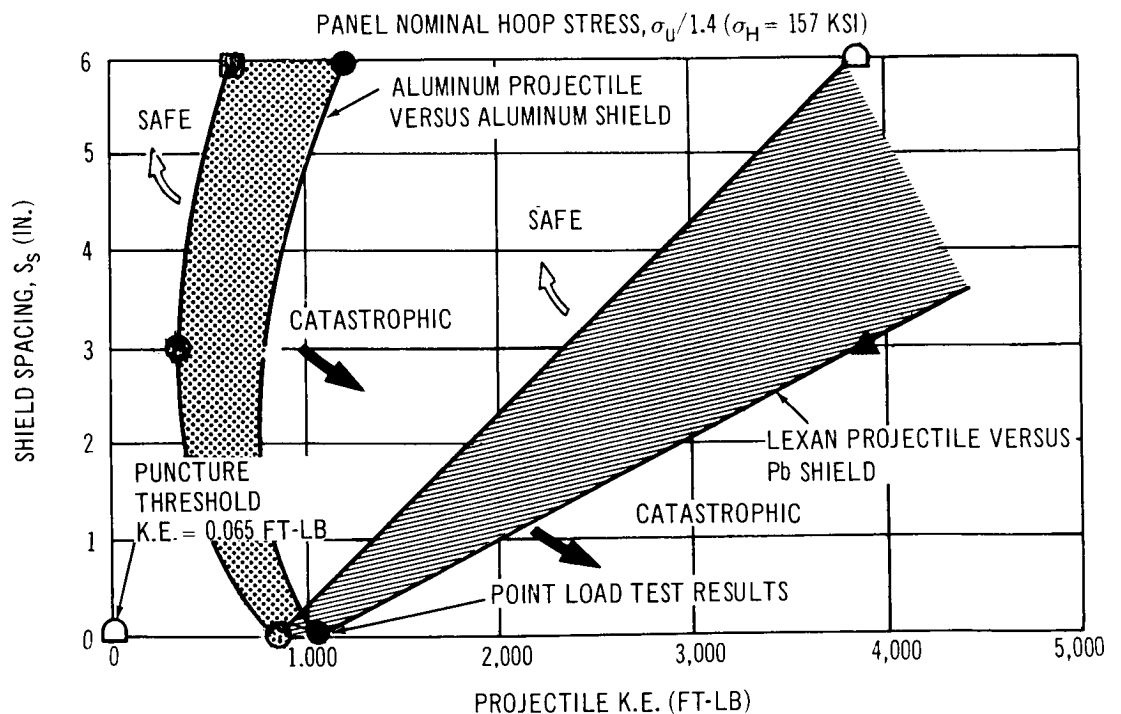
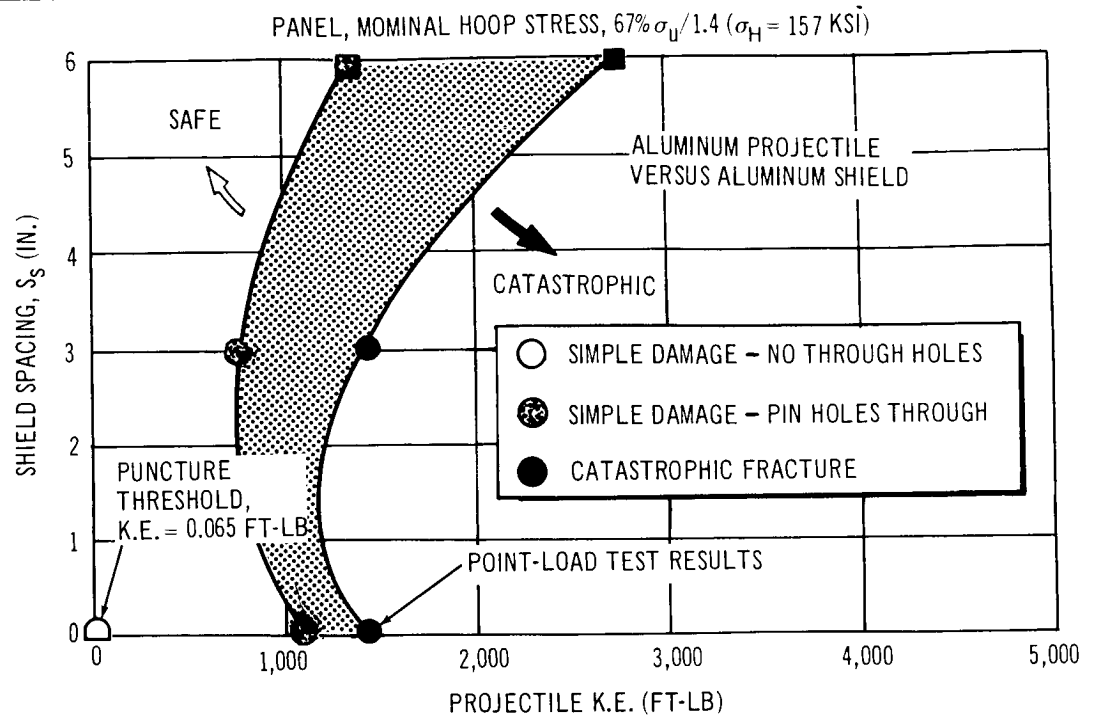


Figure 7-7. Correlation of Distributed-Load (Meteoroid Shield) Test Results with Impact Energy and Shield Spacing (Behavior of 0.015-In.-Thick 5 Al-2.5 Sn (ELI) Titanium at  $\text{LH}_2$  Temperature)



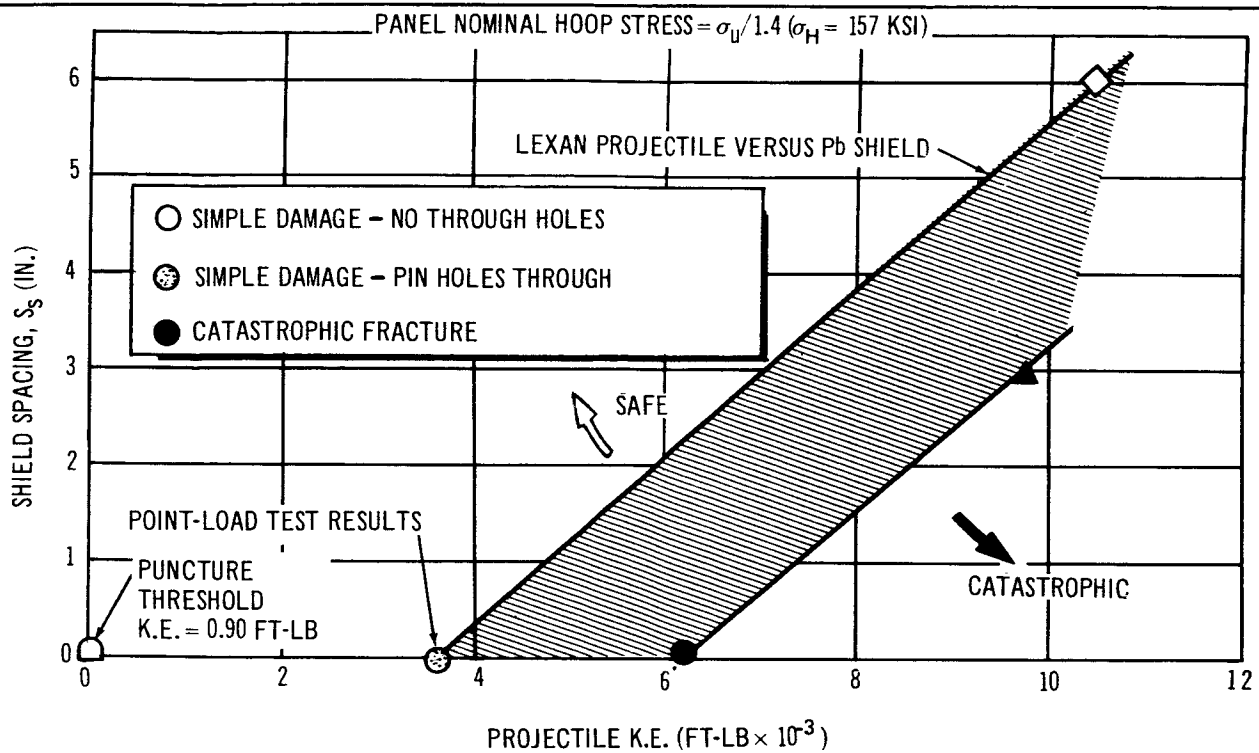


Figure 7-8. Correlation of Distributed-Load (Meteoroid Shield) Test Results with Impact Energy and Shield Spacing (Behavior of 0.036-In.-Thick 5Al-2.5 Sn (ELI) Titanium at LH<sub>2</sub> Temperature)

## Section 8

### CONCLUSIONS

Some of the more important conclusions and observations resulting from the research detailed in this report are briefly restated below. These conclusions are discussed in greater detail in the body of the report.

1. The aluminum and titanium alloys investigated appear to be suitable materials for use as structural walls of cryogenic tankage within the context of a hypervelocity impact environment. Both materials are tolerant to small flaws made by hypervelocity punctures with test temperatures as low as  $-423^{\circ}\text{F}$ . The presented data can be used to make meteoroid hazard analyses of the structures investigated during this research program.
2. The uniaxial strength of flawed panels can be used with reasonable accuracy for design purposes to predict the behavior of panels subjected to biaxial straining.
3. The experiment data demonstrates that safe working stresses can be evaluated for pressure vessels subjected to hypervelocity impact. However, a relatively narrow margin exists between the extremes of safety and catastrophic rupture.
4. A fracture toughness parameter for the materials investigated is useful in the analytical correlation of the experiment data but cannot be solely used to establish safe pressure-vessel working stresses. Dynamic hypervelocity-impact, fracture-strength characteristics are significantly lower than the static fracture strength characteristics of fatigue preflawed biaxial panels.
5. The quasi-composite panels (i. e., panels with a layer of condensate frozen on the front) fractured at much lower impact energy levels (for a given panel hoop-stress level) than those that produced catastrophic fracture of an unprotected panel.
6. Fluid shock overpressure is a dominant factor influencing panel fracture behavior in point-load tests. Differences in  $\text{LN}_2$  and  $\text{LH}_2$  test results indicate that dynamic fracture strengths can be directly related to the compressibility of the contained fluid.

7. The LH<sub>2</sub> shock wave was characterized by the Chou method (Reference 3). This method appears to be sufficiently accurate for use as a component part of the data correlation approach as presented by this document. Possible limitations of the shock equation are explained in detail in Section 6.
8. It is possible to describe the results of all of the point-load tests conducted during this investigation by a normalized master curve relation.
9. A bumpered target can fracture catastrophically under lower energy input conditions than those of point-load impact when aluminum projectiles and aluminum bumpers are used. This reduction in strength was not observed when Lexan projectiles were fired against lead bumpers. These observations are limited to the low 20,000-fps impact-velocity range.

Appendix A  
PROCESSING HISTORY AND CHEMICAL COMPOSITION OF  
TEST PANEL RAW MATERIALS

Table A-I  
PROCESSING HISTORY AND CHEMICAL COMPOSITION OF  
TEST PANEL RAW MATERIALS

Material	2219 Al	5Al-2.5Sn (ELI) Ti
Temper	T87	Annealed
Specification	MIL-A-8920	TMCA Internal
Thickness (in.)	0.032 0.125	0.015 0.036
Supplier	Alcoa	TMCA
Heat No.	---	D-5907

Chem Comp (%)	(Spec)	(Douglas Check)	(TMCA)
Al	Bal	Bal	5.2
C	--	--	0.025
Cu	5.8-6.8	6.25	--
Fe	0.30 Max.	0.27	0.16
H	--	--	0.006-0.015
Mn	0.20-0.40	0.27	--
Mg	0.02 Max.	0.02	--
N	--	--	0.014
O	--	--	0.07
Si	0.20 Max.	--	--
Sn	--	--	2.5
Ti	0.02-0.10	0.07	Bal
V	0.05-0.15	--	--
Zn	0.10 Max.	0.05	--
Zr	0.10-0.25	--	--

Appendix B  
MECHANICAL PROPERTIES OF TEST  
PANEL MATERIALS

Mechanical properties of the test panel materials as supplied by the material vendors (room temperature) and as determined by Douglas tests (at room temperature and at  $\text{LH}_2$  temperature,  $-423^\circ\text{F}$ ) are tabulated in this appendix. A comparison of the Douglas test values with previously reported values is shown by Figures B-1 and B-2.

Table B-1

ROOM TEMPERATURE MECHANICAL PROPERTIES OF  
TEST PANEL SHEET MATERIALS (VENDOR DATA)

Vendor	Code	Material	UTS (KSI)	YS (KSI)	Elongation (% in. 2 in.)
Alcoa	632-293	0.032-in. -thick 2219-T87 aluminum alloy	72.0 max. 71.5 min.	48.9 max. 48.8 min.	10.0
Alcoa	632-291	0.125-in. -thick 2219-T87 aluminum alloy	67.9 max. 67.3 min.	55.6 max. 55.0 min.	10.0
TMCA	C-9239 C-9902 F-0658	0.015-in. -thick 5Al-2.5Sn (ELI) titanium alloy	128.2 max. 117.5 min.	118.1 max. 112.9 min.	18.0 max. 13.5 min.
TMCA	C-9250	0.036-in. -thick 5Al-2.5Sn (ELI) titanium alloy	120.7 max. 115.9 min.	111.3 max. 107.8 min.	19.0 max. 11.5 min.

Table B-II (page 1 of 2)

ROOM TEMPERATURE (70° F) MECHANICAL PROPERTIES  
OF TEST PANEL SHEET MATERIALS (DOUGLAS TESTS)

Tensile Specimen No.	Code	Material	Direction	UTS (KSI)	YS (KSI)	Elongation (% in 2 in.)
1	0.032A-1L	0.032-in.-thick 2219-T87	Longitudinal	70.0	58.8	8
2	0.032A-2L			70.3	59.1	8
3	0.032A-3L			71.0	59.9	8
4	0.032A-1T	aluminum alloy	Transverse	71.9	61.2	8
5	0.032A-2T			71.0	58.7	8
6	0.032A-3T			72.3	59.5	8
	Average (longitudinal specimens)			70.4	59.3	8
	Average (transverse specimens)			71.7	59.8	8
7	0.125A-1L	0.125-in.-thick 2219-T87	Longitudinal	68.9	58.0	11
8	0.125A-2L			68.5	57.2	10
9	0.125A-3L			68.7	57.5	10
10	0.125A-1T	aluminum alloy	Transverse	70.4	58.3	9
11	0.125A-2T			70.3	58.1	10
12	0.125A-3T			70.2	58.1	10
	Average (longitudinal specimens)			68.7	57.6	10
	Average (transverse specimens)			70.3	58.2	10

Table B-II (page 2 of 2)

Tensile Specimen No.	Code	Material	Direction	UTS (KSI)	YS (KSI)	Elongation (% in 2 in.)
13	0.015T-1L	0.015-in. -thick 5Al-2.5Sn (ELI) titanium alloy	Longitudinal	118.1	109.8	15
14	0.015T-2L			116.4	109.3	14
15	0.015T-3L			117.5	110.5	16
16	0.015T-1T	0.036-in. -thick 5Al-2.5Sn (ELI) titanium alloy	Transverse	114.7	109.7	16
17	0.015T-2T			116.9	111.5	17
18	0.015T-3T			118.4	112.2	17
	Average (longitudinal specimens)			117.3	109.9	15
	Average (transverse specimens)			116.7	111.1	17
19	0.036T-1L	0.036-in. -thick 5Al-2.5Sn (ELI) titanium alloy	Longitudinal	118.2	109.7	12
20	0.036T-2L			117.5	108.9	14
21	0.036T-3L			113.5	106.2	16
22	0.036T-1T	0.036-in. -thick 5Al-2.5Sn (ELI) titanium alloy	Transverse	115.7	109.3	15
23	0.036T-2T			115.5	108.9	15
24	0.036T-3T			112.9	106.7	16
	Average (longitudinal specimens)			116.4	108.3	14
	Average (transverse specimens)			114.7	108.3	15



Table B-III (page 1 of 2)  
 LH<sub>2</sub> TEMPERATURE (-423°F) MECHANICAL PROPERTIES OF  
 TEST PANEL SHEET MATERIALS (DOUGLAS TESTS)

Tensile Specimen No.	Code	Material	Direction	UTS (KSI)	YS (KSI)	Elongation (% in 2 in.)
25	0.032A-4L	0.032-in. -thick 2219-T87	Longitudinal	102.3	76.0	16
26	0.032A-5L			101.5	73.4	16
27	0.032A-6L			101.8	75.9	16
28	0.032A-4T	aluminum alloy	Transverse	102.1	74.8	16
29	0.032A-5T			101.8	73.2	15
30	0.032A-6T			99.1	75.3	13
	Average (longitudinal specimens)			101.9	75.1	16
	Average (transverse specimens)			101.0	74.4	15
31	0.125A-4L	0.125-in. -thick 2219-T87	Longitudinal	98.7	73.2	18
32	0.125A-5L			98.6	73.9	18
33	0.125A-6L			98.7	74.8	17
34	0.125A-4T	aluminum alloy	Transverse	103.2	76.9	14
35	0.125A-5T			102.4	75.5	14
36	0.125A-6T			102.7	76.2	14
	Average (longitudinal specimens)			98.7	74.0	18
	Average (transverse specimens)			102.8	76.2	14

Table B-III (page 2 of 2)

Tensile Specimen No.	Code	Material	Direction	UTS (KSI)	YS (KSI)	Elongation (% in 2 in.)
37	0.015T-4L	0.015-in. -thick 5Al-2.5Sn (ELI) titanium alloy	Longitudinal	234.1	213.6	8
38	0.015T-5L			217.1	216.4	1
39	0.015T-6L			228.7	216.9	3
40	0.015T-4T	0.036-in. -thick 5Al-2.5Sn (ELI) titanium alloy	Transverse	226.9	212.7	4
41	0.015T-5T			216.9	211.0	2
42	0.015T-6T			224.1	211.7	3
	Average (longitudinal specimens)			226.6	215.6	4
	Average (transverse specimens)			222.6	211.8	3
43	0.036T-4L	0.036-in. -thick 5Al-2.5Sn (ELI) titanium alloy	Longitudinal	218.5	203.8	3
44	0.036T-5L			208.6	208.6	nil
45	0.036T-6L			228.8	209.4	8
46	0.036T-4T	0.036-in. -thick 5Al-2.5Sn (ELI) titanium alloy	Transverse	221.9	204.6	6
47	0.036T-5T			221.8	208.1	3
48	0.036T-6T			227.0	209.3	7
	Average (longitudinal specimens)			218.6	207.3	4
	Average (transverse specimens)			223.6	207.3	5

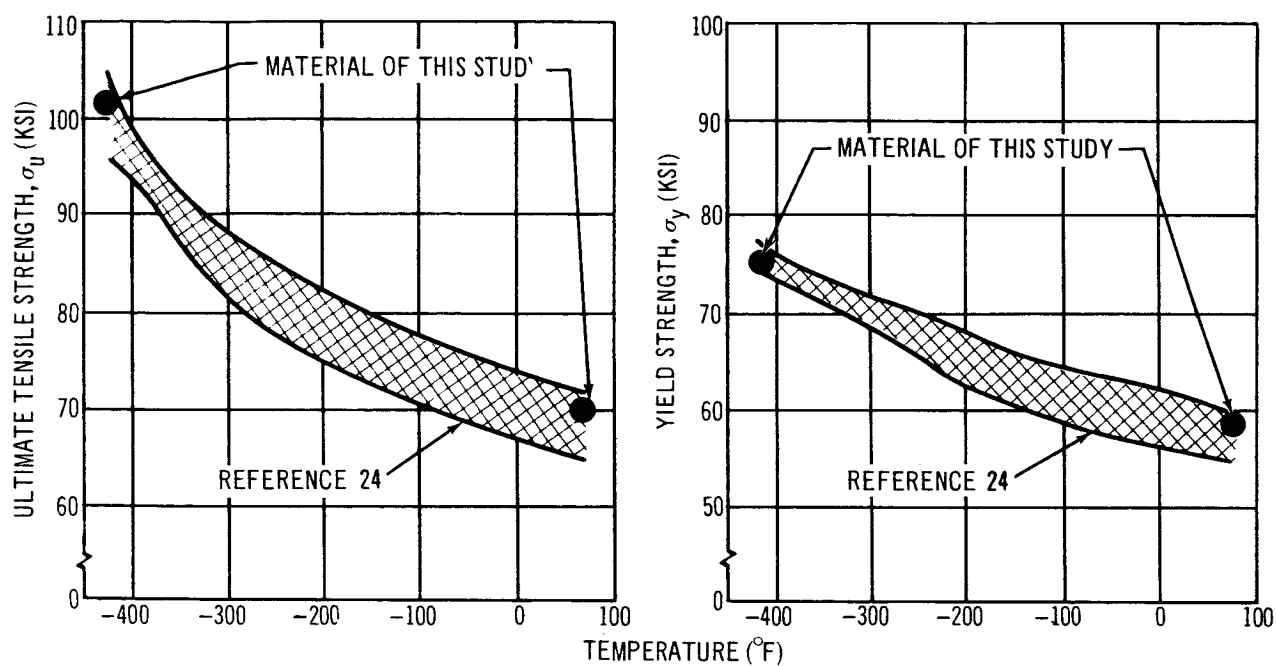


Figure B-1. Mechanical Properties of 2219-T87 Aluminum

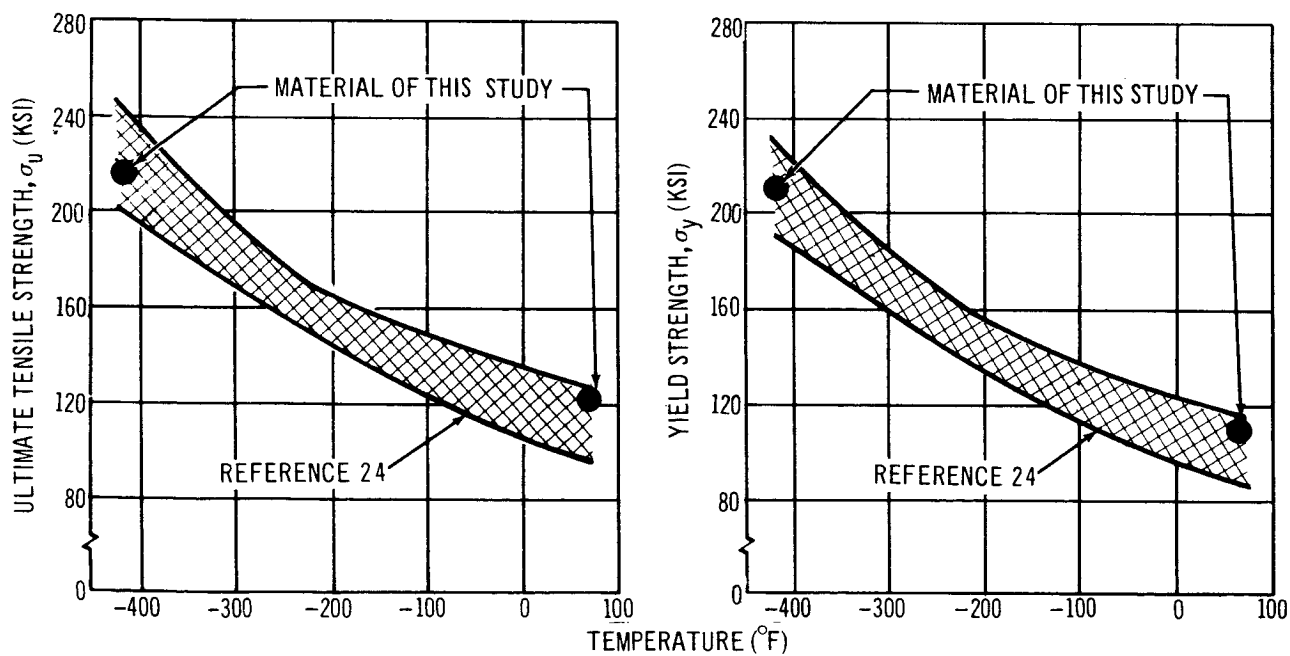


Figure B-2. Mechanical Properties of 5Al-2.5 Sn (ELI) Titanium

Appendix C  
STATIC FRACTURE TESTS OF PREFLAWED PANELS  
TABULATED DATA

Panel nomenclature relates to uniaxial and biaxial test specimen type, material, thickness, and sequence (serial no.) of particular panel types as follows:

1. Uniaxial Fatigue Preflawed Specimen Example  
UF032A#1            0.032-in.-thick Aluminum, Serial No. 1
2. Uniaxial Hypervelocity Impact Preflawed Specimen Example  
UH032A#1            0.032-in.-thick Aluminum, Serial No. 1
3. Biaxial Panel Example (Also used for Impact Tests)  
032A#B27            0.032-in.-thick Aluminum, Serial No.  
                              (Biaxial Type) 27

Table C-I  
FATIGUE PREFLAUED UNIAXIAL PANELS TEST PLAN

Test No.	Specimen No.	Thickness (in.)	Width (in.)	Machined Slot Length (in.)	Fatigue Crack Tip Length	
					Left (in.)	Right (in.)
1	UF125A#1	0.126	16.000	4.566	0.118	0.144
2	UF125A#2	0.126	12.000	1.004	0.122	0.100
3	UF032A#1	0.033	16.000	4.032	0.102	0.102
4	UF032A#2	0.032	12.005	1.013	0.100	0.100
5	UF036T#1	0.035	11.981	1.005	0.071	0.125
6	UF036T#2	0.035	11.980	0.197	0.034	0.048
7	UF015T#1	0.0145	12.008	1.000	0.057	0.074
8	UF015T#2	0.014	12.008	0.220	0.074	0.040

Table C-II  
HYPERVELOCITY IMPACT PREFLAUED UNIAXIAL PANELS TEST PLAN

Test No.	Specimen No.	Thickness (in.)	Width (in.)	Shot No.	Panel Position	Flaw Size (in.)
9	UH125A#1	0.126	11.950	B8-20	Rear	2.166
10	UH125A#2	0.126	12.004	B8-20	Front	0.763
11	UH125A#3	0.126	12.004	B8-18	Rear	0.892
12	UH032A#1	0.033	12.003	B8-18	Front	0.467
13	UH032A#2	0.034	11.998	B8-17	Rear	2.401
14	UH032A#3	0.033	12.005	B8-17	Front	0.477
15	UH036T#1	0.035	12.000	B8-15	Rear	0.560
16	UH036T#2	0.035	12.002	B8-15	Front	0.250
17	UH036T#3	0.036	12.015	B8-16	Rear	0.325
18	UH015T#1	0.014	12.001	B8-16	Front	0.180
19	UH015T#2	0.014	11.985	B8-13	Rear	0.450
20	UH015T#3	0.014	11.985	B8-13	Front	0.185

Table C-III  
FATIGUE PREFLOWED BIAXIAL PANELS TEST PLAN

Specimen No.	Machined Slot Length (in. )	Fatigue Crack Tip Length		Burst Test Run No.
		Left (in. )	Right (in. )	
032A#B01	0.2	0.02	0.03	1
032A#B02	1.0	0.07	0.10	2
125A#B01	1.0	0.07	0.07	3
015T#B01	0.2	0.03	0.04	4
015T#B02	1.0	0.05	0.08	5
036T#B02	1.0	0.05	0.06	6

Table C-IV  
HYPERVELOCITY IMPACT PREFLOWED BIAXIAL PANELS TEST PLAN

Panel No.	Flawed By Shot No. B-8. 2- (Appendix D)	Hypervelocity Puncture Size (in. )	Burst Test Run No.
032A#B27	59	0.34	7
032A#B20	49	0.22	---
125A#B06	64	0.69	10 and 13
125A#B03	26	0.20	---
015T#B13	56	0.20	8
015T#B11	52	0.16	11
036T#B08	65	0.41	9 and 12
036T#B06	62	0.33	---

Table C-V  
UNIAXIAL TESTS OF 2219-T87 ALUMINUM PANELS AT -423°F

Panel No. (code)	$\sigma_{\text{Gross or } \sigma_R}$ (psi)	$\sigma_y$ (psi)	$\sigma_u$ (psi)	w (in.)	$l_o$ or $2a_o$ (in.)	$l_c$ or $2a_c$ (in.)	Type Flaw	$K_c$ (KSI√in.)		$R_p$ ( $l_c$ ) ( $l_o$ )	
								(2a)	( $2a_o$ )	( $l_c$ )	( $l_o$ )
UF032A#1	27,800	74,000	102,000	16	4.24	7.03*	Fatigue	111*	78	6.60*	2.0
UF032A#2	48,100	74,000	102,000	12	1.21	2.02	Fatigue	100	76	2.88	1.39
UH032A#1	70,600	74,000	102,000	12	0.47	0.81	Impact	109	82	2.92	1.50
UH032A#2	39,200	74,000	102,000	12	2.40	3.91	Impact	114	85	5.60	2.17
UH032A#3	70,900	74,000	102,000	12	0.48	0.85	Impact	113	85	3.19	1.58
UF125A#1	26,850	74,000	102,000	16	4.83	6.31	Fatigue	99	82	4.40	2.41
UF125A#2	46,200	74,000	102,000	12	1.23	1.94	Fatigue	92	72	2.37	1.24
UH125A#1	41,200	74,000	102,000	12	2.17	3.40	Impact	110	85	4.65	2.08
UH125A#2	65,500	74,000	102,000	12	0.76	1.75	Impact	145*	92	6.80*	2.00
UH125A#3	54,200	74,000	102,000	12	0.89	1.26	Impact	91	76	2.05	1.33

SUMMARY AND BREAKOUT BY PANEL TYPE OF TEST RESULTS

Panel Type	Thickness (in.)	$K_c$ (KSI√in.)		$R_p$	
		(2a)	( $2a_o$ )	( $l_c$ )	( $l_o$ )
Average values for fatigue preflawed panel tests	0.032	100}** 106}	77	2.88}** 4.74}	1.70
	0.125	96	77	3.38	1.82
	0.032 & 0.125	97}** 100}	77	3.22}** 4.06}	1.76
Average values for impact preflawed panel tests	0.032	112	84	3.90	1.75
	0.125	101}** 115}	84	3.35}** 4.50}	2.14
	0.032 & 0.125	107}** 113}	84	3.68}** 4.20}	1.94
Total aluminum panel tests	0.032 & 0.125	103}** 108}	81	3.51}** 4.15}	1.87

\*Values uncertain

\*\*Upper number is average of all values considered to be reliable; lower number includes "Values Uncertain"  
as tabulated in the basic table in the average value calculation.

Table C-VI

## UNIAXIAL TESTS OF 5A1-2.5Sn (ELI) TITANIUM PANELS AT -423°F

Panel No. (code)	$\sigma_{\text{Gross or } \sigma_R}$ (psi)	$\sigma_y$ (KSI)	$\sigma_u$ (KSI)	w (in.)	$l_o$ or $2a_o$ (in.)	$l_c$ or $2a_c$ (in.)	Type Flaw	$K_c$ (KSI $\sqrt{\text{in.}}$ )		$R_p$ ( $l_c$ )		$(l_o)$
								(2a)	( $2a_o$ )	( $l_c$ )	( $l_o$ )	
UF015T#1	64,700	210	220	12	1.13	1.39	Fatigue	98	89	0.52	0.395	
UF015T#2	112,400	210	220	12	0.33	0.71	Fatigue	128	88	0.88	0.375	
UH015T#1	180,000	210	220	12	0.18	0.34	Impact	164	120	2.43	1.23	
UH015T#2	144,000	210	220	12	0.45	0.94*	Impact	201*	139	2.82*	1.12	
UH015T#3	179,000	210	220	12	0.185	0.33	Impact	162	122	2.26	1.30	
UF036T#1	73,700	210	220	12	1.20	1.84	Fatigue	131	105	1.03	0.58	
UF036T#2	129,000	210	220	12	0.28	1.07	Fatigue	187	95	2.23	0.46	
UH036T#1	136,000	210	220	12	0.56	0.96*	Impact	189*	143	2.33*	1.20	
UH036T#2	172,500	210	220	12	0.25	0.44	Impact	176	133	2.58	1.25	
UH036T#3	121,000	210	220	12	0.33	0.52*	Impact	120*	95*	0.77*	0.47*	

## SUMMARY AND BREAKOUT BY PANEL TYPE OF TEST RESULTS

Panel Type	Panel Thickness (in.)	$K_c$ (KSI $\sqrt{\text{in.}}$ )		$R_p$	
		(2a)	( $2a_o$ )	( $l_c$ )	( $l_o$ )
Average values for fatigue preflawed panel tests	0.015	113	88	0.70	0.385
	0.036	159	100	1.63	0.52
	0.015 & 0.036	136	94	1.17	0.45
Average values for impact preflawed panel tests	0.015	163** 176	127	2.34** 2.50	1.22
	0.036	176** 162	138** 124	2.58** 1.89	1.22** 0.97
	0.015 & 0.036	167** 169	131** 125	2.42** 2.20	1.22** 1.10*
Average values for all titanium panels	0.015 & 0.036	147** 156	115** 113	1.70** 1.78	0.88** 0.84

\*Values uncertain

\*\*Upper number is average of all values considered to be reliable; lower number includes "Values Uncertain" as tabulated in the basic table in the average value calculation.



Table C-VII  
BIAXIAL BURST TESTS OF PREFLAUED PANELS AT -423°F

Panel No.	Material	Thickness (in.)	Flaw Type	$l_o$ or $2a_o$ (in.)	$l_c$ or $2a_c$ (in.)	$\sigma_H$ (KSI)	Panel Radius at Rupture (in.)
032A#B01	Al	0.032	Fatigue	0.255	1.04	73.5	53.5
032A#B02	Al	0.032	Fatigue	1.17	2.44	44.0	51.7
125A#B01	Al	0.125	Fatigue	1.14	2.20	43.0	50.5
015T#B01	Ti	0.015	Fatigue	0.27	0.27→0.45	141.2	44.0
015T#B02	Ti	0.015	Fatigue	1.13	1.31	90.7	46.0
036T#B02	Ti	0.036	Fatigue	1.11	1.86	84.0	46.5
032A#B27	Al	0.032	Impact	0.344	?	96.0	44.5
015T#B13	Ti	0.015	Impact	0.204	?	218	37.7
015T#B11	Ti	0.015	Impact	0.156	?	228	33.2
036T#B08	Ti	0.036	Impact	0.407	?	202	37.9
125A#B06	Al	0.125	Impact	0.688	?	68*	45.5

\*No Fracture

Appendix D  
HYPERVELOCITY IMPACT TEST RESULTS  
TABULATED DATA

Detailed results of all hypervelocity impact tests are tabulated in this appendix. Included are results of (1) checkout tests with the fixture filled with  $\text{LN}_2$ , (2) point-load tests of quasi-composite panels, (3) point-load tests of unprotected panels, and (4) distributed-load tests. The test fixture was filled with  $\text{LH}_2$  during all tests after the  $\text{LN}_2$  checkout series.

Table D-I  
LN<sub>2</sub> CHECKOUT SHOTS

Shot No. B-8, 2-	Projectile					Type Panel				LH <sub>2</sub> Press. (psi)	Panel σ <sub>H</sub> (KSI)	Flaw Size or Description (in.)	Catastrophic		Comments
	Material	Size (in.)	Weight (mg)	Velocity (fps)	K. E. (ft-lb)	Al		Ti							
						0.032	0.125	0.015	0.036						
1	Pyrex	0.125 diam sphere	40	22,000	650	032A#B21				47.5	36.8	0.27 diam hole	X		Good shot
2	Pyrex	0.063 diam sphere	4.7	22,500	81.5	032A#B07				48.5	37.0	0.18 diam hole		X	Good shot
3	Alum.	0.094 diam sphere	20	≈22,000	332				036T#01	119.4	120.0	0.22 diam hole		X	Instrumentation trouble- no reliable velocity data

Table D-II (page 1 of 2)  
POINT LOAD TESTS OF QUASI-COMPOSITE PANELS

Shot No. B-8, 2-	Projectile				Type Panel				LH <sub>2</sub> Press. (psi)	Panel σ <sub>H</sub> (KSI)	Flaw Size or Description (in.)	Catastrophic		Comments
	Material	Size (in.)	Weight (mg)	Velocity (fpe)	K. E. (ft-lb)	A1						T1		
						0.032	0.125	0.015	0.036	Yes	No			
4	A1	0.094 diam sphere	20.0	21,500	-	032A#04			39.5	-	-	-	-	Shot missed panel*
6	A1	0.094 diam sphere	20.0	23,000	-	032A#04			38.5	41.6	1/2 long cracks	X		Sabot broke up during launch
9	A1	0.094 diam sphere	20.0	-	-	032A#B05			38.0	-	-	-	-	Shot missed panel, projectile and sabot broke up during launch
10	A1	0.094 diam sphere	20.0	22,000	332	032A#B05			38.5	41.5	severe damage	X		Size of flaw before catastrophic failure could not be determined
11	A1	0.063 diam sphere	6.0	23,800	-	032A#B06			38.0	-	severe damage	X		Sabot broke up, two holes in panel
12	A1	0.063 diam sphere	6.0	21,000	91	032A#B08			32.0	36.8	3/4 long cracks		X	Two holes in panel, one by projectile, one by sabot
14	A1	0.094 diam sphere	20.0	-	-	032A#B09			16.0	-	none	-	-	Sabot broke up during launch projectile did not hit target
18	A1	0.094 diam sphere	20.0	21,000	302	032A#B09			16.0	21.8	cracks to 3.0 diam		X	Good shot
19	A1	0.063 diam sphere	6.0	21,500	95	032A#B10			15.5	21.5	cracks to 1.9			Sabot broke up during launch
21	A1	0.094 diam sphere	20.0	19,500	-	125A#B03			-	-	panel undamaged	-	-	Shot missed panel
26	A1	0.094 diam sphere	20.0	22,700	353	125A#B03			150	36.4	0.25 diam hole, spall on back	X		Good shot
27	A1	0.063 diam sphere	6.0	22,500	104	032A#B11			58.5	53.8	0.16 diam hole, dished		X	Good shot
28	A1	0.063 diam sphere	6.0	22,600	105			015T#B04	61.0	104.5	3 radial tears	X		Good shot
29	A1	0.094 diam sphere	20.0	23,100	366	032A#B12			60.8	55.6	clean hole, dished		X	Good shot
30	A1	0.125 diam sphere	47.3	23,300	881	032A#B13			60.0	50.3	big hole, torn, severely curled	X		Good shot
31	A1	0.063 diam sphere	6.0	20,000		032A#B14			40.8	41.7	sabot hit panel	X		Shot missed panel
32	A1	0.063 diam sphere	6.0	22,300	120	032A#B14			41.0	40.0	tears to 2.25 diam		X	Good shot
33	A1	0.063 diam sphere	6.0	23,200	111			015T#B05	20.5	45.5	tears to 1.0 radius		X	Good shot

\*The "miss-aims" are the result of requirements set forth for allowable impact area on the target. Projectiles that did not fly within a 2-in. radius circle at the target centerline were caught by a steel plate just uprange of the target station.

Table D-II (page 2 of 2)

Shot No. B-8, 2-	Projectile					K. E. (ft-lb)	Type Panel				LH <sub>2</sub> Press. (psi)	Panel σ <sub>H</sub> (KSI)	Flaw Size or Description (in.)	Catastrophic		Comments
	Material	Size (in.)	Weight (mg)	Velocity (fps)	Al		Ti		Yes	No						
							0.032	0.125						0.015	0.036	
34	A1	0.063 diam sphere	6.0	21,800	98		015T#B06		91.0	144	dimple, 3 splits from impact points	X			Good shot	
35	A1	0.156 diam sphere	92.0	23,200	1,700				222	45.2	spall on back		X		Good shot	
36	A1	0.125 diam sphere	47.3	22,200	800	032A#B16		125A#B04	16.0	19.3	tears to 3.25 diam	?	?		Good shot	
37	A1	0.188 diam sphere	159	21,900	2,620			125A#B05	210	44.6	0.63 diam hole		X		Good shot	
38	A1	0.094 diam sphere	20.0	22,300	341	032A#B17			80.0	66.0	severe damage	X			Good shot	
39	A1	0.035 diam 0.037 long cylinder	2.26	20,800	-		015T#B07		100.5	-	-	-	-		Shot missed panel	
40	A1	0.035 diam 0.035 long cylinder	2.16	22,200	-		015T#B08		100	148	0.25 diam dimple, 1/32 deep		X		Only part of projectile hit panel	
41	A1	0.094 diam sphere	20.0	-	-			036T#B06	270	161	severe damage		X		Sabot and projectile hit panel	
42	A1	0.125 diam sphere	47.3	23,000	859	032A#B18			40.0	42.5	tears to 1.5 diam		X		Good shot	
43	A1	0.094 diam sphere	20.0	23,000	363			036T#B05	-	-	panel shattered	X			Good shot	
44	A1	0.094 diam sphere	20.0	-	-		015T#B09		-	-	-	-	-		Shot missed panel	
45	A1	0.156 diam sphere	92.0	21,700	1,486	032A#B19			37.5	40.0	severe damage		X		Good shot	
46	A1	0.094 diam sphere	20.0	22,000	332		015T#B09		24.5	-	severe damage	X			Good shot	

Table D-III (page 1 of 2)  
POINT LOAD TESTS OF UNPROTECTED PANELS

Shot No. B-8, 2-	Projectile					Type Panel				LH <sub>2</sub> Press. (psi)	Panel σ <sub>H</sub> (KSI)	Flaw Size or Description (in.)	Catastrophic		Comments
	Material	Size (in.)	Weight (mg)	Velocity (fps)	K. E. (ft-lb)	Al			Ti						
						0.032	0.125	0.015		0.036					
49	A1	0.097 diam sphere	20.0	21,700	323	032A#B20				49.0	54.0	0.22 diam hole	X		Good shot
50	A1	0.125 diam sphere	47.3	21,400	745	032A#B22				39.1	39.7	0.28 diam hole	X		Good shot
51	A1	0.063 diam sphere	6.0	21,100				015T#B10		104	156	0.125 diam hole	X		Good shot
52	A1	0.094 diam sphere	20.0	21,100	306			015T#B11		104.5	151.5	0.155 diam hole	X		Good shot
53	A1	0.156 diam sphere	92.0	21,400	1,430	032A#B23				43.5	35.0	0.30 diam hole	X		Good shot
54	A1	0.156 diam sphere	92.0	22,500	1,596			015T#B12		102	164	severe damage	X		Good shot
55	A1	0.220 diam sphere	253.0	21,600	4,050	032A#B25				40.0	41.8	0.375 diam hole, ripped in two	X		Good shot
56	A1	0.125 diam sphere	47.3	21,000	716			015T#B13		58.0	102	0.203 diam hole	X		Good shot
57	A1	0.125 diam sphere	47.3	21,200	727			015T#B08		57.0	101	approx. 50 pin hole, within 5.0 diam	X		Good launch, He tent broke projectile
58	A1	0.188 diam sphere	159.0	21,900	2,620	032A#B26				41.0	42.3	spray dam- age within 2.38 diam	X		Good launch, He tent broke projectile
59	A1	0.188 diam sphere	159.2	21,200	2,580	032A#B27				39.8	42.1	0.34 diam hole	X		Good shot
60	A1	0.156 diam sphere	92.0	21,500	1,460	032A#B28				80.0	68.9	0.312 diam hole	X		Good shot
61	A1	0.156 diam sphere	92.0	21,500	1,460			015T#B14		60.5	103	0.250 diam hole, trans- verse tear	X		Good shot
62	A1	0.188 diam sphere	159	20,900	2,390				036T#B06	152	103.2	0.328 diam hole	X		Good shot
63	A1	0.219 diam sphere	253	21,000	3,830				036T#B07	150	101.5	0.375 diam hole	X		Good shot
64	A1	0.250 diam sphere	378	20,400	5,390	125A#B06				218	44.2	0.890 diam hole	X		Good shot

Table D-III (page 2 of 2)

Shot No. B-8, 2-	Projectile					Type Panel				LH <sub>2</sub> Press. (psi)	Panel σ <sub>H</sub> (KSI)	Flaw Size or Description (in.)	Catastrophic		Comments	
	Material	Size (in. )	Weight (mg)	Velocity (fps)	K. E. (ft-lb)	Al							Yes	No		
						0.032	0.125	0.015	Ti	0.036						
65	A1	0.250 diam sphere	378	21,900	6,210					036T#B08	154	105.5	0.410 diam hole	X		Good shot
66	A1	0.250 diam sphere	378	21,300	5,870		125A#B07				330	62.3	0.780 diam hole	X		Good shot
67	A1	0.188 diam sphere	159	21,300	2,480					036T#B09	257	153	0.340 diam hole	X		Good shot
91	A1	0.125 diam sphere	47.3	21,900	-			015T#B03			-	-	spray damage	X		Shot missed panel
92	A1	0.188 diam sphere	159	21,100	2,435	032A#B03					83.5	69.5	panel split	X		Good shot
93	A1	0.219 diam sphere	253	20,900	3,800					036T#B03	262	150	0.440 diam hole	X		Good shot
94	Lexan	0.352 diam 0.350 long cylinder	572	21,800	9,300		125A#B02				340	64.4	0.940 diam hole	X		Good shot
96	A1	0.125 diam sphere	47.3	22,200	800			015T#B27			100	166	0.188 diam hole	X		Good shot
107	A1	0.250 diam sphere	378	21,200	5,810					036T#B12	282	169	severe damage	X		Good shot

# Table D-IV TEST PLAN FOR DISTRIBUTED-LOAD TESTS

- I. Tests of 0.032-in. -thick, 2219-T87 aluminum alloy biaxial panels
  - A. Panel membrane stress (nominal),  $0.9 \sigma_y$ 
    - (1) Bumper = 0.032-in. -thick aluminum (2219-T87);  $S_s = 3$  in.
    - (2) Bumper = 0.032-in. -thick aluminum (2219-T87);  $S_s = 6$  in.
    - (3) Bumper = 0.020-in. -thick lead sheet
      - (a) Bumper spacing = 6 in.
      - (b) Bumper spacing = 3 in.
  - B. Panel membrane stress (nominal) =  $0.6 \sigma_y$ 
    - (1) Bumper = 0.032-in. -thick aluminum (2219-T87);  $S_s = 3$  in.
    - (2) Bumper = 0.032-in. -thick aluminum (2219-T87);  $S_s = 6$  in.
- II. Tests of 0.125-in. -thick, 2219-T87 aluminum alloy biaxial panels
  - A. Panel membrane stress (nominal),  $0.9 \sigma_y$ 
    - (1) Bumper = 0.020-in. -thick lead sheet
      - (a) Bumper spacing = 6 in.
      - (b) Bumper spacing = 3 in.
    - (2) Bumper = 0.032-in. -thick aluminum (2219-T87), bumper spacing = 6 in
    - (3) Bumper = 0.050-in. -thick aluminum
      - (a) Bumper spacing = 3 in.
      - (b) Bumper spacing = 6 in.
- III. Tests of 0.015-in. -thick, 5Al-2.5Sn (ELI) titanium alloy biaxial panels
  - A. Panel membrane stress (nominal),  $\frac{\sigma_u}{1.4}$ 
    - (1) Bumper = 0.032-in. -thick aluminum (2219-T87);  $S_s = 3$  in.
    - (2) Bumper = 0.032-in. -thick aluminum (2219-T87);  $S_s = 6$  in.
    - (3) Bumper = 0.020-in. -thick lead sheet
      - (a) Bumper spacing = 3 in.
      - (b) Bumper spacing = 6 in.
    - (4) Bumper = 0.010-in. -thick lead sheet;  $S_s = 6$  in.
  - B. Panel membrane stress (nominal), 67% of  $\frac{\sigma_u}{1.4}$ 
    - (1) Bumper = 0.032-in. -thick aluminum (2219-T87);  $S_s = 3$  in.
    - (2) Bumper = 0.032-in. -thick aluminum (2219-T87);  $S_s = 6$  in.
- IV. Tests of 0.036-in. -thick, 5Al-2.5Sn (ELI) titanium alloy
  - A. Panel membrane stress (nominal),  $\frac{\sigma_u}{1.4}$ 
    - (1) Bumper = 0.020-in. -thick lead sheet
      - (a) Bumper spacing = 6 in.
      - (b) Bumper spacing = 3 in.



Table D-V (page 1 of 3)  
DISTRIBUTED-LOAD TEST RESULTS

Shot No.	Material	Size (in.)	Weight (mg)	Velocity (fps)	K. E. (ft-lb)	Type Panel				Test and Shield Configuration Table D-IV	LH <sub>2</sub> Press. (psi)	Panel %H (KSI)	Flaw Size or Description (in.)	Catastrophic		Comments
						A1	Ti	A1	Ti					Yes	No	
47	Al	0.094 diam sphere	20.0	22,100	-	032A#B20	-	-	-	I. A. 2	42.5	-	no damage		X	Preliminary bumper shot, found ice on panel
48	Al	0.094 diam sphere	20.0	21,800	-	-	-	-	-	-	-	-	-	-	-	Ice investigation shot
68	Al	0.188 diam sphere	159	21,500	2,530	032A#B29	-	-	-	I. A. 1	82	63.5	4 splits	X		Good shot
69	Al	0.125 diam sphere	47.3	20,700	695	-	015T#B15	-	-	III. A. 1	110	167	severe damage	X		Good shot
70	Al	0.125 diam sphere	47.3	21,700	765	032A#B30	-	-	-	I. A. 1	80	67.5	3 splits	X		Good shot
71	Al	0.063 diam sphere	6.0	20,700	88.2	-	015T#B16	-	-	III. A. 1	101	152	4 pin holes, 2.5 diam spray area		X	Good shot
72	Al	0.094 diam sphere	20.0	20,600	291	032A#B31	-	-	-	I. A. 1	80	63.6	2.5 diam spray area		X	Good shot
73	Al	0.094 diam sphere	20.0	-	-	-	015T#B17	-	-	III. A. 1	-	-	panel undamaged		X	Miss aim
74	Al	0.094 diam sphere	20.0	21,200	308	-	015T#B17	-	-	III. A. 1	104	160	about 50 pinholes		X	Good shot
75	Al	0.156 diam sphere	92.0	-	-	032A#B32	-	-	-	I. A. 2	80	64.5	panel hit by sabot	X		Hit by sabot
76	Al	0.125 diam sphere	47.3	20,100	656	-	015T#B18	-	-	III. A. 2	102	153	about 20 pinholes		X	Good shot
77	Al	0.156 diam sphere	92.0	19,500	1,200	-	015T#B22	-	-	III. A. 2	105	156	panel shattered	X		Good shot
78	Al	0.156 diam sphere	92.0	20,100	1,275	032A#B33	-	-	-	I. A. 2	82	67.3	2 splits	X		Good shot
79	Lexan	0.280 diam 0.200 long cylinder	227	22,400	3,910	-	015T#B23	-	-	III. A. 3. a	100	154	severe tearing	X		Good shot
80	Al	0.125 diam sphere	47.3	20,400	675	032A#B34	-	-	-	I. A. 2	81.5	66.1	2 holes, 9 diam spray area		X	Good shot
81	Lexan	0.280 diam 0.200 long cylinder	210	23,000	3,810	-	015T#B24	-	-	III. A. 3. b	101	151	no pits, leads spray on panel	X		Good shot
82	Lexan	0.280 diam 0.200 long cylinder	210	21,400	3,300	032A#B35	-	-	-	I. A. 3. a	80	64.9	lead spray on panel	X		Good shot
83	Lexan	0.280 diam 0.200 long cylinder	220	22,600	3,650	032A#B36	-	-	-	I. A. 3. b	79	65.5	panel split in half	X		Good shot

Table D-V (page 2 of 3)

Shot No.	Material	Type Panel					K. E. (ft-lb)	Velocity (fps)	Weight (mg)	Size (in.)	Test and Shield Configuration Table D-IV	LH <sub>2</sub> Press. (psi)	Panel σ <sub>H</sub> (KSI)	Flaw Size or Description (in.)	Catastrophic		Comments
		Al			Ti	Yes									No		
		0.032	0.125	0.015	0.036												
84	Lexan			015T#B19			3,850	22,600	220	0.280 diam 0.200 long cylinder	III. A. 4	105	156	1 pin hole		X	Good shot
85	Al		032A#B39				1,380	20,900	92.0	0.156 diam sphere	I. B. 1	39.0	41.7	4 splits, 2.75 diam spray area	X		Good shot
86	Al			015T#B25			-	-	92.0	0.156 diam sphere	-	-	-	panel hit by sabot	X		Bad shot
87	Al		032A#B41				859	23,000	47.3	0.125 diam sphere	I. B. 1	39.5	42.0	6.0 diam spray area	X		Good shot
88	Al			015T#B20			1,470	21,600	92.0	0.156 diam sphere	III. B. 1	54.0	100	2 diam major spray damage	X		Good shot
89	Al		032A#B37				2,435	21,100	159	0.188 diam sphere	I. B. 2	44.0	41.2	5 pin holes, 3 diam spray area	X		Good shot
90	Al			015T#B21				22,200	47.3	0.125 diam sphere	III. B. 1	55.0	101	3 diam spray area 0.63 crack	X		Good shot
95	Al			015T#B26			2,720	22,300	159	0.188 diam sphere	III. B. 2	55.0	106	6 diam spray area	X		Good shot
97	Al		032A#B38				3,620	20,400	253	0.218 diam sphere	I. B. 2	41.5	41.9	10 diam spray area	X		Good shot
98	Al			015T#B28			1,480	21,700	92.0	0.156 diam sphere	III. B. 2	57.0	95.5	pin holes to 3 diam	X		Good shot
99	Lexan		125A#B08				-	-	365.0	0.350 diam 0.350 long cylinder	-	315	66.6	-			Missed target
100	Lexan		125A#B09				9,550	22,200	565	0.350 diam 0.350 long cylinder	II. A. 1. a	324	62.5	light ero- sion, 0.5W x 2.5L	X		Good shot
101	Lexan			036T#B10			10,250	22,900	570	0.350 diam 0.350 long cylinder	IV. A. 1. a	270	161	light spray	X		Good shot
102	Lexan		125A#B10				9,600	22,200	570	0.356 diam 0.350 long cylinder	II. A. 1. b	320	50.5	light spray	X		Good shot
103	Lexan			036T#B11			10,350	23,000	570	0.356 diam 0.350 long cylinder	IV. A. 1. b	230	145	severe damage	X		Good shot

Table D-V (page 3 of 3)

Shot No.	Material	Type Panel					K. E. (ft-lb)	Velocity (fps)	Weight (mg)	Size (in.)	Test and Shield Configuration Table D-IV		LH <sub>2</sub> Press. (psi)	Panel $\sigma_H$ (KSI)	Flaw Size or Description (in.)	Catastrophic		Comments
		Al	0.032	0.125	0.015	Ti										Yes	No	
104	Al			125A#B11			6,380	22,200	378	0.250 diam sphere	II A. 2. a		355	68.5	pin holes and cracks on back		X	Good shot
105	Al			125A#B12			6,040	21,600	378	0.250 diam sphere	II A. 3. a		320	61.0	panel shattered	X		Good shot
106	Al			125A#B13			5,020	19,700	378	0.250 diam sphere	II A. 3. b		320	61.0	4 diam spray area	X		Good shot
108	Al			X			-	20,900	378	0.250 diam	II A. 2. a		-	-	4 holes, 4.5 diam spray area	X		Test shot on dummy panel

## REFERENCES

1. W.G. Fawcett, F.L. Schutz, R.K. Sloan, and H.G. Trostle. Scientific Exploration with Mariner 4. *Astronautics and Aeronautics*, October 1965.
2. F.S. Stepka and C.R. Morse. Preliminary Investigation of Catastrophic Fracture of Liquid-Filled Tanks Impacted by High-Velocity Projectiles. NASA TN D-1537, May 1963.
3. P.C. Chou, H.S. Sidhu, and R.R. Karpp. Analysis of Peak Pressure Generated in Water by High Velocity Impact. Drexel Institute of Technology Report No. 160-1, April 1963.
4. J.A. Fager. Development of Titanium Alloy for Lightweight LH<sub>2</sub> Tankage. *Journal of Spacecraft and Rockets*, May-June 1965.
5. J.L. Christian and A. Hurlich. Physical and Mechanical Properties of Pressure Vessel Materials for Application in a Cryogenic Environment. Technical Documentary Report No. ASD-TDR-62-258; Part II, General Dynamics Astronautics, April 1963.
6. H.S. Babel, D.A. Eitman, and R.W. McIver. The Biaxial Strengthening of Textured Titanium. Douglas Paper No. 3471, June 1965.
7. A. Bonales. The Spark that Carves. *Product Engineering*, 27 September 1965.
8. J.S. Curtis. An Accelerated Reservoir Light-Gas Gun. NASA TN D-1144, February 1962.
9. W.S. Pierce. Strength Comparison of Flawed Single-Layer and Multilayer AISI 301 Stainless-Steel Pressure Vessels at Cryogenic Temperatures. NASA TN D-2949, October 1965.
10. G.R. Irwin. Fracture Testing of High-Strength Materials Under Conditions Appropriate for Stress Analysis. Naval Research Laboratory Report 5486, July 1960.
11. R.H. Christensen and P.H. Denke. Crack Strength and Crack Propagation Characteristics of High Strength Metals. ASD-TR-207, USAF Aeronautical Systems Division, January 1962.

12. R.B. Anderson. Fracture Mechanics of Through-Cracked Cylindrical Pressure Vessels. NASA TM-X-52079, February 1965.
13. R.H. Christensen and R.J. Bellinfante. Some Considerations in the Fatigue Design of Launch and Spacecraft Structures. NASA CR-242, June 1965.
14. P. Kuhn. Notch Effects on Fatigue and Static Strength. Presented at Symposium on Aeronautical Fatigue, Rome, April 1963.
15. J.F. Lundeborg, P.H. Stern, and R.J. Bristow. Meteoroid Protection for Spacecraft Structures. NASA CR-54201, October 1965.
16. C.J. Maiden and A.R. McMillan. An Investigation of the Protection Afforded a Spacecraft by a Thin Shield. Preprint, AIAA, Aerospace Sciences Meeting, New York, New York, 20-22 January 1964.
17. J.L. Summers. Investigation of High-Speed Impact: Regions of Impact and Impact at Oblique Angles. NAS TND-94, October 1959.
18. R.L. Bjork. Review of Physical Processes in Hypervelocity Impact and Penetration. Proceedings of the Sixth Symposium on Hypervelocity Impact, The Firestone Tire and Rubber Company (Conference Host), August 1963.
19. J.M. Walsh and J.H. Tillotson. Hydrodynamics of Hypervelocity Impact. Proceedings of the Sixth Symposium on Hypervelocity Impact, The Firestone Tire and Rubber Company (Conference Host), August 1963.
20. J.M. Walsh and W.E. Johnson. On the Theory of Hypervelocity Impact. Proceedings Seventh Hypervelocity Impact Symposium, Martin Company (Symposium Coordinator), February 1965.
21. F.S. Stepka, C.R. Morse, and R.P. Dengler. Investigation of Characteristics of Pressure Waves Generated in Water Filled Tanks Impacted by High-Velocity Projectiles. NASA TN D-3143, December 1965.
22. F.S. Stepka. Personal communication.
23. R.B. Scott. Cryogenic Engineering. D. Van Nostrand Co., Inc., 1959
24. Cryogenic Materials Data Handbook. Cryogenic Engineering Laboratory, Boulder, Colorado, U.S. Department of Commerce, National Bureau of Standards.

## DISTRIBUTION LIST

	<u>COPIES</u>
<p>National Aeronautics and Space Administration            Lewis Research Center            21000 Brookpark Road            Cleveland, Ohio 44135</p>	
Attention: Contracting Officer, MS 500-210	1
Liquid Rocket Technology Branch, MS 500-209	8
Technical Report Control Office, MS 5-5	1
Technology Utilization Office, MS 3-16	1
AFSC Liaison Office, MS 4-1	2
Library	2
Office of Reliability & Quality Assurance, MS 500-203	1
F. S. Stepka, MS 49-1	1
J. F. Mondt, MS 500-309	1
Richard Kemp, MS 49-1	1
<p>National Aeronautics &amp; Space Administration            Washington, D. C. 20546</p>	
Attention: Code	2
<p>Scientific and Technical Information Facility            P. O. Box 5700            Bethesda, Maryland 20014</p>	
Attention: NASA Representative Code CRT	6

COPIES

National Aeronautics and Space Administration  
Ames Research Center  
Moffett Field, California 94035  
Attention: Library

1

National Aeronautics and Space Administration  
Flight Research Center  
P. O. Box 273  
Edwards, California 93523  
Attention: Library

1

National Aeronautics and Space Administration  
Goddard Space Flight Center  
Greenbelt, Maryland 20771  
Attention: Library  
W. M. Alexander

1

1

National Aeronautics and Space Administration  
Langley Research Center  
Langley Station  
Hampton, Virginia 23365  
Attention: Library

1

National Aeronautics and Space Administration  
Manned Spacecraft Center  
Houston, Texas 77001  
Attention: Library

1

National Aeronautics and Space Administration  
George C. Marshall Space Flight Center  
Huntsville, Alabama 35812  
Attention: Library

1

National Aeronautics and Space Administration  
Western Operations  
150 Pico Boulevard  
Santa Monica, California 90406  
Attention: Library

1

National Aeronautics and Space Administration  
John F. Kennedy Space Center  
Cocoa Beach, Florida 32931  
Attention: Library

1

Jet Propulsion Laboratory  
4800 Oak Grove Drive  
Pasadena, California 91103  
Attention: Library

1

	<u>COPIES</u>
Office of the Director of Defense Research & Engineering Washington, D. C. 20301 Attention: Dr. H. W. Schulz, Office of Asst. Dir. (Chem. Technology)	1
RTD(RTNP) Bolling Air Force Base Washington, D. C. 20332 Attention: J. W. Minette, E. A. Kritzer	1 2
Arnold Engineering Development Center Attention: AEOIM Air Force Systems Command Tullahoma, Tennessee 37389	1
AFSC(SCLT/Captain S. W. Bowen) Andrews Air Force Base Washington, D. C. 20332	1
AFRPL(RPR) Edwards, California 93523	1
AFRPL(RPM) Edwards, California 93523	1
AFFTC(FTAT-2) Edwards AFB, California 93523	1
Office of Research Analyses (OAR) Attention: RRRT Holloman Air Force Base, New Mexico 88330	1
Air Force Office of Scientific Research Washington, D. C. 20333 Attention: SREP, Dr. J. F. Masi	1
AFRPL(RPC) Edwards, California 93523	1
Wright-Patterson Air Force Base Ohio 45433 Attention: AFML(MAAE)	1
Wright-Patterson Air Force Base Ohio 45433 Attention: AFML(MAAM)	1



	<u>COPIES</u>
Commanding Officer Ballistic Research Laboratories Aberdeen Proving Ground, Maryland 21005 Attention: AMXBR-1, F. E. Allison, R. J. Eichelberger	3
Department of the Army U. S. Army Materiel Command Washington, D. C. 20315 Attention: AMCRD-RC	1
Commanding Officer U. S. Army Research Office (Durham) Box CM, Duke Station Durham, North Carolina 27706	1
U. S. Army Missile Command Redstone Scientific Information Center Redstone Arsenal, Alabama 35808 Attention: Chief, Document Section	1
Bureau of Naval Weapons Department of the Navy Washington, D. C. 20360 Attention: DLI-3	1
Bureau of Naval Weapons Department of the Navy Washington, D. C. 20360 Attention: RMMP-2	1
Bureau of Naval Weapons Department of the Navy Washington, D. C. 20360 Attention: RMMP-4	1
Bureau of Naval Weapons Department of the Navy Washington, D. C. 20360 Attention: RRRE-6	1
Commander U. S. Naval Missile Center Point Mugu, California 93041 Attention: Technical Library	1
Commander U. S. Naval Ordnance Laboratory White Oak Silver Spring, Maryland 20910 Attention: Library	1

COPIES

Commander (Code 753) U. S. Naval Ordnance Test Station China Lake, California 93557 Attention: Technical Library	1
Commanding Officer Office of Naval Research 1030 E. Green Street Pasadena, California 91101	1
Director (Code 6180) U. S. Naval Research Laboratory Washington, D. C. 20390 Attention: H. W. Carhart W. W. Atkins M. A. Persechino	1 1 1
Commander U. S. Naval Weapons Laboratory Dahlgren, Virginia 22448 Attention: Technical Library	1
Aerojet-General Corporation P. O. Box 296 Azusa, California 91703 Attention: Librarian	1
Aerojet-General Corporation 11711 South Woodruff Avenue Downey, California 90241 Attention: F. M. West, Chief Librarian	1
Aerojet-General Corporation Attention: Technical Library 2484-2015A P. O. Box 1947 Sacramento, California 95809	1
Aerospace Corporation P. O. Box 95085 Los Angeles, California 90045 Attention: Library-Documents	1
IIT Research Institute Technology Center Chicago, Illinois 60616 Attention: C. K. Hersh, Chemistry Division Dr. R. Cornish	1 1

COPIES

ARO, Inc. Arnold Engrg. Dev. Center Arnold AF Station, Tennessee 37389 Attention: Dr. B. H. Goethert, Chief Scientist Julius Lukasiewicz	1 1
University of Denver Denver Research Institute P. O. Box 10127 Denver, Colorado 80210 Attention: Security Office R. E. Recht, Mechanics Division	1 1
Battelle Memorial Institute 505 King Avenue Columbus, Ohio 43201 Attention: Report Library, Room 6A	1
Bell Aerosystems Box 1 Buffalo, New York 14205 Attention: T. Reinhardt	1
The Boeing Company Aero Space Division P. O. Box 3707 Seattle, Washington 98124 Attention: Ruth E. Peerenboom (1190) Jack Lundeberg	1 1
Chemical Propulsion Information Agency Applied Physics Laboratory 8621 Georgia Avenue Silver Spring, Maryland 20910	1
Propulsion Engineering Division (D. 55-11) Lockheed Missile & Space Company 1111 Lockheed Way Sunnyvale, California 94087	1
Douglas Aircraft Company, Inc. Santa Monica Division 3000 Ocean Park Boulevard Santa Monica, California 90405 Attention: Mr. J. L. Waisman	1

COPIES

General Dynamics/Astronautics P. O. Box 1128 San Diego, California 92112 Attention: Library and Information Services (128-00)	1
Institute for Defense Analyses 400 Army-Navy Drive Arlington, Virginia 22202 Attention: Classified Library	1
Lockheed Propulsion Company P. O. Box 111 Redlands, California 92374 Attention: Miss Belle Berlad, Librarian	1
Marquardt Corporation 16555 Saticoy Street Box 2013 - South Annex Van Nuys, California 91404	1
North American Aviation, Inc. Space & Information Systems Division 12214 Lakewood Boulevard Downey, California 90242 Attention: Technical Information Center D/096-722 (AJOI) E. R. Mertz	1 1
Rocket Research Corporation 520 South Portland Street Seattle, Washington 98108	1
Rocketdyne 6633 Canoga Avenue Canoga Park, California 91304 Attention: Library, Department 596-306	1
Space Technology Laboratory, Inc. 1 Space Park Redondo Beach, California 90200 Attention: STL Tech. Lib. Doc. Acquisitions	1
Thiokol Chemical Corporation Reaction Motors Division Denville, New Jersey 07834 Attention: Librarian	1

COPIES

Thiokol Chemical Corporation Rocket Operations Center P. O. Box 1640 Ogden, Utah 84401 Attention: Librarian	1
United Aircraft Corporation Corporation Library 400 Main Street East Harford, Connecticut 06118 Attention: Dr. David Rix	1
United Aircraft Corporation United Technology Center P. O. Box 358 Sunnyvale, California 94088 Attention: Librarian	1
General Electric Company Apollo Support Department P. O. Box 2500 Daytona Beach, Florida 32015 Attention: C. Day	1
National Aeronautics and Space Administration Langley Research Center Langley Station Hampton, Virginia 23365 Attention: Mr. D. Davis, Jr.	1
Mr. J. R. Dawson	1
Mr. Richard Heldenfels	1
Mr. William Kinard	1
Mr. E. T. Kruszewski	1
Mr. R. S. Osborne	1
Mr. Jerry Williams	1
National Aeronautics and Space Administration Ames Research Center Moffett Field, California Attention: Mr. Donald E. Gault	1
O. Robert Nysmith	1
James L. Summers	1
National Aeronautics and Space Administration George C. Marshall Space Flight Center Huntsville, Alabama Attention: Research Projects Div. (M-RP-R)	1
Jose F. Blumerick	1
James W. Carter, Future Projects Office, MFPO	1
Orlo K. Hudson	1

	<u>COPIES</u>
W. G. Johnson	1
W. D. Morphree	1
National Aeronautics and Space Administration Manned Spacecraft Center Houston, Texas	
Attention: Paige B. Burbank	1
C. H. Perrine	1
L. G. St. Leger	1
Jet Propulsion Laboratory 4800 Oak Drive Pasadena 2, California	
Attention: Charles Campen	1
Dr. V. Jaffee	1
C. L. Robillard	1
Dwayne F. Spencer	1
Wright-Patterson A. F. B. Ohio	
Attention: Commander, Air Tech. Intelligence Center	1
Attention: AFOIN-4BIA	1
Lt. Lloyd Hedgepeth, ASRMFP-1	1
K. I. Collier	1
A. K. Hopkins	1
J. F. Nicholson	1
J. M. O'Connor	1
F. Sachleh	1
University of California Los Alamos Scientific Laboratory P. O. Box 1663 Los Alamos, New Mexico	1
Prof. Pei Chi Chou Dept. Mechanical Engineering Drexel Institute of Technology Philadelphia 4, Pennsylvania	1
New York University College of Engineering Research Division University Heights New York 53, New York	
Attention: Dr. Paul F. Winternits	1

	<u>COPIES</u>
Harvard College Observatory Cambridge, Massachusetts Attention: Prof. F. L. Whipple	1
Cornell Aeronautical Laboratory, Inc. Buffalo, New York Attention: Dr. William Rae	1
Rand Corporation Santa Monica, California Attention: Robert A. Popetti James Rosen Jock E. Whitener	1 1 1
Aero-Space Corporation El Segundo, California Attention: Verne C. Frost	1
University of Toronto Toronto, Canada Attention: I. I. Glass	1
Sandia Corporation Albuquerque, New Mexico Attention: Walter Herrmann	1
Space Research Center McGill University 892 Sherbrooke Street, West Montreal, Quebec Canada Attention: G. V. Bull	2
Arthur D. Little, Inc. Cambridge 40, Massachusetts Attention: Dr. J. M. Bonneville	1
Martin Company P. O. Box 179 Denver, Colorado Attention: Dr. Arthur Ezra	1
Avco Corporation Wilmington, Massachusetts 01887 Attention: Robert R. McMath - RAD	1
Chance Vought Corporation Library Box 5907 Dallas 22, Texas	1

COPIES

Chrysler Corporation P. O. Box 26018 New Orleans 26, La. Attention: Elayne M. Brower-AEB-2761	1
Fundamental Methods Associates 31 Union Square West New York 2, New York Attention: Dr. Carl Klahr	1
General Electric Valley Forge Space Tech. Center P. O. Box 8555 Philadelphia 1, Pennsylvania Attention: T. D. Riney - TEMO J. F. Heyda - TEMO	1 1
General Motors Defense Research Labs Santa Barbara, California Attention: C. J. Maiden	1
Gruman Aircraft Engineering Corporation Bethpage, Long Island New York Attention: Library, John Tlasmati	1
Lockheed Missiles and Space Company Palo Alto, California Attention: P. E. Sandorff	1
The Martin Company Science Technology Library Mail 398 Baltimore 3, Maryland	1
Northrop Space Laboratories 3401 West Broadway Hawthorne, California 90250 Attention: R. D. Johnson, Space Materials Lab.	1
Republic Aviation Corporation Farmingdale, Long Island New York Attention: Sol Saul, Space System Structures	1



COPIES

Utah Research and Development  
2175 South 3270 West  
Salt Lake City, Utah  
Attention: Boyd Baugh

1

Computing Devices of Canada Limited  
P. O. Box 508  
Ottawa 4, Canada  
Attention: Dr. G. P. T. Wilenius  
J. A. Park

1

1

Republic Aviation  
333 West 1st Street  
Dayton 2, Ohio  
Attention: Paul Rossow

1

Carnegie Institute of Technology  
Dept. of Civil Engineering  
Pittsburgh, Pennsylvania  
Attention: Robert B. Anderson

1

National Aeronautics and Space Administration  
NASA Scientific and Technical Information Branch (RQT-35118)  
P. O. Box 33  
College Park, Maryland 20740

2